Protein folding and translocation

Protein folding and translocation
single-molecule investigations

PROEFSCHRIFT

ter verkrijging van
de graad van Doctor aan de Universiteit Leiden,
op gezag van de Rector Magnificus Dr. D. D. Breimer,
hoogleraar in de faculteit der Wiskunde en
Natuurwetenschappen en die der Geneeskunde,
volgens besluit van het College voor Promoties
te verdedigen op donderdag 16 november 2006
klokke 15.00

door

RUDOLPHUS GERARDUS HENRICUS VAN LEEUWEN

geboren te Gouda
in 1976

Promotor: Prof. dr. A. M. Dogterom
Copromotor: Dr. ir. S. J. Tans (FOM AMOLF)
Referent: Dr. ir. T. H. Oosterkamp
Overige leden: Prof. dr. S. L. Völker
Prof. dr. A. J. M. Driessen (Rijksuniversiteit Groningen)
Prof. dr. S. M. van der Vies (Vrije Universiteit Amsterdam)

© 2006 by Ruud van Leeuwen. All rights reserved.

Nederlandse titel: Eiwitvouwing en translocatie; onderzoekingen aan afzonderlijke moleculen

The work described in this thesis was performed at the FOM Institute for Atomic and Molecular Physics (AMOLF) in Amsterdam, The Netherlands. This work is part of the research programme of the 'Stichting voor Fundamenteel Onderzoek der Materie (FOM)', which is financially supported by the 'Nederlandse Organisatie voor Wetenschappelijk Onderzoek (NWO)'.

ISBN-10: 90-77209-22-0
ISBN-13: 978-90-77209-22-6

A digital version of this thesis can be obtained from `http://www.amolf.nl` and from `http://ub.leidenuniv.nl`. Printed copies can be obtained by request via email to `library@amolf.nl` or by addressing the library at the FOM Institute for Atomic and Molecular Physics (AMOLF), Kruislaan 407, 1098 SJ, Amsterdam, The Netherlands.

Cover design by Ruud van Leeuwen. Printed in the Netherlands by Ponsen & Looijen BV graphical company, Wageningen. Typeset with pdfTEX using the Adobe MinionPro font.

Voor Bep, Wim en Astrid

Contents

Voorwoord **11**

1 Optical tweezers **15**
- 1.1 Introduction . . . 15
- 1.2 Optical tweezers setup . . . 17
- 1.3 Force detection . . . 22
- 1.4 Flow system . . . 24

2 Towards optical tweezers measurements on protein translocation **29**
- 2.1 Introduction . . . 29
- 2.2 Materials and methods . . . 33
  - 2.2.1 Molecular constructs . . . 33
  - 2.2.2 Bulk assays . . . 35
  - 2.2.3 Microsphere preparation . . . 36
  - 2.2.4 Optical trapping procedures . . . 37
- 2.3 Results . . . 39
  - 2.3.1 Bulk studies on the preprotein length dependence of protein translocation . . . 39
  - 2.3.2 Optical tweezers experiments: surface approach . . . 41
  - 2.3.3 Optical tweezers experiments: micropipette approach . . 43
  - 2.3.4 Calculation of step response . . . 49
- 2.4 Discussion . . . 52

3 Unfolding the maltose-binding protein (MBP) with optical tweezers **55**
- 3.1 Introduction . . . 55
  - 3.1.1 The role of SecB in the targeting of proteins . . . 57
  - 3.1.2 Structure of SecB . . . 58
  - 3.1.3 The maltose-binding protein (MBP) . . . 59
- 3.2 Materials and methods . . . 61
  - 3.2.1 Experimental configuration . . . 61
  - 3.2.2 Cloning and protein expression of MBP constructs. 64
  - 3.2.3 Optical Tweezers setup . . . 65
  - 3.2.4 Microsphere preparation . . . 67

3.2.5 Steered molecular dynamics studies 68
3.3 Results 69
3.3.1 Forced unfolding of MBP using optical tweezers 69
3.3.2 Forced unfolding of a 4×MBP construct. 72
3.3.3 Steered molecular dynamics simulations on the forced unfolding of MBP 76
3.3.4 The effect of chaperone SecB on the forced unfolding of MBP 81
3.4 Discussion 83
3.4.1 Unfolding forces 84
3.4.2 Unfolding intermediates 88
3.4.3 Binding of SecB to MBP 89
3.4.4 Protein translocation context 91

4 Optical tweezers measurements on dsDNA-packaging by phage ϕ29 93
4.1 Introduction 93
4.2 DNA constructs 98
4.2.1 Construction of a short DNA construct 98
4.2.2 Construction of a long DNA construct 99
4.2.3 Removal of dsDNA oligonucleotides 101
4.2.4 Ligation of dsDNA oligonucleotides to ϕ29-L fragments . . 104
4.2.5 Preparation of the 24.4-kbp T7 DNA fragment 105
4.2.6 Restriction analysis design 106
4.2.7 Synthesis of a 32.4-kbp ϕ29-T7 construct 108
4.3 Optical tweezers experimental procedures 109
4.3.1 Preparation of optical tweezers experiment. 109
4.3.2 Optical tweezers setup 112
4.4 Results 112
4.4.1 Packaging of long DNA 112
4.4.2 The effect of spermine on packaging of DNA by bacteriophage ϕ29 115
4.4.3 Packaging of nicked DNA by bacteriophage ϕ29 118
4.5 Discussion 119

A The worm-like chain (WLC) model 121

Bibliography 125

Summary 133

Samenvatting 137

Curriculum Vitae 143

List of publications 143

Failure is always the best way to learn.
—Kings of Convenience, ‘Failure’

Voorwoord

Dit proefschrift beschrijft experimenten die zijn uitgevoerd in de Biofysica-groep van Sander Tans op het FOM-Instituut voor Atoom- en Molecuulfysica (AMOLF) in de periode van oktober 2001 tot september 2006. Aanvankelijk bestond de groep uit twee mensen – Sander en mij – maar inmiddels is de groep uitgegroeid tot een van de grotere groepen van AMOLF met 9 man.

We startten met een project waarin we, met behulp van een optisch pincet, de bewegingen van één afzonderlijk eiwit wilden volgen, terwijl het door een celmembraan heen werd getransporteerd, ofwel getransloceerd. Dit ambitieuze project werd – vanaf het eerste moment – uitgevoerd in hechte samenwerking met de Moleculaire Microbiologiegroep van Arnold Driessen aan de Rijksuniversiteit Groningen. In Amsterdam bouwde ik een optisch-pincetopstelling terwijl in Groningen aan de DNA- en eiwitconstructen werd gewerkt die benodigd waren voor het beoogde experiment. Om algemene biochemische technieken en de typische translocatieproeven te leren ging ik enkele weken naar Groningen. Toen zowel optisch pincet als moleculaire constructen eenmaal verder ontwikkeld waren kwam Danka Tomkiewicz enkele malen vanuit Groningen naar Amsterdam om mij te vergezellen bij de eerste pogingen tot een enkelmolecuuls translocatie-experiment. Na twee jaar werd het team op AMOLF versterkt door Matt Tyreman. Een jaar later verschoof mijn focus naar twee andere projecten: Enerzijds optisch-pincetmetingen aan eiwit(ont-)vouwing en het effect van een chaperonne-eiwit daarop, en anderzijds optisch-pincetmetingen aan DNA-import door bacteriofaag ϕ29. De resultaten van het eiwittranslocatieproject zijn te vinden in Hoofdstuk 2.

Het onderzoek van het Amsterdam-Groningenteam richtte zich nu op een project waarin we, met behulp van de optisch-pincetopstelling, het effect van het eiwittranslocatie-gerelateerde chaperonne-eiwit SecB op de vouwing en ontvouwing van één enkel eiwit (MBP) wilden onderzoeken. Ook bij dit project werden moleculaire constructen gemaakt in Groningen, voornamelijk door Philipp Bechtluft, terwijl de optisch-pincetmetingen werden verricht in Amsterdam. Het effect van chaperonne-eiwit SecB was erg duidelijk, maar in het ontvouwen van het eiwit MBP zagen we bepaald gedrag dat we niet konden verklaren vanuit de bestaande literatuur. Om deze reden zochten we contact met Harald Tepper, die vervolgens moleculaire-dynamicasimulaties verrichtte aan het ontvouwen van MBP. Ondanks de vele ordes van grootte verschil in tijdsschaal en treksnelheid bleken simulaties en experimenten uiteindelijk zeer goed met elkaar te rijmen te zijn. De resultaten van experimenten en simulaties zijn beschreven in Hoofdstuk 3.

De experimenten aan DNA-import door het virus bacteriofaag φ29 begonnen als vervolg op werk van Sander Tans aan de *University of California* in Berkeley. Met de optisch-pincetopstelling wilden wij het effect van verschillende factoren bestuderen op de DNA-importsnelheid en op de hoeveelheid DNA die geïmporteerd kan worden. Voor dit project zijn verschillende technieken ontwikkeld voor het maken van een DNA-construct voor de optisch-pincetexperimenten. Uiteindelijk ging de aandacht naar het eiwitontvouwingsproject vanwege de interessante resultaten die daar te behalen waren. De resultaten van het DNA-importproject zijn beschreven in Hoofdstuk 4.

◆

Het moge duidelijk zijn dat de inhoud van dit proefschrift in hoge mate te danken is aan samenwerking met verschillende mensen. Hier wil ik dan ook alvast alle mensen bedanken die mij op de een of andere manier hebben geholpen bij het tot stand komen van dit proefschrift.

De samenwerking met Groningen heb ik als zeer prettig en interessant ervaren. De halfjaarlijkse vergaderingen zijn met de jaren en het uitdijen van het team uitgegroeid tot zeer dynamische bijeenkomsten met interessante discussies waar ik erg naar uitkeek. Van het Amsterdam-Groningenteam wil ik allereerst Danka Tomkiewicz bedanken, voor haar wetenschappelijke inbreng en haar humor en enthousiasme tijdens onze gezamenlijke meetdagen. Nico Nouwen heeft met zijn ijver en nauwkeurigheid een essentiële rol gespeeld bij de laatste metingen in het translocatieproject. Verder wil ik hem bedanken voor het feit dat hij van deze natuurkundige een biofysicus heeft gemaakt tijdens mijn bezoek aan Groningen. Philipp Bechtluft begon als verlegen student maar zijn *drive* voor het MBP-project was steeds daar en wordt steeds duidelijker. Dennie Rozeveld wil ik bedanken voor het maken van het 4×MBP-construct. Zonder Matt Tyremans systematische aanpak en doorzettingsvermogen had dit proefschrift er beslist anders uitgezien. Ik ben blij dat hij naast me zit tijdens de verdediging. Aan de discussies die ik met Harald Tepper had over de MBP-kristalstructuur heb ik erg plezierige herinneringen. Verder wil ik hem bedanken voor zijn kritische blik op het manuscript van dit proefschrift.

Voor het DNA-importproject wil ik Shelley Grimes bedanken van de *University of Minnesota* voor het leveren van virale eiwitten en DNA. Roland Dries wil ik bedanken voor zijn hulp bij het maken van het DNA-construct.

Verder wil ik nog een aantal mensen bedanken die betrokken zijn geweest bij het bouwen van de optisch-pincetopstelling. Allereerst Steve Smith van de *University of California* in Berkeley voor zijn optisch-pincet ‘boodschappenlijstje’. Ik wil verder Astrid van der Horst op AMOLF, en Christoph Schmidt en Gijs Wuite van de Vrije Universiteit Amsterdam bedanken voor de vele praktische tips voor het bouwen van een optisch-pincet. Thomas Kalkbrenner wil ik bedanken voor zijn *gründliche* inbreng bij het uitlijnen en herbouwen van de opstelling. In de groep *Bio-assembly and organization* van Marileen Dogterom was toen ik begon al veel kennis van algemene experimenteel-biofysische problemen. In de gezamenlijke meetings en in lab 007 heb ik daar veel van mogen profiteren. Met name wil ik hiervoor Martijn van Duijn, Jacob Kerssemakers en Gerbrand Koster bedanken. Uiteraard mogen in dit rijtje alle technische afdelingen van AMOLF niet ontbreken. Graag wil ik hen bedanken voor alle hulp in de vorm van technische tekeningen, onderdelen op maat, elektronica en Labview-tips.

Vanwege de focus op de brede ontwikkeling van zijn werknemers heb ik AMOLF ervaren als een erg prettig instituut om mijn promotieonderzoek te doen. Ook tussen de experimenten en colloquia door was het een fijne werkplek, en dan in het bijzonder de – binnenkort legendarische – overloop. Het onderzoek in de Biofysica-groep was divers, maar er heerste wel een zeer prettige collegiale sfeer. Dank dus aan enkelmoleculers Matt en Thomas, biochemische-netwerkers Aileen, Daan, paranimf Frank en Philip en technici Genison, Kim en Roland. Eva werd consultant; haar consult heb ik – met plezier – aan den lijve mogen ondervinden. Verder wil ik mijn kamergenoten door de jaren heen bedanken: Gerbrand, Ivan, Kim, Pim, Niels en Julien.

De AMOLFers zorgden al voor veel vermaak – ook buiten de muren van het instituut – maar daarnaast waren er nog mijn vrienden en familie voor een leuke tijd naast mijn werk en om op zijn tijd mislukte experimenten te kunnen relativeren. Met name wil ik hier mijn ouders noemen, die mij altijd hebben gesteund en me de vrijheid hebben gegeven om te doen wat ik doe. Tenslotte wil ik mijn vriendin Astrid bedanken voor haar steun en het doorstaan van mijn – sporadische – geklaag en voor haar geduld tijdens het schrijven van dit proefschrift. Het is heerlijk zo'n lieve en eerlijke vriendin als haar te hebben.

RUUD VAN LEEUWEN
Amsterdam, september 2006

1

Optical tweezers

For various single-molecule experiments that will be presented in this thesis, we have built an optical tweezers setup. In this chapter, we will introduce this setup.

1.1 Introduction

This thesis will present experiments on a broad range of biological processes: protein translocation, protein unfolding and the packaging of dsDNA by bacteriophage ϕ29. The common denominator for these experiments is the use of an optical tweezers setup. Optical tweezers are an excellent tool to study the forces and distances inherent in these processes.

Optical tweezers were first demonstrated by Ashkin et al. [1] in 1986 and are based on the central observation that photons carry a momentum $p = h/\lambda$, with h Planck's constant and λ the wave length of the light. Hence, if the direction of a photon is altered, e. g., by scattering or by refraction, a force is exerted on the scatterer or on the refractive interface. On macroscopic objects, this force can be neglected, but on micro- or mesoscopic objects, such as micron-sized polystyrene microspheres, the effect of this force can clearly be observed, if a high-intensity light source such as a laser is used.

Two different optical forces are of importance to optical trapping: the *scattering force* and the *gradient force*. The scattering force on an object is caused by backscattering of photons and acts in the direction of the light beam. The gradient force on an object is pointed in the direction of highest light intensity. This is explained in Figure 1.1. In this figure, a microsphere is shown with an incoming, collimated beam that has an intensity profile as shown on the left (top: high intensity; bottom: low intensity). Of two rays, a bright ray and a dim ray, the path is shown through the transparent microsphere. Due to refraction at the microsphere interface, a force is exerted on the microsphere by the rays because of the change in momentum (see inset for the momentum of the bright ray). For both rays, the direction of forces is indicated, with the size of the arrow indicating the magnitude of the force. It can be seen that the vertical component of the total force on the microsphere is acting upwards, in the direction of highest intensity.

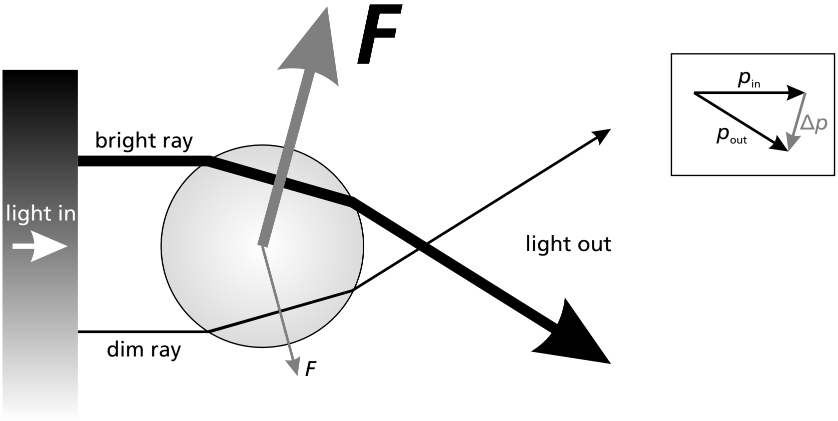

Figure 1.1: Illustration of the gradient force that is exerted on transparent objects by non-homogeneous light beams. From the left of the picture, a collimated beam enters with an intensity profile as indicated (top: high intensity; bottom: low intensity). Of two rays from this beam, the path through a transparent microsphere is shown. Due to refraction at the microsphere interface, the direction of each ray is altered. Because of the change of momentum of the photons that constitute the ray, this results in a force exerted on the microsphere that is bigger for the bright ray than for the dim ray. The net vertical force on the microsphere is therefore pointing upward, in the direction of highest intensity.

When a laser beam is focused on an aqueous suspension of particles with a higher refractive index than water, the gradient force will direct a particle to the point with the highest intensity, i. e., the center of the focus. If a high-numerical-aperture (NA) lens such as a microscope objective is used, the gradient force dominates the scattering force and the particle can stably be trapped in the laser focus. Note that the equilibrium position of the particle is slightly 'off-stream' due to the scattering force. The laser focus can now be used as an optical trap for microspheres, or as *optical tweezers*.

Using a microscope objective, one can combine optical trapping with microscopy. Soon after the first demonstration of optical trapping, Ashkin and Dziedzic showed the first biological application of optical tweezers [2]. Using a laser emitting in the near infra-red (IR), *Escherichia coli* bacteria could be trapped for hours without being damaged. A major advance in optical trapping was the introduction of a force-measuring detector by Svoboda et al. [3]. A microsphere inside an optical trap experiences a force F towards the trap center that varies linearly with the displacement as $F = k_x x$ for small displacements x. The detector introduced by Svoboda et al. could be used both to determine the position of a microsphere in the optical trap and to determine the trap stiffness k_x and hence the force. They coated a silica microsphere with kinesin motor proteins and could thus measure the force exerted by a kinesin molecule advancing on a microtubule.

Optical tweezers have since been used to study many biological systems, e. g., motor proteins myosin [4] and the packaging motor of bacteriophage ϕ29 [5] (see also Chapter 4); a DNA polymerase [6]; the elasticity of DNA [7] (see Appendix A); the unfolding of proteins [8, 9] (see Chapter 3), membrane tube formation [10] and the polymerization of microtubules [11].

Using optical tweezers, forces up to 100 pN can be measured with resolutions as fine as less than 0.1 pN. This rendered it an ideal experimental tool for the biochemical processes studied in this thesis: protein translocation, protein unfolding and packaging of dsDNA by bacteriophage ϕ29. For these experiments, we built an optical tweezers setup. We used an approach using two polystyrene microspheres, of which one was optically trapped and one was held by a glass micropipette that was introduced in the microscope sample. Both microspheres were coated with different biological molecules. By pushing the micropipette microsphere against the optically trapped microsphere, connections could be made between the two microspheres, e. g., between a streptavidin tetramer on the micropipette microsphere and a biotinylated DNA molecule on the optically trapped microsphere. By varying the distance between the microspheres, the force on the molecule of interest could now be tuned. We developed a sophisticated flow system that enabled fast replacement of both microspheres for a new measurement. This enabled a high throughput in our measurements, something that is of key importance to acquire good statistics in single-molecule studies.

In this chapter, our optical tweezers setup will be described in detail. Furthermore, the flow system will be introduced and we will describe how forces were measured using our setup.

1.2 Optical tweezers setup

Figure 1.2 shows a schematic drawing of the optical tweezers setup that was used in the experiments presented in this thesis. In this setup, two beam lines can be distinguished: (I) the trapping beam line (in white), from the laser, via objective and condenser, to the quadrant photodiode (QPD) and (II) the imaging beam line (in gray), from the LED, via condenser and objective to the two CCD cameras.

As a trapping laser, a Nd:YVO_4 laser (Spectra physics, λ = 1064 nm, 5.4 W) is used. This wave length was chosen such that it could be well separated from the light that was used for imaging the sample. Moreover, absorption and scattering in biological materials is minimized when using infra-red (IR) light. The trapping beam is expanded 10× using a Galilean beam expander (BE10X-C, Thorlabs). Next, a rotatable $\lambda/2$ waveplate (Thorlabs), in combination with a polarizing cube beamsplitter (Newport) and a beam block (Thorlabs), is used to attenuate the laser light. Using the cube beamsplitter and a mirror (Thorlabs), the laser light is coupled into a second beam expander, consisting of two lenses (Edmund Optics, f = -25 mm, f = 50 mm), that expanded the beam another 2×, resulting in a laser beam of ~8.4 mm in diameter. Via a mirror (Thorlabs), the beam is coupled in a ∅50 mm

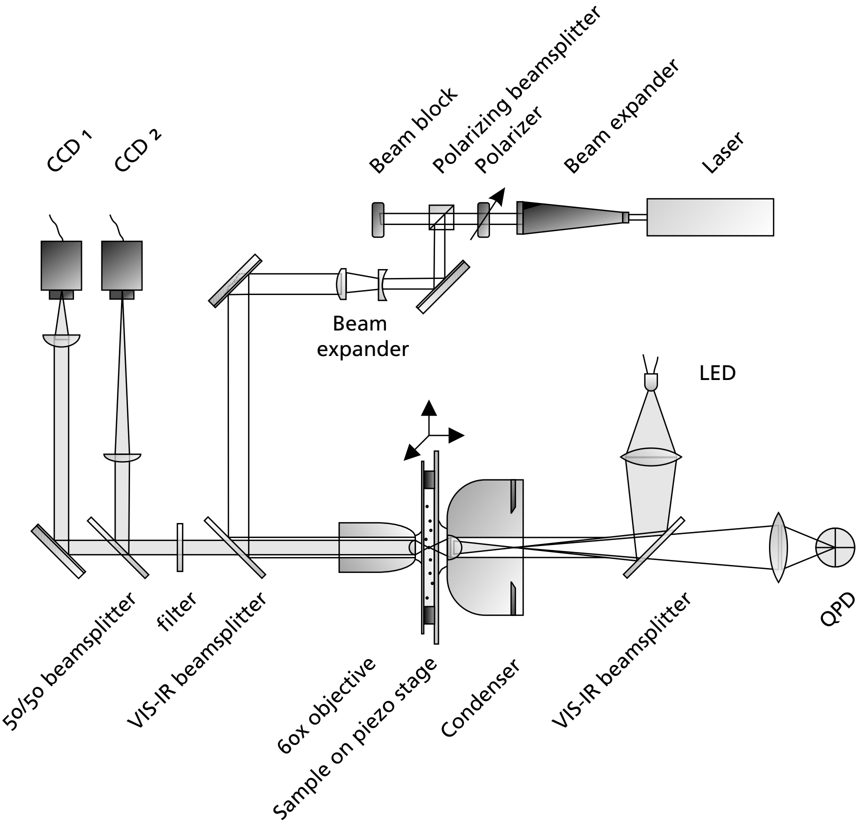
CCD 1
CCD 2
Beam block
Polarizing beamsplitter
Polarizer
Beam expander
Laser
Beam
expander
LED
50/50 beamsplitter
filter
VIS-IR beamsplitter
60x objective
Sample on piezo stage
Condenser
VIS-IR beamsplitter
QPD

Figure 1.2: Schematic drawing of the optical tweezers setup. A 60× water-immersion objective is used for imaging and trapping. A blue LED is used for illumination of the sample. Two cameras are used to observe the sample at different magnification. A Nd:YVO_4 laser is used as a trapping laser. A quadrant photodiode (QPD) is used for detection of trapping forces.

VIS-IR beamsplitter, that is used to reflect the laser beam into the back aperture of a 60× water-immersion objective lens (Nikon CFI Plan-Apochromat, NA = 1.2) that is used both for imaging and to focus the laser in the specimen plane. The laser beam is slightly overfilling the 8-mm objective back aperture for maximal trapping potential. After the focus, the laser beam is collected using an oil-immersion condenser lens (Nikon, NA = 1.4). Using a positive lens (f = 50 mm), the back-focal plane of the condenser is imaged onto a quadrant photodiode (QPD, SPOT-9DMI, OSI Optoelectronics). All lenses in the trapping beam line were purchased with an IR anti-reflective coating. In the early experiments with this setup, a diode laser (Spectra Diode Labs, λ = 830 nm, 500 mW) was used as a trapping laser, but because of the low power, it was replaced by a stronger Nd:YVO_4 laser.

In the imaging beam line, a blue LED (Toyoda Gosei, λ = ~470 nm) was used for the illumination. Using a bi-convex lens (Newport, f = 75.6 mm), the LED diode is imaged in the back-focal plane of the condenser lens to illuminate the microscope sample. A ∅50 mm VIS-IR beamsplitter is used to reflect the blue light into the condenser, while transmitting the trapping beam. The objective lens was used to image the sample. The polarizing beamsplitter at the objective lens back aperture transmitted the blue light. A filter (Melles Griot) was used to prevent reflected laser light from reaching the cameras. Via a 50/50 plate beamsplitter (Melles Griot) and a mirror (Thorlabs), the light is directed to two separate CCD cameras (Watec), onto which the sample is imaged at different magnifications using two lenses (f = 20 cm, 40 cm).

All components were mounted on an actively-damped optical breadboard such that all beams were parallel to the table surface (beam height 11 cm). The use of beams perpendicular to the surface would involve using tall, upright-standing components that could introduce artifacts in measurements because of vibrations. The microscope sample was mounted on a piezo-nanopositioning stage (P-517.3CL, Physik Instrumente) that permitted translation both in the perpendicular (x [parallel to breadboard] and y [perpendicular]) and in the longitudinal (z) direction of the trapping beam. The x and y range of the piezo stage was halved as to increase the accuracy of positioning, resulting in a range of 50 µm × 50 µm × 20 µm ($x \times y \times z$). The piezo stage was mounted on the table via a manually-controlled linear stage (Newport) and a custom-made flexure stage to allow coarse movements of the microscope sample in the x and z directions, respectively. The objective lens was mounted on a precision linear stage (M-561D-XYZ-LH, Newport) to allow precise positioning of the objective lens in three dimensions with respect to the trapping beam and the microscope sample. The condenser was mounted on the breadboard via a linear stage (Newport) and a kinematic base (Newport) to allow movement in the z direction and to allow replacing the condenser with high repeatability between experiments, respectively. Most other components of the setup were mounted on the optical table using Thorlabs mounts and bases. The setup was built in a room where the temperature was maintained constant by an air-conditioning system.

The laser power could be adjusted using the rotatable polarizer and using a

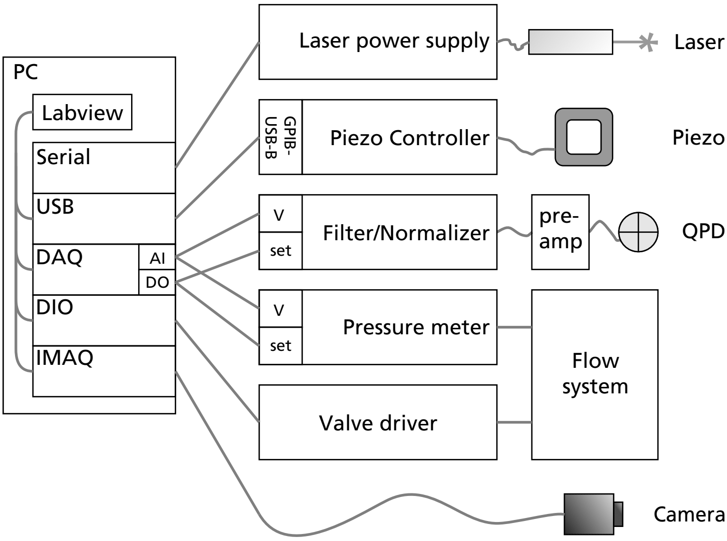

Figure 1.3: Control of the optical tweezers setup by a PC. Various components of the optical tweezers setup were controlled by a PC as shown. DAQ: data acquisition board; AI: analog input; DO: digital output; DIO: Digital I/O board; IMAQ: image acquisition board (frame grabber); V: analog signals; set: settings.

personal computer (PC) that was connected to the laser power supply via a serial (RS232) cable (see Figure 1.3). The piezo stage was controlled by a digital piezo controller (E-710.P4L, Physik Instrumente) that was connected to the PC via the USB port via a GPIB controller for USB (GPIB-USB-B, National Instruments). The voltages of the four QPD elements (numbered 1...4 from left to right and top to bottom) were pre-amplified and converted to voltages V_x (equal to $[V_2 + V_4] - [V_1 + V_3]$), V_y (equal to $[V_3 + V_4] - [V_1 + V_2]$) and V_{sum} (equal to $V_1 + V_2 + V_3 + V_4$) by analog electronics on the printed circuit board (PCB) that also contained the QPD detector. Next, the QPD V_x and V_y signals were normalized with the V_{sum} signal, filtered by a 5th-order Butterworth low-pass anti-aliasing filter, and further amplified using a second analog electronics circuit. The amplification and the filter frequency of the anti-aliasing filter could be manually controlled. Additionally, the filter frequency could be digitally controlled by the PC (range 10–50,000 Hz). All analog electronic circuits were designed and manufactured by Henk Dekker at AMOLF. The normalized QPD signals were recorded by the PC using the analog input (AI) channels of a multifunction data acquisition (DAQ) board (PCI-6052E, National Instruments). The digital output (DO) channels of the DAQ board were used to control the anti-aliasing filter frequency. The DAQ board also controlled a pressure meter that was used in the flow system that will be introduced later in this chapter. A digital I/O (DIO) board (PDL-DIO-64, United Electronic Industries) controlled the

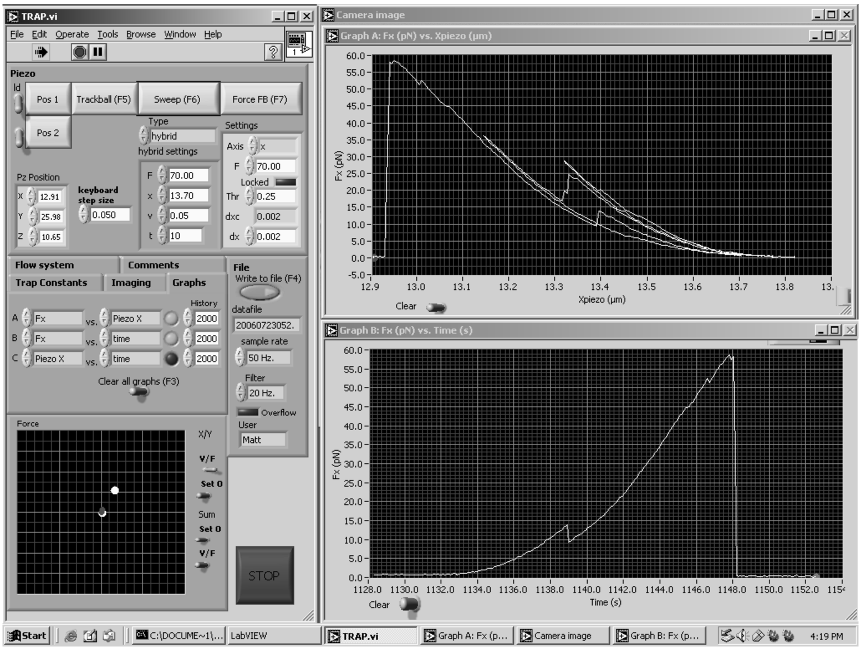

TRAP.vi
File Edit Operate Tools Browse Window Help
Piezo
Id
Pos 1
Pos 2
Trackball (F5)
Sweep (F6)
Force FB (F7)
Flow system
Comments
Trap Constants
Imaging
Graphs
History
Clear all graphs (F3)
File
Write to file (F4)
Overflow
Force
X/Y
V/F
Set 0
Sum
Set 0
V/F
STOP
Camera image
Graph A: Fx (pN) vs. Xpiezo (µm)
Fx (pN)
60.0
55.0
50.0
45.0
40.0
35.0
30.0
25.0
20.0
15.0
10.0
5.0
0.0
-5.0
12.9
13.0
13.1
13.2
13.3
13.4
13.5
13.6
13.7
13.8
13.
Xpiezo (µm)
Clear
Graph B: Fx (pN) vs. Time (s)
Fx (pN)
60.0
55.0
50.0
45.0
40.0
35.0
30.0
25.0
20.0
15.0
10.0
5.0
0.0
1128.0
1130.0
1132.0
1134.0
1136.0
1138.0
1140.0
1142.0
1144.0
1146.0
1148.0
1150.0
1152.0
115
Time (s)
Clear
Start
C:\DOCUME~1\...
LabVIEW
TRAP.vi
Graph A: Fx (p...
Camera image
Graph B: Fx (p...
4:19 PM

Type: hybrid
hybrid settings
F 70.00
x 13.70
v 0.05
t 10

Settings
Axis x
F 70.00
Locked
Thr 0.25
dxc 0.002
dx 0.002

Pz Position
X 12.91
Y 25.98
Z 10.65

keyboard step size 0.050

A Fx vs. Piezo X 2000
B Fx vs. time 2000
C Piezo X vs. time 2000

datafile 20060723052.
sample rate 50 Hz.
Filter 20 Hz.
User Matt

Figure 1.4: A screenshot of the used Labview program, `TRAP.vi`. The main window (left) and two graph windows (right) are shown.

valve drivers (NResearch) that were needed to control the valves in the flow system. Images from the CCD camera with the highest-magnification image were recorded by the PC using a frame grabber (PCI-1407, National Instruments). Images from both cameras could be visualized using a monochrome monitor.

On the setup PC, a Labview (National Instruments) program was run that could simultaneously control the piezo stage, the anti-aliasing filter, the pressure meter and the flow system controller, and acquire QPD, pressure meter and camera signals. A screen capture of the Labview program (`TRAP.vi`) is shown in Figure 1.4. In this screen capture, the main control window is shown on the left. Up to three resizable graph windows can be shown to visualize data in real-time. This program was used to determine calibration constants of the optical trap, i. e., force constants k_x and k_y (in pN/µm) and QPD sensitivities S_x and S_y (in V/µm). More about determining these constants will be shown later on in this chapter. If a microsphere is trapped, these calibration constants can be used to calculate forces F_x and F_y from the QPD V_x and V_y signals. The program was also used to control movement of the piezo stage in several ways: (I) in the trackball mode, movement of the piezo stage in the x, y and z direction is controlled directly by a trackball (Logitech). (II) In the force-feedback mode, the piezo stage is moved such that the force on an optically-trapped microsphere is kept constant. (III) In the sweep mode, the piezo stage is moved in one of several pre-programmed patterns, e. g., at constant speed (μm/s) between two forces F_{min} and F_{max}. Using a Labview single-particle tracking (SPT) algorithm, the x and y position of two microspheres on the camera image could be determined. If wanted, the data was written to disk (t [in seconds], x_{piezo}, y_{piezo}, z_{piezo} [in μm], $x_{\mathrm{SPT},1}$, $y_{\mathrm{SPT},1}$, $x_{\mathrm{SPT},2}$, $y_{\mathrm{SPT},2}$ [in pixels], V_x, V_y and V_{sum} [in Volts]). After calibration, parameters were written to disk and additionally, user comments could be written to disk during measurements.

1.3 Force detection

To detect the movement of a microsphere inside the trap focus, we placed a quadrant photodiode (QPD) in a conjugate optical plane of the back-focal plane of the condenser lens. Due to movement of an optically trapped microsphere in the trapping focus, the outgoing laser beam varies with the position of the microsphere. The pattern that is measured at the QPD represents the angular-intensity distribution of light that has passed through the focus [12]. For small displacements of the microsphere from the trap center, there is a linear relationship between the detector voltages V_x, V_y, V_z and displacements x, y and z, respectively. Alternatively, a camera image was used to detect the position of a microsphere at a lower frequency (25 Hz vs >1000 Hz). Labview pattern recognition algorithms were used here to find microspheres in a camera image.

Next, we describe how we could use the QPD to detect forces exerted on an optically trapped microsphere. To a dielectric microsphere of, e. g., polystyrene or glass, a focused laser spot acts as an attractive potential well with an equilibrium position near the focus. If the microsphere remains close to the equilibrium position, the optical trap can be regarded as a Hookean spring, and the force exerted on the microsphere (in the x direction) can be described by $F = k_x(x - x_0)$, with k_x the trap stiffness and x_0 the position of the trap center. For the y and z direction, the same relation holds (for a well-aligned setup, $k_x \approx k_y$; k_z is generally smaller by a factor of 10). To find k_x, several methods can be used [13]. We used the power spectrum method. For this method, we measured displacement fluctuations $x(t)$ of a trapped microsphere. The power spectral density (PSD), or one-sided power spectrum $2|X(f)|^2$, where $X(f)$ denotes the Fourier transform of $x(t)$, of these fluctuations is approximately Lorentzian [12, 13], and is given by:

$$\mathrm{PSD}(f) = \frac{k_{\mathrm{B}} T}{\pi^2 \gamma (f_{\mathrm{c}}^2 + f^2)}, \tag{1.1}$$

where k_{B} is the Boltzmann factor, T is the temperature, $\gamma = 3\pi\eta d$ is the Stokes drag coefficient for a sphere of diameter d immersed in a fluid of viscosity η and $f_{\mathrm{c}} = k_x/2\pi\gamma$ is called the corner frequency. Trap constant k_x can now be found by fitting a Lorentzian to the measured PSD, using, e. g., Labview, to find the corner frequency. Note that the QPD detector does not directly measure the microsphere displacement, but rather a voltage signal. Because of the linear relation

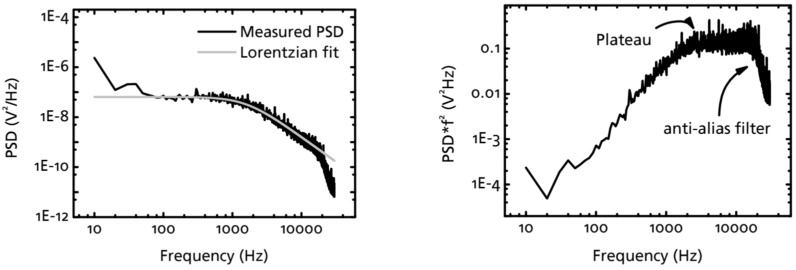

(a) (b)

Figure 1.5: (a) Averaged power spectral density of an optically trapped 1.88 µm-sized microsphere. Data has been fitted using a lorentzian curve (shown in gray) to acquire the corner frequency f_c and trap stiffness κ. (b) The PSD of Subfigure (a) has been multiplied by f^2. The height of the resulting plateau (in V^2 Hz) can be used to get the trap sensitivity.

of the detector signal $V_x(t) = S_x x(t)$ for small displacements $x(t)$, the PSD of the detector signal $\mathrm{PSD}^V(f)$ is given by:

$$\mathrm{PSD}^V(f) = 2|V_x(f)|^2 = 2S_x^2|X(f)|^2 = S_x^2\mathrm{PSD}(f) = S_x^2\frac{k_\mathrm{B}T}{\pi^2\gamma(f_\mathrm{c}^2+f^2)}, \qquad (1.2)$$

and one can see that k_x can be found even without knowing the detector sensitivity S_x. The detector sensitivity does not alter the value for the corner frequency f_c that is found by fitting.

Figure 1.5a shows an example of the power spectral density $\mathrm{PSD}^V(f)$ of an optically trapped 1.88-µm polystyrene microsphere. A Lorentzian fit is plotted in the same figure.

The detector sensitivity S_x (in V/µm) can now be found by multiplying both sides of Eq. 1.2 by f^2:

$$f^2\mathrm{PSD}^V(f) = f^2S_x^2\frac{k_\mathrm{B}T}{\pi^2\gamma(f_\mathrm{c}^2+f^2)}, \qquad (1.3)$$

At high frequencies, this function is given by:

$$\lim_{f\to\infty} f^2\mathrm{PSD}^V(f) = S_x^2\frac{k_\mathrm{B}T}{\pi^2\gamma}, \qquad (1.4)$$

showing that at high frequencies, $f^2\mathrm{PSD}^V(f)$ will reach a plateau value that can be used to calculate sensitivity S_x. Figure 1.5b shows function $f^2\mathrm{PSD}^V(f)$. The plateau can clearly be observed. Also a drop can be seen at even higher frequencies due to the anti-aliasing filter.

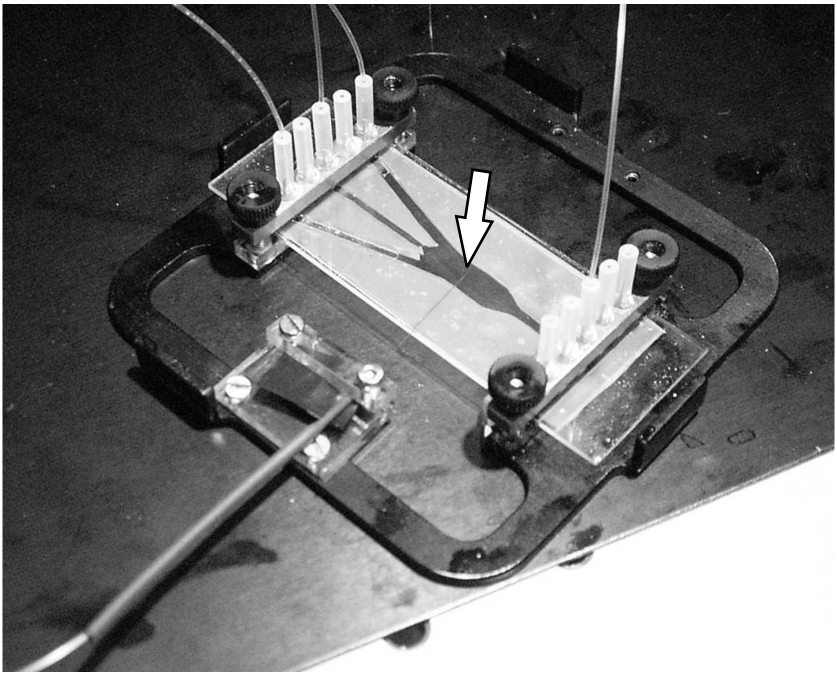

Figure 1.6: An example of the sample holder that was used in experiments. The arrow points at the position of the micro-pipette tip.

Knowing the trap stiffness k_x and the detector sensitivity S_x, we can calculate force F_x from the detector x signal V_x using:

$$F_x = k_x / S_x \cdot V_x .$$

1.4 Flow system

For the experiments that are described in this thesis, a flow system was developed that enabled precise control of the buffer conditions and flow speed during different stages of an experiment. In single-molecule biophysics, a high number of experiments has to be performed for sound statistics, so a flow system enabling a high measurement throughput was essential.

In Figure 1.6, an example of a flow cell is shown with the custom-made sample holder that we used to mount the flow cell on the piezo stage. The sample holder was mounted on the piezo stage such that it could be moved in the x and y directions to align it with the trapping focus. Figure 1.6 shows a flow cell with three inputs (left) and one output (right). Polyethylene tubing was used to connect the in- and outputs

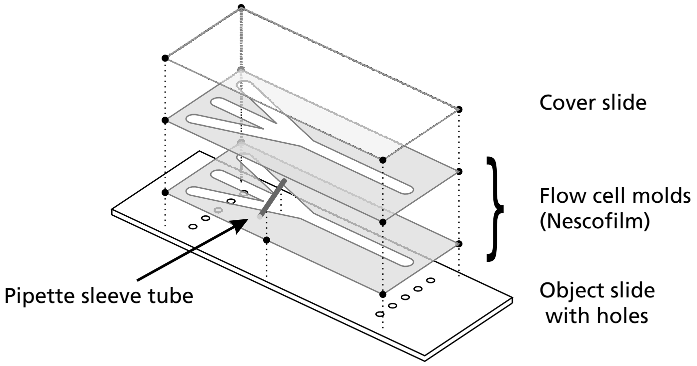

Figure 1.7: Flow cell assembly procedure. All components are stacked as shown and heated to create a tight seal between glass and Nescofilm.

to syringes filled with buffer. The flow from these syringes to the flow cell could be controlled either manually, using a plunger, or using a computer-controlled flow system. Between the flow cell and the syringes, manually-controlled valves (Hamilton) were introduced to enable switching between buffers or to completely block channels. The arrow in Figure 1.6 points at the micropipette tip (not visible on this scale). This micropipette was connected to a manually-controlled syringe via polyethylene tubing (bottom left).

Figure 1.7 shows a schematic illustration of the flow cell assembly procedure. Object slides (Menzel Gläser), and cover slides (24 mm × 60 mm, Menzel Gläser) were washed using a detergent solution (10% Hellmanex II, Hellma) and rinsed with water. The object slides contained ten ∅1-mm holes that were drilled in the slides using a diamond drill. Flow cell molds were cut by hand from Nescofilm (Karlan). A micropipette sleeve tube was cut from a Microfil needle (outer diameter [OD]: 164 µm; inner diameter [ID]: 100 µm, World Precision Instruments) and the flow cell was assembled as shown. The flow cell was sandwiched between two clean object slides and transferred to a hot plate that was pre-heated at 150°C. While applying pressure, the flow cell was heated until the Nescofilm melted, forming a tight seal with the glass.

Most experiments described in this thesis were performed using a glass micropipette. Micropipettes were made using a custom-made pipette-pulling apparatus. To make a micropipette, a hollow glass fiber (OD: 80 µm; OD: 40 µm, Garner Glass Company) was locally heated circumferentially using a glowing platinum filament (∅700 µm). Upon melting of the fiber, the two ends of the fiber on both sides of the filament were pulled apart by a weight that was attached to one side of the fiber. This resulted in a strongly-tapered micropipette tip with an inner diameter of ~1 µm at one of the two ends. The micropipette was connected to polyethylene tubing using heat-shrink tubing and a hot-air gun. It was introduced in the micropipette sleeve tube using a bench-top stereo microscope.

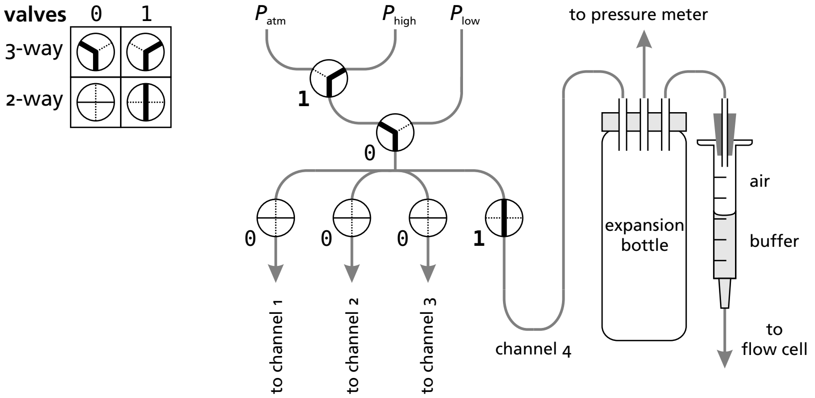

Figure 1.8: Schematic diagram of the flow system that was used to control the flow speed of buffers in the flow cell. Buffer flow out of the syringe (right) was regulated by varying the pressure inside the syringe. This was done by briefly switching the six two- and three-way solenoid valves such that the syringe was connected to either a compressor (P_{high}), a vacuum pump (P_{low}), or atmospheric pressure (P_{atm}). Here, it is shown how the syringe is briefly connected to P_{high}. Channels 1–3 are equal to channel 4.

Figure 1.8 shows a schematic diagram of the flow system that was used to control the flow from each of the syringes to the flow cell input channels. By changing the pressure in the syringe, the flow to the flow cell was changed. To change the pressure, two three-way solenoid valves and four two-way solenoid valves (NResearch) were switched using the DIO board in the PC and the valve drivers, such that the syringe was temporarily connected to either a compressor (P_{high}), a vacuum pump (P_{low}), or atmospheric pressure (P_{atm}). Figure 1.8 shows how the syringe is temporarily connected to P_{high} by sending a '1' to two of the six valves using the DIO board. This results in a flow of air between P_{high} and the syringe, leading to an increased pressure in the syringe and a higher flow from the syringe to the flow cell. An expansion bottle (~50 ml) was introduced between the valves and the 3-ml syringe (Terumo) to keep the pressure approximately constant as the buffer meniscus moves downwards during buffer flow. Teflon tubing was used to connect valves, bottles and syringes. A silicon stop (with a hole for the teflon tubing) was used to close the syringe. The expansion bottle was connected to a pressure meter. This pressure meter was developed by Idsart Attema at AMOLF. Four separate pressures could be measured one at a time, using the PC DAQ board. To switch between channels, a digital signal was sent to the pressure meter, using the DO channels of the DAQ board.

The flow cell design that was shown in Figure 1.7, with three inputs and one output, was the design that was used most often in experiments, but other flow cell designs, with additional in- and/or outputs were also used. In the three-input flow cell, the outermost channels were connected to syringes with microsphere

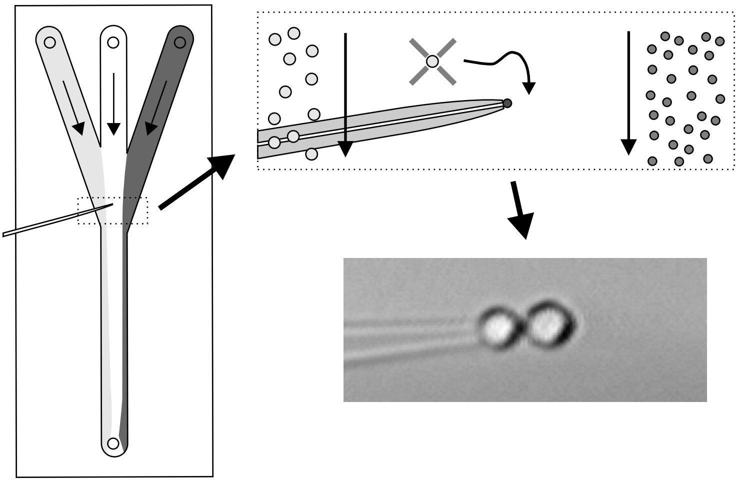

Figure 1.9: Schematic illustration of laminar flow inside a flow cell. Left: from the three input channels, different buffers are flown in: a microsphere suspension, the experimental buffer and another microsphere suspension. Because of the small dimensions, the flow inside the flow cell is laminar and the three flows do not mix. Top right: microspheres are caught from their respective flows and transferred to the micropipette in the middle of the channel. Bottom right: micrograph of an optically trapped 2-µm microsphere (right) and a microsphere that is being held by a micropipette (left).

suspensions. The middle channel was used for the experimental buffer. Because of the small internal dimensions of the flow cell (typically 5 mm wide; 100 µm deep) and hence the low Reynolds number, no mixing occurs of the three input flows (except for some diffusion) and the flow is laminar. This phenomenon is illustrated in Figure 1.9. In the zoomed-in representation, one can see the two microsphere flows and the experimental buffer flow in parallel. In a typical experiment, the optical trap was used to catch microspheres from their respective flows. This was done by moving the flow cell using the piezo stage and the manual linear stage on which the piezo stage was mounted. After catching a microsphere, it could be transferred to the micropipette tip, where it could be held through suction. Next, a microsphere was caught from the other microsphere flow and an experiment could be started (see micrograph in Figure 1.9) by making the two microspheres touch and probing for connections via, e. g., DNA strands and proteins. If no connection could be obtained, the microspheres could be removed from either micropipette or optical trap and new microspheres could be caught.

Forces exerted on the trapped microsphere were calculated as described in the previous section. In the next chapters, measurements will be shown with on the horizontal axis the distance between the two microspheres, the extension x. This extension was calculated using the piezo stage x_{pz} value, the detector V_x signal and the calibrated sensitivity S_x using:

$$x = (x_{\mathrm{pz},0} - x_{\mathrm{pz}}) - \frac{V_x}{S_x},$$

with $x_{\mathrm{pz},0}$ the position of the piezo stage when the optically trapped microsphere and the micropipette microsphere are just touching (i. e., the optically trapped microsphere is still [approximately] in the middle of the optical trap).

2

Towards optical tweezers measurements on protein translocation

We have performed optical-tweezers experiments, aiming to measure protein translocation by the E. coli *Sec translocase on the single-molecule level. In this chapter, we will present our progress.*

2.1 Introduction

Proteins are synthesized inside the cell. In order to be functional some of them need to be translocated to different compartments in- or outside the cell. In bacteria a special signal sequence, at the N terminus of a protein (then called preprotein), directs it to the translocation pathway. In *Escherichia coli*, the main translocation pathway via the inner membrane to the periplasm, outer membrane or outside the cell (see Figure 2.1 for a schematic illustration of *E. coli*) is through the protein conducting pore named translocase [14]. The main components of the translocase are the membrane protein complex SecYEG and the motor protein SecA (see Figure 2.2). Energy for transport can be derived from two sources: chemical energy from ATP hydrolysis by SecA and the difference in membrane potential, the so-called proton motive force (PMF) [15, 16, 17]. Just after or during synthesis by the ribosome, a preprotein interacts with cytosolic chaperone SecB, which keeps the preprotein in a so-called translocation competent state (by preventing folding to the native state) and directs it to the translocase-bound SecA [18, 19]. According to the stepwise model, binding of ATP to SecA releases the SecB chaperone and drives the translocation of about 40 amino acids of the preprotein [20, 21, 22]. Next, ATP is hydrolyzed, resulting in the release of SecA from the translocase. Subsequently, the preprotein can be further translocated using the energy from the proton motive force or SecA can bind again and drive the next step of translocation. During translocation, the signal sequence is exposed to the periplasm where it is cleaved off by a protein termed signal peptidase, leaving a mature form of the protein. For review articles on the Sec translocase, see Driessen et al. [23] and de Keyzer et al. [24]

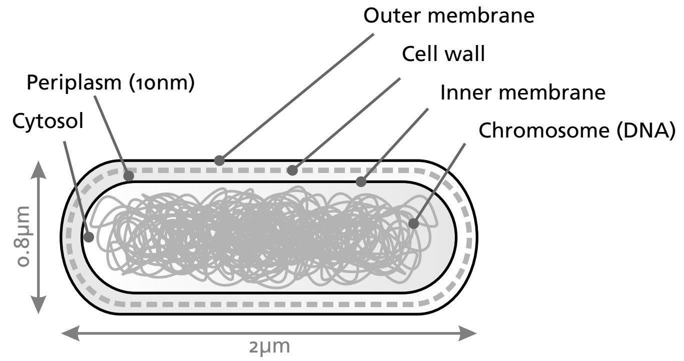

Figure 2.1: Schematic illustration of *E. coli*, showing the location of different compartments and membranes in the cell. NB: the periplasmic space is not drawn to scale. Its width is twice the thickness of the inner membrane.

The Sec pathway is one of the best known and studied translocation machineries. The system is highly conserved throughout nature and directs the translocation of the bulk of secretory proteins in prokaryotes as well as in eukaryotes. Biochemical studies have shown that bacterial translocation is a highly dynamic process, driven by both the motor protein SecA and the proton motive force. Furthermore, various conformational changes and protein-protein interactions play a role in translocation. The structures of individual proteins and complexes involved in the protein transport were recently resolved (SecA [25], SecB [26], SecY complex [27]).

Despite the large body of experimental data, many fundamental questions still remain. One of the central questions is: what is the exact mechanism behind the translocation process? For instance, does protein translocation follow the 'power stroke' model, in which a preprotein is actively pushed through the SecYEG pore upon hydrolysis of ATP by SecA? One can also ask: does it indeed happen in a stepwise fashion? What is the force exerted on the preprotein during translocation? Does the energy from ATP hydrolysis play a role in the active unfolding of the preprotein prior to translocation? What is the exact step size after ATP hydrolysis? An alternative model for the translocation process is the 'thermal ratchet' model. In this model, it is Brownian motion of the translocated protein that drives the translocation, while SecA only provides the directionality to this process by preventing backsliding of the preprotein [28]. Such a model predicts that the physicochemical properties of a preprotein, like folding characteristics and amino acid composition, can have a big impact on the speed of translocation. The expected steps during translocation by Brownian motion, are expected to be of variable size, depending on the type of preprotein.

With the purpose of finding the answers to those questions, we decided to employ a recently developed technique—optical tweezers—in order to investigate preprotein transport at the single-molecule level. Bulk experiments cannot access

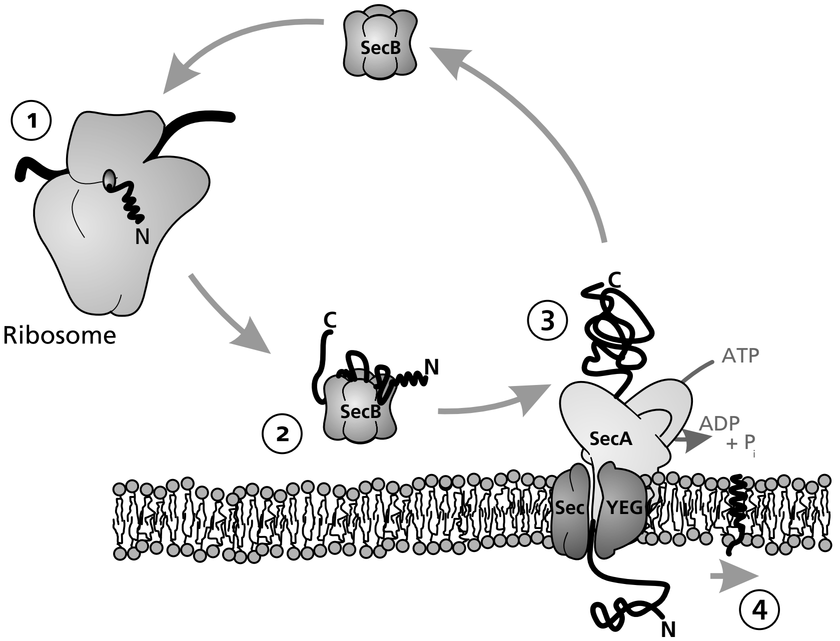

Figure 2.2: Protein translocation through the *E. coli* inner membrane shown in a step-by-step manner. In this picture, the cytosol is located above the membrane and the periplasm below. At (1), the ribosome is shown, translating mRNA to a preprotein. Preproteins that are destined for translocation have a signal sequence at their N terminus. Here, it is shown as a zigzag line. Before the preprotein can reach a stable fold, it is recognized by chaperone protein SecB, that keeps it in a translocation-competent state (2). Next, SecB and the preprotein signal sequence are recognized by the translocation apparatus at (3), and the preprotein is translocated through a pore in protein complex SecYEG. This process is driven by the proton motive force and by ATP hydrolysis of motor protein SecA. During translocation, the signal sequence is cleaved off the preprotein (4).

the behavior of a single preprotein. Moreover, using optical tweezers, we might be able to measure the forces and movements during actual translocation events. In our experimental approach, a well characterized *in vitro* assay was adapted for single-molecule measurements of protein translocation. The followed approach is summarized in the schematic picture of Figure 2.3. In our approach, we used a number of molecular constructs that we will introduce next:

Inner membrane vesicles (IMVs) The standard *in vitro* translocation activity assay uses vesicles made from the inner membrane of *E. coli*. These inside-out vesicles (IMVs) have the *cis* side of the SecYEG translocase facing outside, so preproteins are translocated to the inside of the vesicles. For our optical tweezers experiments, these IMVs are an ideal means to handle SecYEG-containing

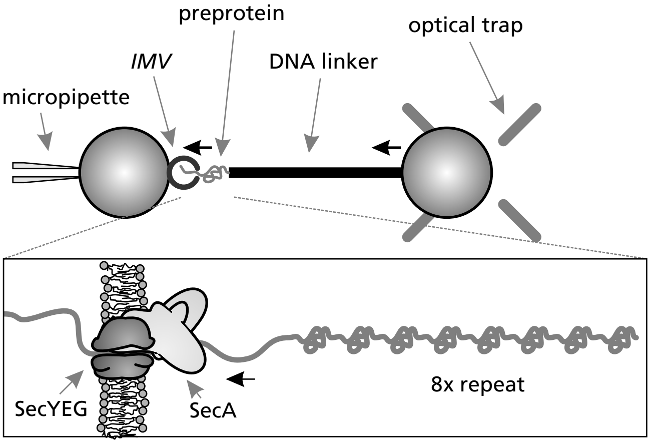

Figure 2.3: Schematic representation of the proposed optical trapping configuration to enable single-molecule measurements on protein translocation. The bottom picture shows how a preprotein with 8 repeats of a subdomain is translocated into phospholipid membrane vesicles made from the inner membrane of *E. coli* (imvs). The black arrows indicate the direction of translocation.

membrane. Previous work suggested an expected step size during translocation of 40 amino acid residues, corresponding to around 13 nm of unfolded polypeptide chain per step. A potential problem is the following: if the membrane containing the studied translocase is too compliant, such steps will only result in a deformation of the membrane, rather than movement of the optically trapped microsphere that is used as a force probe in the optical tweezers setup. In order to get sufficient stiffness of the membrane, the vesicles were resized to 100 nm. Our experiments will show that indeed, no compliance of these small vesicles can be detected in our measurements.

Preprotein construct As a substrate for protein translocation, proOmpA-P8, a proOmpA derivative, was constructed. ProOmpA is intensively studied in *in vitro* protein translocation experiments. This enables a comparison between bulk and single-molecule experiments. For our experiments we constructed a proOmpA derivative containing 8 repeats of the periplasmic domain: proOmpA-P8. Fully extended, the length of the proOmpA-P8 polypeptide amounts to 320 nm, four times the length of proOmpA. In a separate bulk study using proOmpA-P8, we showed that the translocation rate (in pmol/min) for proOmpA-P8 is four times lower than for proOmpA [29]. Hence, it could be concluded that for the Sec translocase, the translocation rate per amino acid, in the absence of pmf, is constant. Therefore, the use of proOmpA-P8 allows for a longer measurement time and, additionally, it could lead to better statistics by introducing repetitive features in translocation measurements.

DNA linker To increase the distance between the trapped microsphere acting as a force probe and the proteins of interest (SecYEG, SecA, SecB, proOmpA-P8), an 800 nm DNA spacer was introduced between the microsphere and the translocated protein. This way, non-specific interactions between the trap microsphere and proteins are avoided. Moreover, the IMV microsphere is too far away from the laser focus to significantly affect measurements on the trapped microsphere. The use of a DNA linker introduces additional compliance, but this is well understood and can easily be subtracted from the data.

Figure 2.3 shows schematically how, in our approach, translocation of a preprotein from the outside to the inside of an IMV, results in movement of the optically trapped microsphere inside the optical trap (black arrows). This movement can then be detected using the deflected outgoing laser beam and the quadrant photodiode (QPD, see Chapter 1).

Beside this two-microsphere/DNA linker/micropipette, we explored an approach employing only one microsphere and no DNA linker and micropipette, also the results reached using this approach will be discussed in this chapter.

Many steps towards the experimental configuration that is sketched in Figure 2.3 have been finished successfully. However, due to technical difficulties, protein translocation measurements on the single-molecule level could not be realized as of yet. This chapter will show the successful steps that have been taken and it will discuss the issues that need to be addressed to successfully perform such experiments.

We will also briefly show the results from a separate study we undertook [29] that used our proOmpA-P8 construct to show that ATPase SecA supports a constant rate of preprotein translocation.

2.2 Materials and methods

This section will cover the experimental details of the experiments described in this chapter. It will discuss how we created molecular constructs such as IMVs, preprotein constructs and the DNA linker. Furthermore, the experimental procedures that were needed in our optical-trapping experiments will be described in detail. Results of all the different experiments will be shown in the next section.

Synthesis of IMVs, protein constructs and the DNA linker and most bulk translocation experiments have been performed at the University of Groningen by Danka Tomkiewicz.

2.2.1 Molecular constructs

IMVs Inner membrane vesicles (IMVs) are small liposomes created from the inner membrane of *E. coli* using a French press. They are in an inside-out orientation,

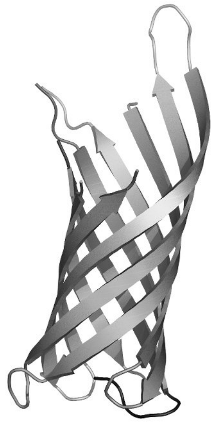

Figure 2.4: Crystal structure of the transmembrane domain of outer-membrane protein A (OmpA; PDB-ID 1QJP [32]). The β-barrel structure that is visible in this picture sits in the outer membrane, with its axis perpendicular to the membrane (periplasmic side down). The periplasmic domain of OmpA could not be crystallized, so is not shown in this picture.

hence the cytoplasmic side of the *E. coli* inner membrane is facing outward. IMVs containing overproduced SecYEG were isolated from *E. coli* strain SF100 [30] containing plasmid pET610 [31], which allows IPTG dependent overexpression of the secYEG genes. The IMVs were extruded through a polycarbonate membrane with 100 nm pores using a LiposoFast extruder (Avestin) in order to get a homogeneous fraction of IMVs with the same size (~100 nm).

Protein expression For our experiments, outer membrane protein proOmpA was used (see Figure 2.4 for the crystal structure). A proOmpA derivative carrying 8 repeats of the periplasmic domain was produced as described before [29] (see Figure 2.5 for a schematic representation): Cysteine-less *ompA* from plasmid pNN208 was cloned into plasmid pUC19, resulting in plasmid pEK200. Next, a cysteine codon was introduced at the extreme 5′ end of the *ompA* gene (pEK201) using the QuikChange™ site-directed mutagenesis kit (Stratagene). Subsequently, two unique restriction sites were introduced: (I) a SalI site at the hinge region between the β-barrel and the periplasmic domain, and (II) a XhoI site just before the cysteine residue at the C terminus (pEK203). The SalI and XhoI restriction sites have compatible cohesive ends that enable the duplication events. To duplicate the periplasmic domain, plasmid pEK203 was digested with EcoRI and XhoI and the fragment encoding OmpA without C-terminal cysteine residue was isolated (fragment A). Digestion of plasmid pEK203 with SalI and EcoRI resulted in a fragment encoding the periplasmic domain with the remaining vector (fragment B). Ligation of both fragments (A+B) results in an *ompA* gene with an additional periplasmic domain and a remaining XhoI restriction site that can be used for introduction of additional periplasmic domains. Using the procedure described above, an *ompA* gene with 2, 4, 6, and 8 in-tandem repeats of the periplasmic domain was obtained (pEK206, pEK208, pEK209, and pEK210, respectively). For overproduction of proOmpA (termed proOmpA-P1) and proOmpA derivatives P2, P4, P6, and P8,

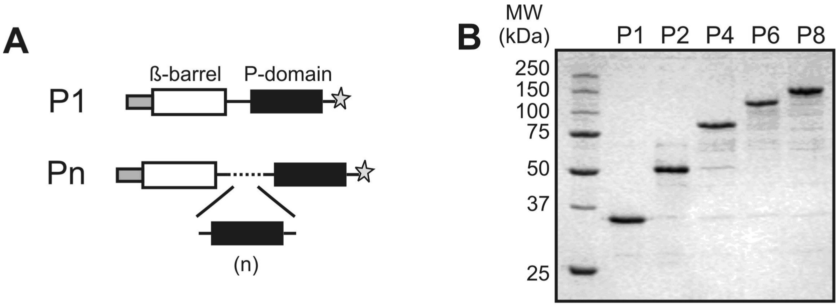

Figure 2.5: Schematic representation and purification of proOmpA derivatives with in tandem copies of the periplasmic domain (n = 1, 3, 5, 7). (A) The signal sequence, β-barrel and periplasmic domain are indicated by the gray, white and black boxes, respectively. The star (☆) indicates a unique C-terminal cysteine residue that is labeled with maleimide biotin. (B) 5 μg purified proOmpA-P1, P2, P4, P6 and P8 was separated by 10% SDS-PAGE and stained with Coomassie brilliant blue. Positions of molecular mass markers (in kDa) are indicated. Images adapted from Tomkiewicz, Nouwen, van Leeuwen, Tans, and Driessen [29]

genes encoding corresponding proteins were cloned (BamHI, HindIII) into expression vector pJF118, giving plasmids pEK204, pEK211, pEK212, pEK213, and pEK214, respectively.

Preproteins proOmpA and proOmpA-P8 derivative (plasmids pEK204 and pEK214, respectively) were overproduced at 30°C in strain MM52 (F^-, Δ*lacU*169, *araD*139, *rpsL*, *thi*, *relA*, *ptsF*25, *deoC*1, *secA*51) [33]. After harvesting the cells, inclusion bodies were purified and labeled with biotin- (Molecular Probes) or fluorescein-maleimide (Invitrogen) as described [34].

SecA [35] and His-tagged SecB [36] were purified as described previously.

DNA linker An 800 nm DNA linker with covalently bound digoxigenin and biotin groups was made by twice performing a restriction reaction on plasmid pUC19 and filling the resulting cohesive ends with digoxigenin-dUTP and biotin-dUTP, respectively, using the large (Klenow) fragment of DNA polymerase I (exo$^-$ mutant; New England Biolabs).

2.2.2 Bulk assays

***In vitro* translocation protection assay** The *in vitro* translocation assay, or protein protection assay [37] is a widely used protocol to measure protein translocation activity. Our proposed experimental configuration is derived from this solid experimental tool. It exploits the fact that the SecYEG translocase is localized on the outside (cytoplasmic) side of the IMVs. Preproteins translocated into the vesicle are then protected from proteinase K, which digests all untranslocated material outside of the vesicle. Non-digested, and therefore translocated, material is precipitated with trichloroacetic acid (TCA) and analyzed by SDS-PAGE.

In a protein protection assay, translocation reactions were performed in translocation buffer (50 mM HEPES-KOH, pH 7.5, 5 mM $MgCl_2$, 50 mM KCl, 2 mM dithiothreitol [DTT], 0.1 mg/ml bovine serum albumin [BSA]) with 50 µg/ml SecB, 10 µg/ml SecA, 80 nM of the urea-denatured labeled preprotein (proOmpA-P1 or proOmpA-P8) and 10 g of the IMVs containing high levels of SecYEG (derived from *E. coli* SF100). Reactions were started by the addition of 1 mM ATP and followed by incubation for 30 min. at 37°C. Reactions were stopped by chilling on ice. Non-translocated material was degraded by proteinase K treatment [21] whereafter the translocated material was precipitated by 8% TCA. Proteins from the supernatant were precipitated overnight at 4°C with 8% TCA. Analysis by 10% SDS-PAGE was followed by direct in-gel visualization using a Roche Lumi Imager F1 (Roche Molecular Biochemicals) [34] or chemiluminescence with anti-proOmpA antibody or streptavidin-alkaline phosphatase (Roche) in the case of fluorescein labeled and biotinylated preprotein, respectively.

Creation of translocation intermediates using streptavidin To create translocation intermediates, proOmpA-P8 with a biotin at the C terminus was incubated with an excess of streptavidin (Molecular Probes, 60× molar excess) in translocation buffer with 50 µg/ml of SecB for 5–10 minutes at room temperature. Next, 10 µg/ml SecA, 10 µg IMVs and 1 mM ATP were added and incubated for 30 minutes at 37°C. The translocation reaction was stopped by chilling on ice for 5 min. To separate untranslocated material and excess streptavidin from the IMVs, the vesicles were spun down on a sucrose cushion (50 mM HEPES-KOH, pH 7.6, 50 mM KCl, 5 mM $MgCl_2$ and 0.2 M sucrose) in an Airfuge ultracentrifuge (Beckman) for 30 min. at 30 PSI.

To check whether translocation was halted by the C-terminally bound streptavidin, a second round of translocation was performed: the obtained pellet was resuspended in translocation buffer with additional 10 µg/ml SecA, 50 µg/ml SecB and 80 nM of fluorescently labeled proOmpA-P8. After the addition of 1 mM ATP, translocation continued for 30 min. at 37°C. Non-translocated material was degraded by proteinase K and the residual protein was analyzed as described above.

2.2.3 Microsphere preparation

IMV microspheres For the optical tweezers protein translocation assay using a micropipette, IMVs were bound to amino-polystyrene microspheres. 15 µl of a 5% suspension of 1.88 µm amino-polystyrene microspheres (Spherotech) was washed twice by adding 500 µl of 50 mM HEPES-KOH, pH 7.9 (buffer A) and a subsequent 5 minute spin in a table centrifuge at full speed. The microspheres were resuspended in 200 µl of buffer A.

Next, 40 µl of IMV suspension (equivalent to 17.7 mg/ml membrane protein) was diluted in buffer A to a total volume of 250 µl. Then the IMVs were made monodisperse by passing the suspension 11× through a polycarbonate membrane with 100 nm pores using a LiposoFast extruder (Avestin).

Next, the washed microspheres were coated with the IMVs by adding 100 µl of the 100 nm IMV suspension and incubating overnight at 4°C in a hand-over-hand mixer. The microspheres were spun down and pre-blocked twice with 500 µl of buffer A with 10 mg/ml BSA for 30 min. at 4°C in a hand-over-hand mixer. The microspheres were again spun down and resuspended in 60 µl of buffer A with 0.1 mg/ml of BSA.

The microsphere-bound IMVs could be used to make translocation intermediates, as described above. Separation of untranslocated material and excess streptavidin from the microspheres can be done here using a table centrifuge at full speed instead of using a sucrose cushion.

Passive adsorption to polystyrene microspheres was detected using a fluorescence microscope by incorporating rhodamine-B-chloride in IMVs.

To analyze the translocation activity of IMVs connected to the polystyrene microspheres, the *in vitro* protection assay could be performed as described above, with the IMVs bound to the microspheres. After proteinase K digestion, the reaction mixture was treated with 10 mM PMSF and 1% SDS (spin 5 minutes, 13,000 rpm) in order to separate the protein from the microspheres.

Additionally, the ATP consumption during translocation of microsphere-bound IMVs could be determined by spinning down IMV microspheres after a translocation reaction and measuring the amount of released free phosphate in the supernatant using the malachite green assay [38].

DNA microspheres For our experiments, the 800 nm DNA linker molecules were coupled to polystyrene microspheres. Anti-digoxigenin (anti-DIG) antibodies (Roche Diagnostics) were covalently coupled to carboxyl-functionalized 1.87 µm polystyrene microspheres (Spherotech) using the crosslinker carbodiimide. A commercially available kit including all needed buffers was used for this crosslinking reaction (Polysciences, cat. no 19539-1). In this protocol, 100 µg of antibody was coupled to 250 µl 5% w/v microsphere suspension. The anti-DIG microsphere suspension was mixed with buffer containing DNA linker molecules and incubated for 30 minutes at room temperature in a hand-over-hand mixer.

2.2.4 Optical trapping procedures

Optical tweezers setup In our study, we used the optical tweezers setup that was presented in Chapter 1. The experiments using the surface configuration that was initially explored were performed using the diode laser (wave length 830 nm) as a trapping laser. Experiments were done in the z direction (in the axial direction of the laser beam, perpendicular to the coverslip). Using the linear relation between force F_z and the summed voltage V_{sum} of all four quadrants of the quadrant photodiode (QPD) [39], the force on a trapped microsphere in the z direction can be measured.

For the micropipette experiments presented in this chapter, the stronger Nd:YVO_4 laser (wave length 1064 nm) was used. Here, measurements were done in the x direction (horizontally, perpendicular to the laser beam). By fitting a Lorentzian to the power spectral density (PSD) of the movements of a trapped microsphere (see Chapter 1), the force constant of the optical tweezers and the sensitivity of the QPD were determined every day before doing experiments. On average, the force constant for a 1.88 µm polystyrene microsphere along the x coordinate was 237.4 pN/µm with standard deviation 18.6 pN/µm. The sensitivity of the QPD was on average ~1.63 V/µm with standard deviation 0.18 V/µm.

During the experiments, microsphere movements were measured by recording the normalized QPD V_x and V_y voltage and sum voltage V_{sum} at a frequency of 50 Hz. The analog electronics anti-aliasing filter was set at a filter frequency of 20 Hz. Additionally, the Labview particle tracking algorithm was used to track microspheres at a lower frequency (~5 Hz). For the analysis and for plots, the QPD data was used. The particle tracking data was only used for calibration.

Optical tweezers experiments using the cover slide surface A flow cell with 10 µl volume was created by drawing two parallel lines of vacuum grease (Hivac-G, Shin-Etsu) approximately 5 mm apart on a microscope slide (Menzel Gläser), in the lateral direction and by mounting a glass cover slide (24 mm×24 mm, Menzel Gläser) on top, under a 45° angle. Cover slides were previously silanized using 3-aminopropyltriethoxysilane (APES, Sigma-Aldrich), yielding a positively charged surface.

Next, 50 mM HEPES-KOH, pH 7.6, 100 mM KCl, 5 mM $MgCl_2$ 0.1% w/v BSA (HMS/0.1% BSA) containing the intermediate IMVs that were described above was flown in and incubated for 5 min. After removing unbound IMVs in 2–3 consecutive washes with HMS/0.1% BSA, biotin microspheres (Spherotech) and 1 mM ATP, diluted in HMS/0.1% BSA, were flown in. The flow cell was sealed with nail polish (Etos) and transferred to the optical tweezers setup.

Optical tweezers experiments using a micropipette A three-input/one-output flow cell as described in §1.4 was used for these experiment. The syringes connected to the outermost channels were filled with IMV- and DNA-microsphere suspensions. The syringe connected to the middle channel was filled with 50 mM HEPES-KOH, pH 7.6, 100 mM KCl, 5 mM $MgCl_2$, supplemented with 0.1% w/v BSA. To this buffer, 1 mM ATP and 10× diluted cell lysate from a SecA-overproducing strain of *E. coli* could be added to drive translocation. The flow system pressures were adjusted such that three separate flows could be distinguished next to each other. Before an experiment, the flow cell was moved using manually controlled stages such that the optical trap was located in the IMV microsphere flow. A microsphere was trapped and transferred to the micropipette tip in the middle of the flow cell. Next, a DNA microsphere could be trapped and transferred to the middle of the flow cell. There, an experiment could be started by moving the two microspheres together to try and create a connection between the biotin at the free end of the DNA linker and the streptavidin at the C terminus of proOmpA-P8.

2.3 Results

This section will describe the results of the experiments we performed towards single-molecule measurements on protein translocation. First, we will show the results of a derivative bulk study that used the protein construct that was developed for the optical trapping experiments. Next, we will show the results of optical trapping studies. First, we explored an experimental configuration without a DNA linker, with IMVs bound to the glass surface. Next, we performed experiments using the micropipette configuration that was already introduced in the introduction of this chapter. At the end of this chapter, we will perform some calculations on the force response of our trapping configuration to a hypothetical translocation step.

2.3.1 Bulk studies on the preprotein length dependence of protein translocation

The preprotein construct that was developed for our experiments, proOmpA-P8, was used in a study to address how the length of a preprotein substrate affects the translocation process. In this published study [29], translocation protection assays were performed with both proOmpA and proOmpA-P8 (and other proOmpA derivatives proOmpA-P2/P4/P6) as described before. TCA-precipitates were gathered at different time points to be able to follow translocation in time. Figure 2.6a shows a gel with the results of translocation. In Figure 2.6b, the intensity of the bands in Figure 2.6a are plotted as a function of time. In Figure 2.6a and b, it can be seen that translocation can only be detected after a short delay (from ~30 s for proOmpA to ~2 minutes for proOmpA-P8). This is because the proOmpA derivatives are labeled at the extreme C terminus, so translocation can only be detected after a preprotein has been fully translocated. Indeed, it can be seen that the delay for proOmpA-P8/P6/P4/P2 is bigger than that of the shorter proOmpA. Next, the translocation rate in picomoles of protein per minute was determined using the first, linear part of the curves in Figure 2.6b. The result is shown in Figure 2.6c. In this graph, it can be seen that the translocation rate of proOmpA is fourfold that of proOmpA-P8. Taking into account that proOmpA-P8 is four times longer than proOmpA (1397 vs 347 amino acids) one can conclude that the translocation rate expressed in amino acids per minute is equal for both proteins. The translocation experiments using proOmpA the derivatives with 2, 4 and 6 copies of the periplasmic domain confirmed this notion.

These data indicate that ATPase SecA drives a constant rate of preprotein translocation that is consistent with the stepwise model of protein translocation.

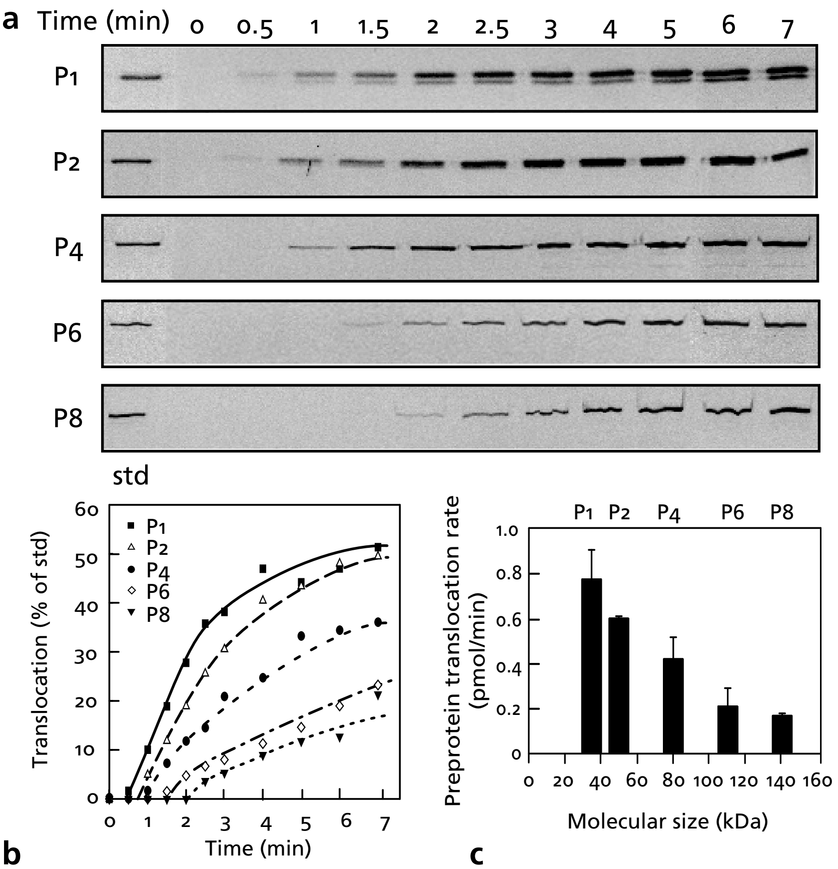

Figure 2.6: Preprotein length dependence of protein translocation. A protein translocation protection assay was performed with proOmpA (P1) and derivatives proOmpA-P2/P4/P6/P8. (a) TCA precipitates were gathered at different times and collected on an SDS-PAGE gel. The P1 gel shows bands for both the mature and the precursor form of OmpA. (b) The intensities of the bands were determined and plotted as a function of time. All curves show an initial delay, a linear phase and an eventual decrease of the translocation rate. (c) The translocation rate (in picomoles of protein per minute) was calculated from the linear phase of protein translocation. This data was published in Tomkiewicz et al. [29].

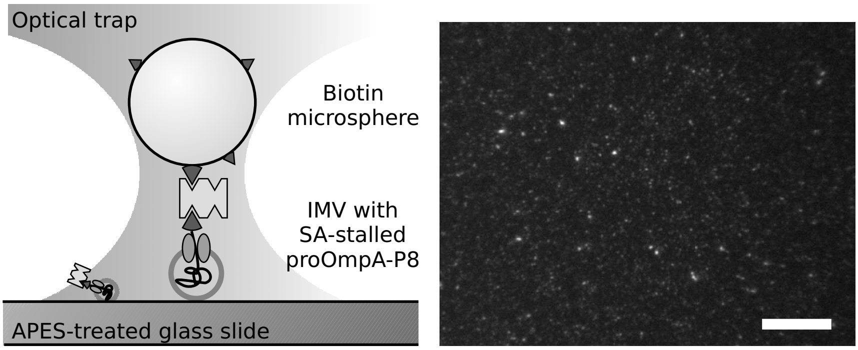

(a) (b)

Figure 2.7: Surface approach of single-molecule translocation experiments. (a) Schematic view of the experiment. Biotinylated proteins were translocated up to a streptavidin 'plug' that was previously bound to the biotin at the C terminus. The (negatively charged) IMVs were then bound to an APES-treated (positively charged) glass surface. Biotinylated microspheres were then bound to the streptavidin. Experiments were done along the axis of the trapping laser. (b) Fluorescence micrograph showing *E. coli* inner membrane vesicles of ~100 nm size on an APES-treated glass surface. Vesicles were made fluorescent by adding low amounts of a membrane-inserting fluorescent dye (C8-BODIPY 500/510-C5 [Molecular Probes]). The scale bar corresponds to 10 μm.

2.3.2 Optical tweezers experiments: surface approach

In our experiments towards single-molecule measurements on protein translocation, we initially explored a surface assay, with IMVs directly bound to the glass cover slide and the trapped microsphere acting as a force probe directly bound to the translocated protein. In Figure 2.7a, a schematic representation of this single-microsphere surface configuration is shown. All components of the shown construct are along the laser beam axis.

In this configuration, experiments were done on a surface that had been treated with APES. This silane forms a covalent bond with the glass, leaving a positively charged amine moiety at the interface with the water. The inner leaflet of the *E. coli* inner membrane carries a net negative charge. Hence, the inside-out IMVs will bind to the APES-treated cover slide through electrostatic interactions. Figure 2.7b shows that IMVs can bind efficiently to the APES-treated glass surface and hence that electrostatic interactions are an effective means to bind IMVs to a surface.

For our experiments, a novel method of creating a translocation intermediate was employed. In this method, a preprotein was kept in a partially translocated state with the C terminus exposed to the outside of a vesicle. To achieve this, proOmpA-P8 was biotinylated at the unique C-terminal cysteine and mixed with an excess of streptavidin (SA) in the presence of SecB. Under these conditions a preprotein-streptavidin complex is formed (proOmpA-P8-SA). Because streptavi-

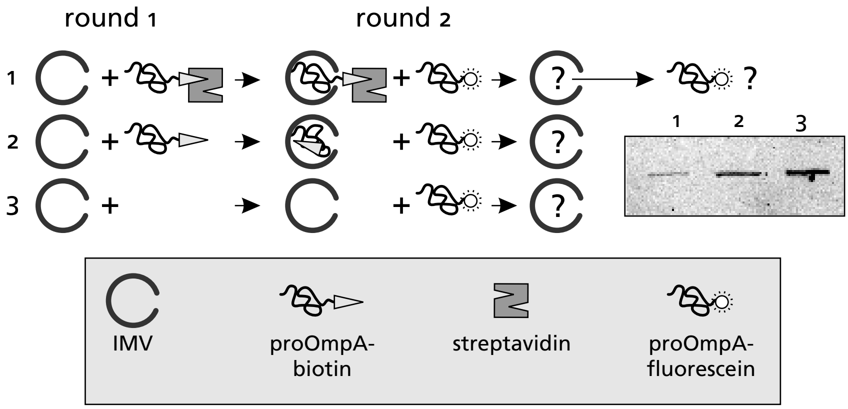

Figure 2.8: A translocation intermediate can be created by binding a streptavidin tetramer to the a biotin at the C terminus of a preprotein. A translocation reaction was performed with (1) proOmpA with a streptavidin bound to its C terminus, (2) proOmpA without bound streptavidin and (3) nothing. After removal of untranslocated preproteins (see §2.2), a second round of translocation was started with a fluorescent proOmpA construct. The contents of the IMVs were put on gel. This gel (right) shows that the translocation efficiency is significantly decreased for lane 1, showing that the translocases can be efficiently jammed using streptavidin.

din is a large molecule that forms a very stable tetramer it can block the translocation reaction. Indeed, it could be shown that the translocation of proOmpA-P8-SA is jammed on streptavidin: the SecYEG translocase was less active in a second round of translocation with the fluorescent labeled preprotein. Figure 2.8 shows the results of this test.

IMVs with translocation intermediates were bound to the surface and subsequently, biotin-polystyrene microspheres were flown in and left to bind to the exposed streptavidin tetramers on the IMV-surface. When observing the microspheres at the cover slide surface, a fraction of the microspheres would show a wiggling motion around a central position. Presumably, these microspheres were tethered to the glass surface via one or several IMVs.

An experiment was started by optically trapping a tethered microsphere and moving it away from the surface by moving the piezo stage in the z direction, along the laser axis. This way, we aimed to partially pull the translocated protein back out of the vesicle. Possibly, translocation would then translocate it back in the IMV because of the ATP in the surrounding buffer. The trapped microsphere would then move back to the surface and as a result, the QPD sum voltage V_{sum} (the summed voltages of all four quadrants) would change. This voltage is linearly related to the position z of the trap microsphere, so by measuring V_{sum}, translocation can be followed as a function of time. Alternatively, a constant force measurement can be done by performing force-feedback.

Several problems were encountered with the configuration that is sketched here: (i) In the axial direction, the optical tweezers have a lower trap stiffness than in the direction perpendicular to the optical axis so lower forces can be exerted on the trapped microsphere. (ii) Control experiments where no streptavidin was bound to proOmpA-P8 also showed tethered motion of microspheres, pointing to non-specific interactions between the polystyrene microspheres and the glass surface or IMVs. Because of these problems, the micropipette approach that will be described in the next section, was developed eventually.

What these experiments did show was that IMVs can be bound to a surface and that the bond to the surface was rather strong. Using the optical tweezers in the axial direction, a tethered microsphere could not be pulled off the glass surface. Moreover, the experiments showed that sizing the vesicles down to ~100 nm using an extruder does indeed lower the mechanical compliance of the vesicles. In fact, no deformation of the vesicles could be observed (data not shown).

2.3.3 Optical tweezers experiments: micropipette approach

In our experiments, we eventually used the micropipette approach that is illustrated in Figure 2.9a–c. Central to this approach is a DNA linker that is used to increase the distance between the translocated preprotein and a trapped microsphere that is used as a force probe. As a substrate for the IMVs, amino-polystyrene microspheres were used that were held by a micropipette. The two microspheres can be moved with respect to each other using the piezo stage. In this approach, translocation intermediates were created by binding a streptavidin tetramer to the C terminus of the translocated preprotein, as described previously. As a preprotein, proOmpA-P8 was used.

This two-microsphere/DNA linker approach solves the problems of the surface approach. A disadvantage of the DNA linker is the extra compliance that is introduced in the construct. However, the elastic properties of DNA are well known (see Appendix A) and can easily be filtered out of the data.

In Figure 2.9, we present the concept behind the micropipette measurement approach we proposed for single-molecule experiments on protein translocation: (a) To create a connection between the DNA linker and a preprotein, we brought the microspheres in contact by moving the piezo stage. A connection is made upon binding of a biotin at the end of the DNA linker to the streptavidin tetramer. (b) After a connection has been made, the distance between the two microspheres is again increased. Concomitantly, the force exerted on the preprotein is increased, and possibly, it is partially pulled out. (c) If this is indeed the case, the SecA and the ATP in the surrounding buffer may restart translocation of the preprotein back into the IMV. Translocation of the preprotein can then be followed by monitoring the movements of the trapped microsphere using the quadrant photodiode. Note that obtaining a specific connection between the biotin at the DNA linker and the streptavidin tetramer at the preprotein C terminus is crucial. Later in this

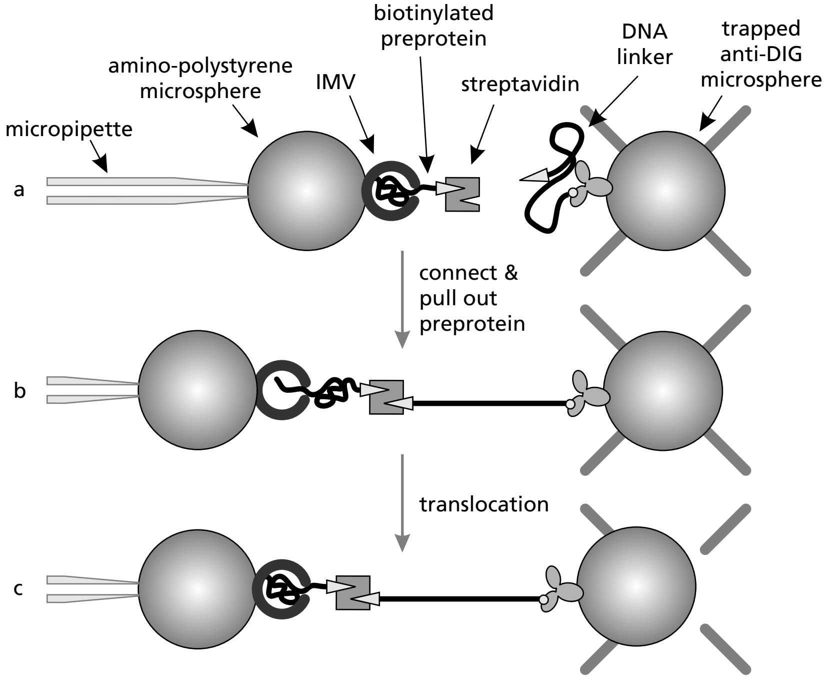
biotinylated preprotein
amino-polystyrene microsphere
IMV
streptavidin
DNA linker
trapped anti-DIG microsphere
micropipette
a
connect & pull out preprotein
b
translocation
c

Figure 2.9: The different steps in the micropipette approach that we employed to enable single-molecule protein translocation experiments. (a) an IMV microsphere is pushed against an optically trapped DNA microsphere to create a connection between the biotin at the end of the DNA linker and the streptavidin that was used to block translocation of the preprotein. (b) The distance between the microspheres is again increased and, possibly, the protein is partially pulled out. (c) Translocation of the preprotein will start because of the SecA and ATP in the surrounding buffer. Translocation of the preprotein will result in movement of the trap microsphere inside the optical trap.

section, we will present control experiments that we performed to test whether this connection could at all be made specifically.

The IMVs were bound to amino-polystyrene microspheres that carry a positive surface charge. Hence, the negatively charged IMVs will bind to the microspheres through electrostatic interactions. Figure 2.10 shows that fluorescent IMVs can indeed be bound specifically to polystyrene microspheres.

IMVs attached to microspheres were checked for translocation activity using the *in vitro* translocation protection assay that was introduced in §2.2.2. Figure 2.11 shows that both *in vitro* translocation and ATPase activity assays demonstrated that bound IMVs were still able to translocate the preprotein via the membrane, thereby hydrolyzing ATP.

Before a final translocation experiment could be performed, a number of tests

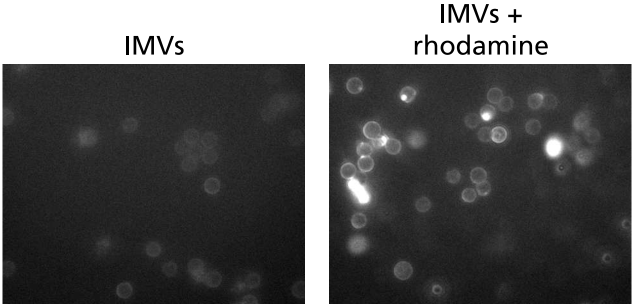

Figure 2.10: Binding of IMVs to amino-polystyrene microspheres. The right fluorescence micrograph shows how IMVs can cover the surface of amino-polystyrene microspheres through electrostatic interactions. The IMVs were made fluorescent using incorporated rhodamine-B-chloride.

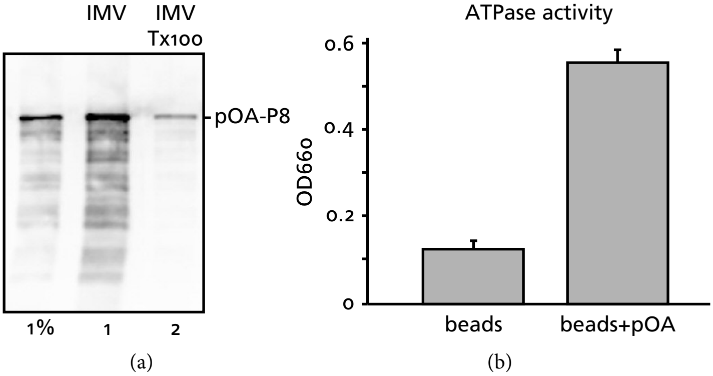

(a) (b)

Figure 2.11: Measurements showing translocation activity of microsphere-bound IMVs. (a) Results of protection assay, as described in §2.2.2. The translocation of microsphere-bound IMVs (lane 1) is compared to the translocation of microsphere-bound IMVs that were previously treated with detergent Triton X-100 to render the vesicles incapable of translocation (lane 2). 1% of the input material was loaded on gel as a reference (left) (b) A malachite green assay showed that adding proOmpA to microsphere-bound IMVs leads to increased ATPase activity, which is an indicator of protein translocation activity.

test #	IMVS	BIO	SA	ATP	Tethers
1:	+	+	+	+	+
2:	–	+	+	–	very few
3:	+	+	+	–	+
4:	+	–	+	+/–	+
5:	+	low +	–	+/–	–
6:	+	low +	low	+/–	+
7:	+	low +	medium	+/–	+
8:	+	+& –	+	+/–	+
9:	+	+	+	+/– low	+
10:	+	–	+	+/– low	+ (less)

Table 2.1: The results of the many control experiments done on the configuration shown in Figure 2.9. The labels illustrate the following: 'IMVS': whether (+) or not (–) the micropipette microsphere was coated with IMVS prior to the translocation reaction; 'BIO': whether or not the used proOmpA-P8 was biotinylated, 'low' indicates a reduced concentration of proOmpA-P8; 'SA': whether or not streptavidin (SA) was used to block translocation; 'low' and 'medium' represent a SA : proOmpA-P8-ratio of 3:1 and 15:1, respectively; 'ATP': whether or not ATP was added during the preparatory translocation reaction. For the tests of rows 9 and 10, a slightly altered protocol using translocation intermediates was used (see the text).

had to be done to check whether a specific connection could be made between the biotin at the free DNA end and the streptavidin at the C terminus of proOmpA-P8. The results of these tests are summarized in Table 2.1. This table shows, under a number of different conditions, the occurrence of DNA tethers after pushing together an IMV microsphere on the micropipette and a DNA microsphere in the optical trap. The experiments that are summarized in rows 1–8 were performed as described before (see also Figure 2.12a). For the experiments that are described in rows 9 and 10, a slightly altered approach was used (see Figure 2.12c) where the streptavidin tetramer was bound to the DNA linker rather than to the preprotein. In this case, translocation intermediates were created by using a low concentration of ATP in the preparation. The column labels in Table 2.1 represent the parameters that were changed between experiments.

Below, the results of each of the tests summarized in Table 2.1 are clarified.

Row 1 First of all, the experiment was prepared exactly as in the proposed experiment to check if a connection could at all be made between the DNA and the IMV microsphere. Indeed, pushing together an IMV microsphere and a DNA microsphere led to a DNA tether, that could be extended to overstretching (See Figure 2.13).

Row 2 To check whether the connection between the DNA and the IMV microsphere was via the IMVS and not via polystyrene-bound proOmpA-P8 or streptavidin (see Figure 2.12b, configuration 2a/2b), the micropipette mi-

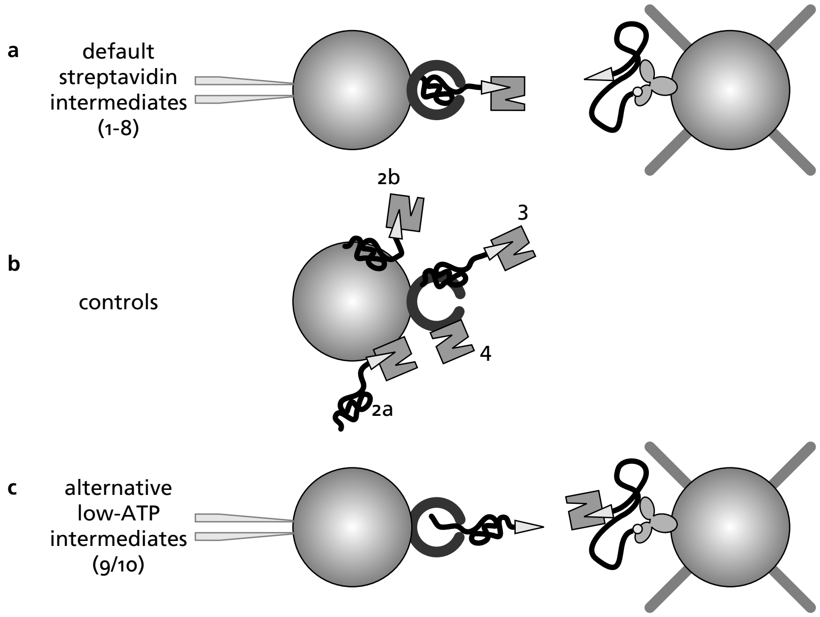
a
default streptavidin intermediates (1-8)
b
controls
2b
3
4
2a
c
alternative low-ATP intermediates (9/10)

Figure 2.12: Schematic illustration of the micropipette approach that was used in the tests described in this section. (a) default configuration with streptavidin-intermediates as described before. (b) Possible causes for non-specific tethers (c) Alternative configuration with a translocation intermediate created by performing a short preparatory translocation reaction at low ATP. The streptavidin is bound to the DNA linker rather than to the preprotein.

crospheres were prepared without adding IMVs (but with proOmpA-P8-SA). Here, only DNA tethers could be formed that were easily broken. Apparently, both the proOmpA-P8-BIO and the streptavidin do not bind to the polystyrene strong enough to create a strong tether.

Row 3 ATP was left out in the translocation reaction. In this case, proteins will not translocate and observed tethers can solely be explained from non-specific connections between either preprotein or streptavidin and the IMV membrane. Remarkably, also in this case, tethers were observed, likely due to direct binding of proOmpA-P8-BIO and/or streptavidin to the IMV membrane (see Figure 2.12b, configuration 3/4).

Row 4 This test was done to determine whether streptavidin shows affinity to the IMV surface. non-biotinylated proOmpA-P8, whether translocated (+ATP) or not (−ATP), cannot be bound by streptavidin. Nevertheless, tethers were observed, indicating that streptavidin can bind directly to the IMV membrane with high affinity (see Figure 2.12b, configuration 4). Possibly, the positive charge of streptavidin might be responsible for its binding to the

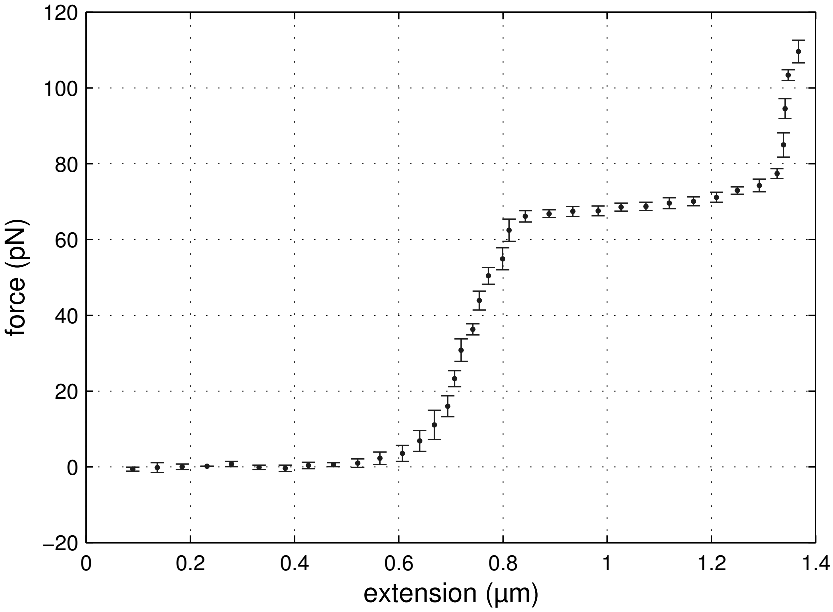

Figure 2.13: Overstretching of dsDNA. An 800 nm DNA linker was tethered between an anti-DIG microsphere and an IMV microsphere and extended to overstretching. Several consecutive force–extension curves were averaged to obtain this graph. It can clearly be seen that at a force of 65–70 pN, the DNA can be overstretched until ~170% of its contour length.

negatively charged membrane. Alternatively, it might bind to negatively charged, membrane-associated proteins.

Rows 5–7 The experiment summarized in row 4 showed that streptavidin binds to the IMVs. In the sample preparations, a large molar excess of streptavidin is used (60:1) in the binding to proOmpA-P8. Hence, more than 98% of the streptavidin tetramers stay unbound and can bind non-specifically to the membrane, where they can result in the unwanted tethers observed in the experiments of row 4. Rows 5–7 show the results of experiments with different molar ratios of SA : proOmpA-P8 (0:1, 3:1, 15:1). When no streptavidin is added (row 5), no tethers are observed. However, at only a small molar excess (row 6) of SA, non-specific tethers can be observed already if ATP is left out in the preparatory translocation reaction.

Row 8 proOmpA is a membrane protein and experiments have shown that it can associate with membranes and insert itself on a timescale of minutes [40]. Hence, part of the strong interaction between streptavidin and the IMVs can be via such membrane-associated, non-translocated, biotinylated proOmpA-P8 polypeptides (see Figure 2.12b, configuration 3). To prevent membrane association of biotinylated proOmpA-P8, IMVs were pre-incubated with non-biotinylated proOmpA-P8 prior to translocation of biotinylated proOmpA-P8. It was thought that this would block the membrane for biotinylated proOmpA-P8 with the aim to direct it to the translocase, where an intermediate could be formed. However, also here, strong tethers could be formed if no ATP was added.

Row 9–10 To reduce non-specific binding of the streptavidin to the membrane prior to the trapping experiment, the streptavidin tetramer that was needed to connect the DNA linker to the preprotein was now connected to the DNA, rather than to proOmpA-P8 (see Figure 2.12c). To keep the biotin at the C terminus of proOmpA-P8 exposed to the outside of the IMV, translocation was performed until a translocation intermediate state by lowering the ATP concentration 400-fold in the sample preparation from 2 mM to 5 µm and by lowering the time for the translocation reaction from 30 min. to 8 min. Moreover, IMVs were treated with urea prior to translocation to denature all membrane-associated, non-inserted proteins that could eventually be responsible for non-specific binding to streptavidin. To enable a translocation measurement in this configuration, a connection should be made between the DNA-bound streptavidin tetramer and the biotinylated preprotein in the absence of ATP in the flow cell. Once a specific connection is made, ATP-containing buffer could be flown in to restart translocation. We performed control experiments to investigate the presence of non-specific tethers in this approach (leaving out ATP from the preparatory translocation reaction; performing the experiment with non-biotinylated proOmpA-P8 [row 10]). The result in Table 2.1 indeed shows a small decrease in the amount of non-specific tethers observed if non-biotinylated proOmpA-P8 is used or if no ATP is added in the preparatory translocation reaction. However, because the translocation effects that we expect to see are very subtle, an even higher efficiency in acquiring specific tethers is required.

Because, in our configuration, we could not couple the DNA linker to a translocated preprotein with enough certainty, it was not possible as of yet to measure translocation with our optical tweezers setup. In the discussion at the end of this chapter, some possible solutions to the problems mentioned here will be given.

2.3.4 Calculation of step response

Preprotein translocation is proposed to occur in a stepwise fashion [21]. So far, measurements of such steps could not be accomplished, due to the experimental problems that were sketched in the previous chapter. Once the mentioned problems are solved, the question is what the minimum step size is that can be detected, using our optical tweezers setup in the micropipette configuration. To check this, calculations were performed of translocation measurements, performed with both micropipette and optical trap held at a constant position (constant-position mode),

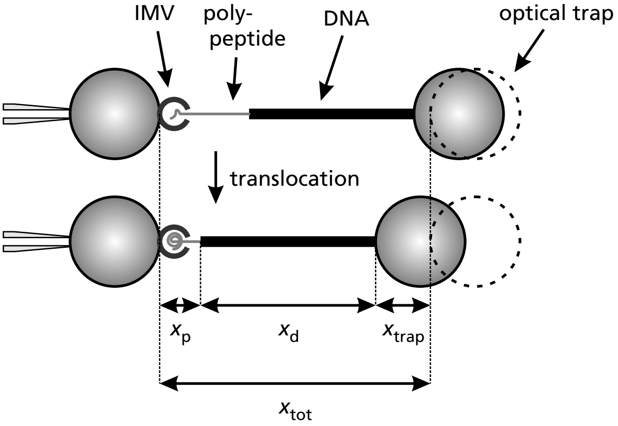

Figure 2.14: Schematic illustration of constant-position measurement of protein translocation. Indicated are DNA extension x_d, polypeptide extension x_p, microsphere-trap center distance x_{trap} and total extension x_{tot}.

as shown in Figure 2.14. This figure schematically illustrates how a polypeptide is being translocated inside an IMV. As a result, the optically trapped microsphere is pulled further away from the center of the focus and the force on the polypeptide/DNA construct increases. Now, also the DNA extension and the extension per amino acid of the polypeptide increase (while the total polypeptide extension increases). In this section, we will calculate the response of the trapped microsphere on translocation. Here, we assume that translocation occurs in a stepwise fashion.

For this calculation, we regard the coupled preprotein and DNA linker as two coupled WLC polymers. The DNA linker is modelled as an extensible WLC with persistence length $p_d = 53\,\text{nm}$, elastic stretch modulus $S_d = 1200\,\text{pN}$ and contour length $L_d = 800\,\text{nm}$. The translocated polypeptide is modeled as an inextensible WLC with persistence length $p_p = 1\,\text{nm}$ and a variable contour length L_p that decreases with translocation as $(N - n)l_{aa}$, with N the total number of amino acids of the polypeptide ($N = 1305$ for proOmpA-P8), n the number of amino acids that has been translocated already, and $l_{aa} = 0.33\,\text{nm}$ [9] the contour length per amino acid. Using the force extension relations (See Appendix A; subscripts p and d indicate the polypeptide and the DNA linker, respectively):

$$\frac{x_d}{L_d} = 1 - \frac{1}{2}\left(\frac{k_B T}{F(n)p_d}\right)^{1/2} + \frac{F(n)}{S_d}, \tag{2.1}$$

$$\frac{F(n)p_p}{k_B T} = \frac{1}{4}\left(1 - \frac{x_p}{(N-n)l_{aa}}\right)^{-2} - \frac{1}{4} + \frac{x_p}{(N-n)l_{aa}}, \tag{2.2}$$

$$F(n) = k_{trap} \cdot x_{trap}, \tag{2.3}$$

with trap stiffness $k_{trap} = 100\,\text{pN}/\mu\text{m}$, force $F(n)$ could be calculated for different

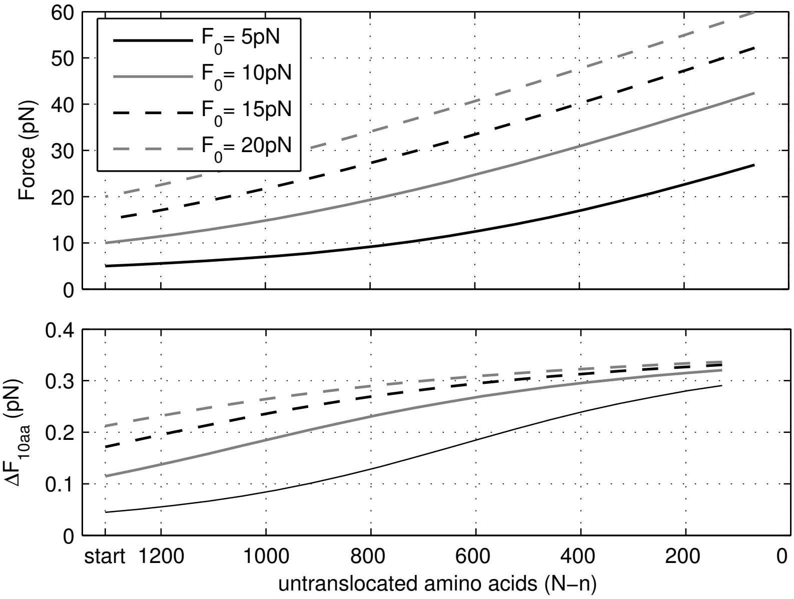

Figure 2.15: Calculated constant-position measurements of protein translocation. The top graph shows, for different values of initial force F_0, several examples of how the force changes with the shortening of a polypeptide due to translocation. The bottom graph shows, for each of the simulated measurements, the increase in force ΔF_{10aa} due to translocation of 10 amino acids.

trap microsphere-micropipette distances $x_{tot} = x_d + x_p + x_{trap}$ (see Figure 2.14).

The top graph of Figure 2.15 shows four examples of $F(n)$, for different values of F_0, the force initially exerted on the DNA-polypeptide construct at the onset of translocation. In the shown curves, translocation is assumed to start at the first amino acid of the signal sequence of proOmpA-P8. In this graph, it can be seen that if a tethered construct is held at a force of 5 pN at the beginning of translocation, the force will rise up to more than ~20 pN when the protein is fully translocated. In the bottom graph of Figure 2.15, the response in force on a hypothetical translocation step of 10 amino acids is shown. It can be seen that if the construct is held at 5 pN at the start of translocation, the response in force on a translocation step of 10 amino acids is ~0.05 pN.

This analysis shows that if the construct is held at a higher force during the measurement, the response in force on a translocation step is higher and, likewise, smaller translocation steps can be detected. Given the instrumental error of our setup, $\sigma_F = 0.11$ pN, the minimal detectable translocation step is around 0.11/0.05×10 = 22 amino acids if the construct is held at 5 pN at the start of translocation.

2.4 Discussion

In this chapter, we described the steps that we have taken to enable single-molecule experiments on protein translocation by the bacterial Sec translocase using optical tweezers. We proposed an experimental configuration with the canonical *in vitro* translocation activity assay, that uses *E. coli* inner membrane vesicles, at its core. To overcome the associated technical challenges, we introduced novelties such as a DNA linker, a proOmpA-derivative with its periplasmic domain repeated 8 times (proOmpA-P8), and streptavidin-jammed translocation intermediates.

In our experiments, we have seen that inner membrane vesicles (IMVs) can be attached to both a glass surface and polystyrene microspheres with enough strength, to hold the forces inherent in optical trapping experiments. Moreover, it was shown that by reducing the size of these IMVs to ~100 nm, no mechanical compliance of the phospholipid membrane could be observed that could obscure eventual single-molecule measurements.

Furthermore, a proOmpA derivative with 8 copies of its periplasmic domain was successfully constructed. This was done to increase the measurement time per preprotein, in eventual experiments. Indeed, we could show that the translocation rate of proOmpA-P8 (pmol/min) is lower than that of proOmpA. Moreover, it was found that the translocation time per amino acid is constant.

By binding a streptavidin tetramer to the C terminus of proOmpA-P8, using a covalently bound biotin, translocation could be efficiently halted before complete translocation of the preprotein. This principle was used in our proposed experiment to make a partially translocated preprotein accessible to optical trapping experiments. To connect an optically trapped microsphere to the preprotein, a biotinylated DNA construct was used to link the microsphere surface to a streptavidin tetramer at the IMV surface.

We performed a range of control experiments to check whether this connection between the DNA linker and the preprotein could indeed be made. In the protocol explored so far, aspecific connections could not be sufficiently reduced, preventing us from doing single-molecule experiments. In summary, the control experiments showed that currently, there are two major obstacles for single-molecule experiments on protein translocation using optical tweezers: (I) aspecific binding of proOmpA-P8 to the IMV membrane. (II) aspecific binding of streptavidin to IMVs. Because of these obstacles, we could not make a specific tether between a DNA linker and a preprotein in a translocation intermediate state with enough certainty.

The binding of proOmpA-P8 to the IMV membrane might be due to the fact that part of the sequence of proOmpA-P8 is a sequence of hydrophobic amino acids that fold into a β-barrel once in the outer membrane of *E. coli*. In our experiments we think that it is this hydrophobic domain that is mainly responsible for the observed aspecific interactions of proOmpA-P8 with the IMVs. There are different solutions to this problem that can be thought of. First of all, a mutant of proOmpA-P8 can be made that does not contain this hydrophobic, β-barrel domain. In fact, we have made one such mutant, but unfortunately, purification appeared to be not

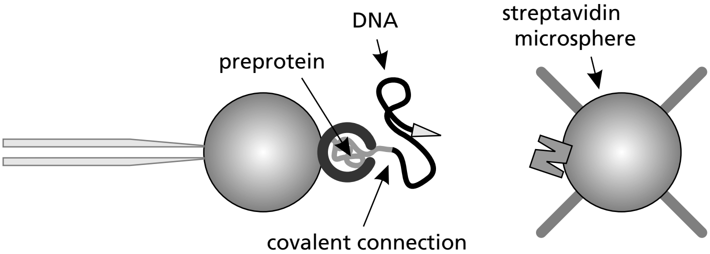

Figure 2.16: Trapping configuration with a covalent link between the translocated preprotein and a DNA linker.

possible.[1] Another solution might be to use other proteins than proOmpA-P8 for these experiments that have a less pronounced hydrophobic domain. Along these lines, one can think of, e. g., the maltose-binding protein (MBP) that will be introduced in the next chapter. An MBP construct with multiple repeats of MBP has been constructed for the protein unfolding experiments that will be described in the next chapter. This construct could also be useful for the protein translocation experiments.

The problem caused by the binding of streptavidin to the IMV membrane could be circumvented by covalently coupling the DNA linker to the preprotein instead of using biotin-streptavidin interactions (see Figure 2.16). In this method, the DNA linker is covalently linked to the C terminus of a preprotein. Conceptually, in a preparatory translocation step using microsphere-bound IMVs, the preprotein with covalently coupled DNA construct is translocated up to the covalent link. The DNA linker works here as a plug, similar to the streptavidin tetramer in previously described experiments. In the optical tweezers setup, a connection is made with streptavidin-coated microspheres and a trapping experiment can be started.

Crosslinking of proteins to dsDNA is possible [9] but very inefficient. In the crosslinking of proOmpA to DNA, however, the high concentration of urea that is added to prevent proOmpA from aggregation will render the used crosslinker nonfunctional. Here, a preprotein that is less prone to aggregation should be used. Experiments have been done with crosslinking dsDNA to the maltose-binding protein, but the crosslinking efficiency was so far insufficient.

Another complication with this covalent-linking approach, is that it is expected that the translocation efficiency of a preprotein construct will seriously be lowered by covalently coupling a DNA molecule to it. Most likely, the targeting of the signal sequence to the translocase will be hampered by the much larger attached DNA molecule (1365 kDa vs 140 kDa).

---

[1] In the cytosol, proOmpA-preproteins aggregate into inclusion bodies at limiting SecB concentrations. This aggregation is mediated by hydrophobic interactions between β-barrel domains. These inclusion bodies can easily be separated from cell lysate and are hence used to purify proOmpA and proOmpA derivatives such as proOmpA-P8. proOmpA without a β-barrel does not create inclusion bodies. At overexpression, it becomes toxic to the cell, which impedes bacterial growth and protein purification.

Another solution to the binding of streptavidin to the IMV membrane might be the use of NeutrAvidin [41] rather than streptavidin. NeutrAvidin is a commercially available form of avidin with a neutral pI to minimize nonspecific adsorption. In our experiments, it might have a reduced affinity to the IMV membrane.

There are many open questions concerning protein translocation that require single-molecule experiments. We have showed some steps towards such experiments and have done some recommendations to possibly overcome the issues that were pointed out in this chapter.

3

Unfolding the maltose-binding protein (MBP) with optical tweezers

We have used optical tweezers to study the folding and unfolding of a single protein, the maltose-binding protein. We will present measurements on the effect of chaperone protein SecB on the (un)folding and we will present molecular dynamics simulations to explain an observed unfolding intermediate.

3.1 Introduction

In *Escherichia coli*, many different proteins are constantly being synthesized by the ribosome. These proteins can be grouped in different classes by their destination: cytosolic proteins remain in the cytosol, membrane proteins should be targeted to either the inner or outer membrane, periplasmic proteins have to be transported to the periplasm, the space between inner and outer membrane, and finally secretory proteins have to be transferred to the outside of the cell.

It is evident that the folding properties of a protein are of importance for the targeting process. Cytosolic proteins have to fold quickly in order to be able to fulfill their task in the cytosol. In the crowded milieu of a cell, folding chaperones such as GroEL [42] and DnaK [43] are often needed for folding. Membrane proteins, periplasmic and secretory proteins, however, should be kept in an unfolded state, in order to pass the narrow pore of the SecYEG translocase (see Chapter 2) to reach their destination. Hence, folding prior to translocation has to be prevented. Another issue arises with the (inner and outer) membrane proteins. These proteins carry large stretches of hydrophobic residues in their sequence, that will eventually fold into transmembrane helices, once the polypeptide has reached its destination. In the cytosol, however, these hydrophobic stretches may cause proteins to aggregate into *inclusion bodies*, after which the protein cannot be translocated anymore.

In *E. coli*, the folding and aggregation of proteins prior to translocation is prevented by the chaperone protein SecB. During translation of a protein—whether cytosolic or not—SecB binds to certain hydrophobic parts of the newly synthesized polypeptide, preventing the polypeptide from finding its native conformation or from aggregation into inclusion bodies. Next, these non-cytosolic proteins carrying

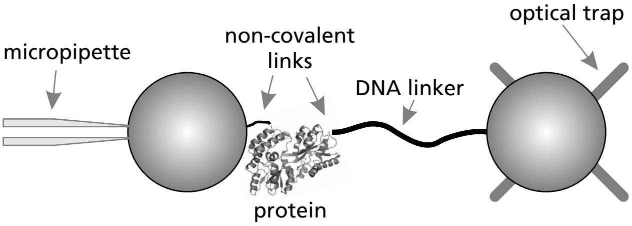

Figure 3.1: Schematic representation of the trapping geometry that was used in the optical tweezers experiments. Later in this chapter, the nature of the non-covalent links and the procedure to obtain this geometry will be further introduced.

a translocation signal sequence are targeted to the Sec translocase, while cytosolic proteins—without the signal sequence—are released to the cytosol, where they can fold. A more detailed explanation of the mechanism behind this selection will be given later in this chapter.

Previously, bulk assays have been performed to study the effect of SecB-binding to an unfolded polypeptide. Much has been revealed by these studies, but many questions remained unanswered, e. g., on the dynamics of the binding of SecB to a preprotein, and on the effect of SecB-binding to the configuration of an unfolded polypeptide. To answer these questions, we have—for the first time—studied the effect of SecB-binding on the folding and unfolding of a *single* protein, the maltose-binding protein or mbp.

To unfold (and refold) a protein, we used an optical tweezers setup employing the novel trapping construct that is shown in Figure 3.1. In this geometry, non-covalent links were used to link the C and N terminus of a protein to a polystyrene microsphere and a 920-nm dsdna linker that was introduced to prevent interactions between the optically trapped microsphere and the protein and to prevent interference of the micropipette microsphere with the trapping beam. This trapping geometry allowed for the repeated unfolding and refolding of a single protein in a controlled way. Moreover, our geometry was much more straightforward and gave a higher yield than a recent other solution [9].

The mbp-unfolding experiments showed that the forced unfolding of mbp often occurs via one or several unfolding intermediates. Repeatedly, we observed one specific unfolding intermediate after a first partial unfolding of mbp at a force of ~16 pN. Further unfolding of mbp to a fully extended polypeptide then occurred at a force of ~25 pN. Unfolding experiments using an engineered protein construct consisting of four in-tandem repeats of mbp confirmed these observations.

For a better interpretation of the observed unfolding intermediates in the forced unfolding of mbp, we undertook steered molecular dynamics (smd [44]) simulations. These simulations revealed a series of C-terminal surface-exposed α-helices in the structure of mbp that relatively easily detached from the mbp structure (when a force was exerted on C and N terminus in an smd simulation). This predicted intermediate agrees remarkably well with the experimentally observed one.

Next, we studied the effect of SecB on the unfolding and refolding of MBP by adding SecB during an optical tweezers unfolding experiment. We saw no effect of SecB binding prior to the complete unfolding of the tethered protein. This was the first direct observation showing that SecB has no affinity to native, stably folded proteins. After the forced unfolding of MBP, we observed that the refolding of the unfolded polypeptide was dramatically prevented by the presence of 0.1 μM of SecB, in an all-or-nothing manner. No single feature pointing at (partial) refolding could be observed. We will discuss the implications of this observation on the SecB-preprotein binding mechanism. Extending an unfolded polypeptide in a SecB-bound state resembled worm-like chain behavior. We will show that this suggests that in SecB-mediated protein translocation by the Sec translocase, only a fraction of the free energy from ATP hydrolysis by SecA is used for the unfolding of a protein.

We start by further introducing chaperone SecB and the protein used in our experiments and simulations, MBP. Then, we will further describe the materials and methods used in our experiments. Next, we will present the results from our experiments and simulations. We will finish this chapter by discussing the implications of our results to protein folding, the binding of SecB to a substrate protein, and to protein translocation in general.

3.1.1 The role of SecB in the targeting of proteins

Figure 3.2 shows, in a schematic way, the role of SecB in the transport of a cytosolic (1) and a periplasmic (2) protein to their respective destination. In the transport pathway of a periplasmic protein (Figure 3.2-2), SecB interacts with a newly synthesized polypeptide during translation. The concentration of SecB in the cytosol is high (~13 μM tetramer [45]) so all periplasmic preproteins will be bound during translation. SecB has no interaction with the protein translocation signal sequence, but binds to peptides in the mature part of the preprotein [46]. Binding of SecB to a polypeptide prevents it from aggregation or folding prior to translocation to the periplasm. The SecB-bound state of a preprotein is termed *translocation-competent* state. Note that after synthesis of a new protein, there is a competition between folding of the protein and its binding to SecB. This competition is governed by *kinetic partitioning*. Later in this chapter, we will give a more detailed example of this kinetic partitioning.

After binding of a preprotein to SecB, the preprotein-SecB complex diffuses to the translocase at the inner membrane. There, SecB binds to ATPase SecA with high affinity [47]. Next, also the preprotein signal sequence binds to SecA, tightening the bond between SecA and SecB. Now, the preprotein is released from SecB and delivered to SecA [48]. Upon hydrolysis of ATP by SecA, SecB is released. Next, by repeated ATP hydrolysis of SecA, the preprotein polypeptide is translocated

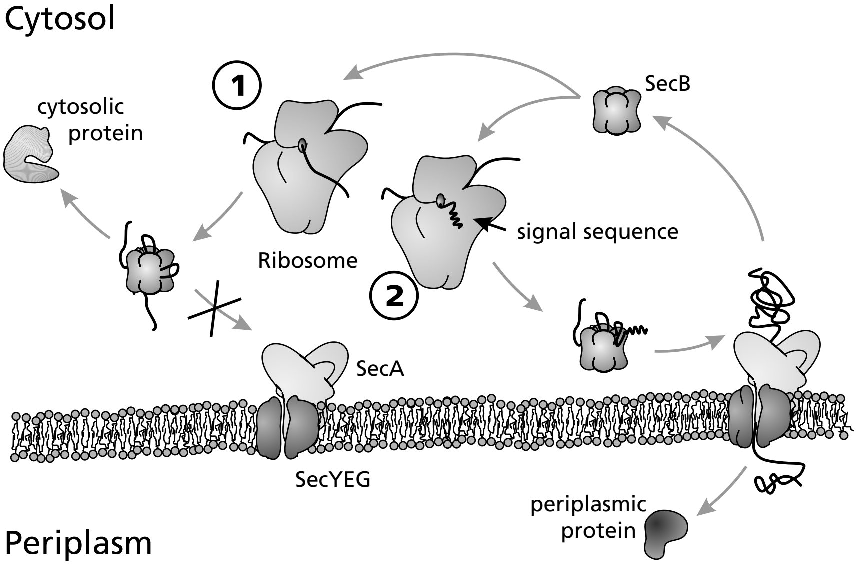

Figure 3.2: Protein translocation through the *E. coli* inner membrane shown in a step-by-step manner. The role of SecB is specifically shown.

through the membrane and will fold into its native state in the periplasm. For a review on protein translocation by the Sec translocase, see Driessen et al. [23]

Since the occurrence of high-affinity SecB-binding peptides is the same in both cytosolic and secretory proteins [46], also cytosolic proteins will associate with SecB during translation (Figure 3.2-1) and will subsequently be delivered to the translocase on the inner membrane. The absence of a signal sequence, however, will prevent the preprotein from binding to SecA and translocation cannot start [49]. Eventually, the protein will be released by SecB to the cytoplasm where it can fold into its native state, possibly aided by folding chaperones such as GroEL [42].

3.1.2 Structure of SecB

In Figure 3.3, different representations of the structure of SecB are shown [26]. SecB is a homotetrameric protein with a molecular mass of ~17 kDa that can be regarded as a dimer of dimers. The cartoon representation of Figure 3.3a shows a view on one of the two sides carrying the proposed SecA-binding site [26]. Figure 3.3b shows how channels are located between two monomers. These 70 Å-long channels likely form the peptide binding sites of SecB.

Knoblauch et al. [46] screened 2688 peptides covering sequences of 23 proteins for their SecB binding. This helped defining a binding motif in peptides that bind to SecB. A typical SecB-binding peptide consists of ~9 residues and is enriched in

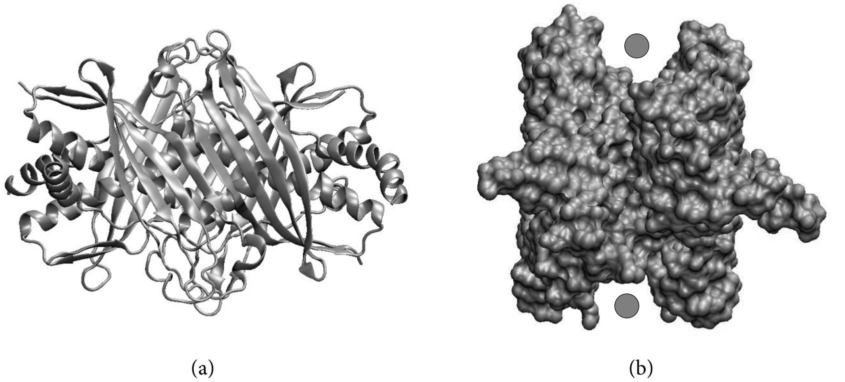

Figure 3.3: Different representations of the structure of the SecB tetramer (PDB-ID: 1FX3 [26]). (a) Cartoon drawing of the top view of SecB showing the β-sheet that is formed by two monomers. This surface contains the SecA-binding site. (b) Surface drawing showing the previous view rotated over 90° around a vertical axis, with the two binding channels indicated. Figures were prepared using VMD [50].

aromatic and basic residues. Acidic residues are disfavored by SecB. In binding of peptides to SecB, hydrophobic interactions contribute most to the binding free energy [51].

3.1.3 The maltose-binding protein (MBP)

In the protein unfolding experiments described in this chapter, the maltose-binding protein (MBP) of *E. coli* was used. MBP is a periplasmic protein that is part of the *E. coli* maltodextrin transport system [52], which belongs to the superfamily of the evolutionarily conserved ABC transport systems [53]. MBP transfers maltooligosaccharides such as maltose from a receptor at the outer membrane to a receptor at the inner membrane, where the maltooligosaccharides are transported to the cytoplasm by ATP-hydrolysis.

MBP is a 370-aa, 40.6 kDa protein containing a maltose binding cleft, surrounded by two globular domains, or lobes. Figure 3.4 shows the crystal structure of MBP [54]. This picture clearly shows that MBP is a bilobate protein. The maltose-binding cleft located in the middle is indicated. The contour length of a fully extended MBP polypeptide chain (i. e., with the secondary structure removed) would amount to 120 nm.

MBP is synthesized in the cytosol as a preprotein (preMBP) carrying a 26-aa signal sequence at the N terminus. MBP has been used as a model protein for bulk protein folding experiments [56, 57, 58], for determining the effect of a signal sequence on the folding of a preprotein [59, 60] and for studying SecB–protein interaction [51, 61, 62, 63, 64, 65]. The pool of knowledge gained from these studies

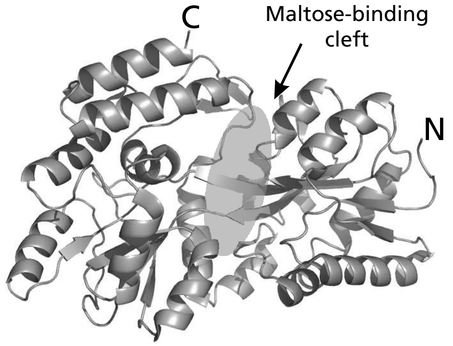

Figure 3.4: Crystal structure of the maltose-binding protein (mbp, pdb-id: 1jw4 [54]) with the maltose-binding cleft indicated and the C and N termini. Figure was prepared using Pymol [55].

rendered mbp an ideal protein for our single-molecule optical tweezers study. Titration calorimetry experiments [51] showed that the free energy of stability (ΔG) of the complexes between SecB and both mbp and premBP amounts to ~42 kJ/mol or ~17 $k_B T$ at room temperature, equivalent to a dissociation constant K_d of 30 nM for mbp (at 6.5°C) and 27 nM for premBP at (7.7°C). Moreover, these experiments showed that mbp binds to the SecB tetramer in a 1:1 stoichiometry (i. e, 1 mbp protein binds to 1 SecB tetramer). The unfolding free energy (ΔG) of mbp (at 298 K) was determined by Beena et al. [60] to be 37.2 kJ/mol (15.0 $k_B T$) for mbp and 30.5 kJ/mol (12.3 $k_B T$) for premBP.

After synthesis of a new mbp precursor, note that there is competition between binding to SecB and folding to the native state. This competition is most likely governed by the rates of folding (in s^{-1}) and the rate of SecB-binding (in $M^{-1} s^{-1}$) and -unbinding (in s^{-1}) of the preprotein. It has been proposed that there is a *kinetic partitioning* [66] in this competition. One can calculate that it cannot be thermodynamically determined, i. e., by free energy differences between the different states (bound/unbound; folded/unfolded). Thermodynamics dictates that a SecB concentration as high as 4 mM is required at 37°C to have an equilibrium concentration of folded premBP equal to the concentration of preprotein/SecB complexes, assuming that no new preproteins are synthesized or translocated to the periplasm. In *E. coli*, the concentration of SecB is more than three orders of magnitude lower than that (~13 μM tetramer [45]) so in the presence of SecB, all mbp precursors would irreversibly fold to their native state and hence cannot be translocated to the periplasm. For the rate of folding of premBP, a value of 0.25 s^{-1} at 30°C has been estimated [67]. This value is considerably smaller than the proposed binding rate of SecB, 130 s^{-1} [66], assuming that 10% of the 13 μM of SecB is available for binding. Hence, folding is a much slower process than SecB-binding. SecB tetramers will bind to a polypeptide during its folding, thereby preventing complete folding to the native state before reaching the translocase. Cytosolic proteins have a

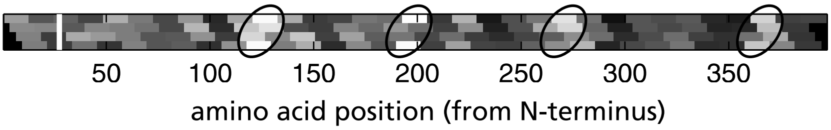

Figure 3.5: Linear representation of the sequence of preMBP, showing the relative affinity of 13 aa peptides to SecB. Data adapted from Knoblauch et al. [46, fig. 2]. Each gray rectangle represents a 13 aa peptide from MBP. Left of the white line at amino acid position 26, the translocation signal sequence is shown. Four regions with high affinity to SecB are indicated at amino acid position 120, 190, 270 and 360.

higher folding rate (5–10 s^{-1}) and, moreover, are not translocated to the periplasm, hence these proteins are likely to eventually unbind from SecB (unbinding rate ~3 s^{-1}) and fold to the native state where they cannot bind to SecB anymore.

Figure 3.5 shows a linear representation of the sequence of MBP with the relative affinity of 13-aa peptides within MBP to SecB. This data was determined by peptide screening analysis, performed by Knoblauch et al. [46]. It can be seen that, as mentioned before, the signal sequence has a low affinity to SecB. Along the sequence of MBP, four regions can be distinguished (indicated with ovals) with a high occurrence of peptides with a high relative binding affinity to SecB.

3.2 Materials and methods

3.2.1 Experimental configuration

We have used an optical tweezers setup to study the unfolding and refolding of single proteins. In the single-molecule protein unfolding field, most studies employ atomic force microscopy (AFM). In AFM studies, connections between the protein and surfaces are made through non-specific interactions. Compared to an approach using AFM, optical tweezers allow for a more specific tethering of C and N terminus of the protein. Because of the lower spring constant of the optical trap, lower unfolding forces can be detected and lower pulling rates can be reached. This way, we could refold a protein in a controlled way, after first unfolding it.

In single-molecule protein unfolding studies, surface interactions have to be minimized. During unfolding, hydrophobic parts of the polypeptide chain become exposed that might interact with the nearby surface. To avoid this problem, in AFM unfolding studies, the protein of interest is often cloned between several copies of titin immunoglobulin domains [68, 69] or a construct with multiple in-tandem repeats of the protein is used [70, 71] to increase the distance of proteins to a surface during an unfolding measurement. In an optical tweezers study done by Cecconi et al. [9], the C and N terminus of the protein of interest (ribonuclease H) were covalently linked to two 500-bp DNA spacers to prevent interaction of the protein with the surface of one of the two polystyrene microspheres that were used to exert force on the construct. In our optical tweezers experiments, we used a novel approach using a single DNA linker and non-covalent links between the protein and a microsphere and the DNA linker, respectively. Compared to the covalent links that Cecconi et al. used, this approach allows for connections that are easy to make yet are strong enough to sustain the forces needed to unfold a protein. The streptavidin-biotin connections that we used allow for a high yield and a high resistance.

Our novel trapping geometry for single-molecule protein unfolding experiments is shown schematically in Figure 3.6. Via a 4×c-myc tag at its C terminus, MBP is directly bound to microspheres coated with anti-c-myc antibodies. These microspheres are held by a micropipette. To be able to exert force on the protein, its N terminus is bound to an optically trapped microsphere via a covalently bound biotin, a streptavidin, a dsDNA linker (contour length 920 nm) with covalently bound biotin and digoxigenin molecules, and anti-digoxigenin antibodies. These connections enable a specific yet easy linking of both termini of the protein. This section will describe how the construct is established.

Experiments were performed in a flow cell as the one described in Chapter 1. For the experiments where SecB was added during the experiment, a flow cell was used with an additional input to flow in SecB-containing buffer when needed. In the tweezers setup, syringes that were connected to the left- and rightmost channels of a flow cell were filled with different microsphere suspensions: a suspension containing MBP-coated microspheres (MBP microspheres) and a suspension containing microspheres with dsDNA-tethered streptavidin tetramers (DNA microspheres). The syringe that was connected to the middle channel was filled with the reaction buffer, HMS/0.1% BSA(50 mM HEPES-KOH, pH 7.6, 100 mM KCl, 5 mM $MgCl_2$, supplemented with 0.1% bovine serum albumin [BSA]).

Next, the flow from the three syringes was started by applying pressure pulses (see Chapter 1) and tuned such that three separate unmixed flows could be distinguished next to each other. Using manually controlled linear stages, the flow cell was moved such that the optical trap was located in the flow carrying MBP microspheres. A microsphere was trapped and transferred to the micropipette, where it was held through suction. In the same way, also a DNA microsphere was trapped and transferred to the middle of the flow cell. Using the trackball mode of the Labview program, the microspheres could now be touched together to probe for a single DNA/MBP tether (Figure 3.6-1). In the preparation of the DNA microspheres, the DNA-to-microspheres ratio was tuned such that if two microspheres were tethered, it was via a single DNA linker (Figure 3.6-2a). Multiple tethers could be recognized by the occurrence of overstretching transitions at forces higher than ~65 pN (see Appendix A). After a single DNA/MBP construct had been tethered, a folding and unfolding experiment could be started. Using the piezo stage, the micropipette could be moved with respect to the optical trap, thus increasing and decreasing the force exerted on the termini of the protein to drive its unfolding (Figure 3.6-3) or to allow refolding. For an alternative set of experiments, a protein consisting of four in-tandem repeats of MBP was used (Figure 3.6-2b).

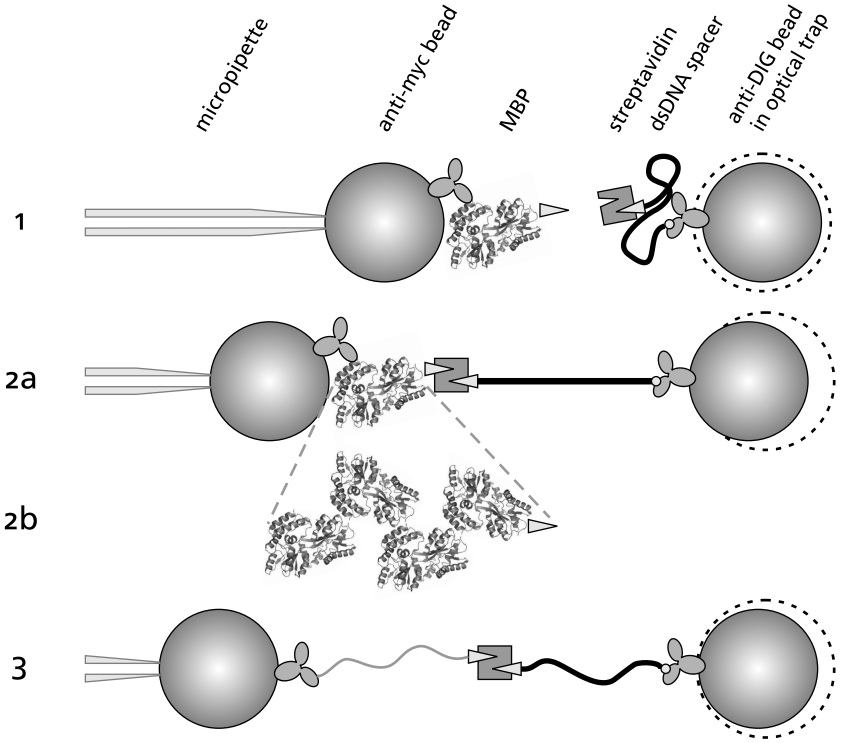
micropipette
anti-myc bead
MBP
streptavidin
dsDNA spacer
anti-DIG bead
in optical trap
1
2a
2b
3

Figure 3.6: Schematic view on some of the stages in an MBP unfolding and unfolding experiment. (1) To start an experiment, an anti-c-myc microsphere is pushed against a microsphere carrying streptavidin tetramers that were previously tethered using a dsDNA linker. (2a) After a connection has been made between the streptavidin and the biotin at the C terminus of MBP, the force exerted on the construct can be increased by moving the micropipette away from the optical trap. (2b) Alternatively, a protein consisting of four in-tandem copies of MBP could be used. (3) After unfolding of MBP, the construct consists of a coupled DNA linker and an unfolded polypeptide. Relaxing the construct allows for subsequent refolding of the polypeptide. Picture is not drawn to scale.

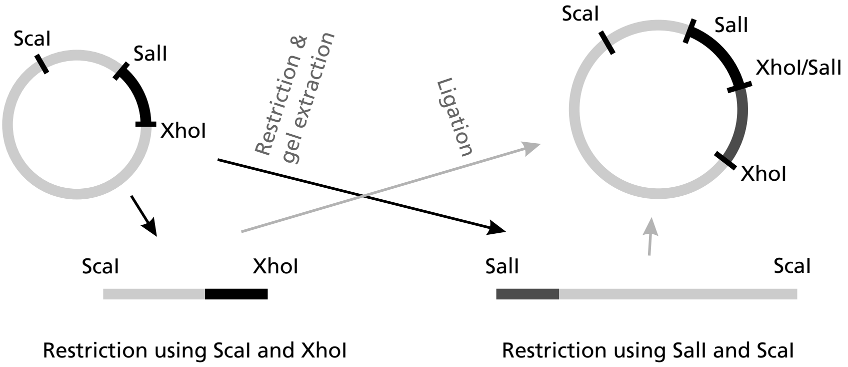
ScaI
SalI
XhoI
Restriction & gel extraction
Ligation
ScaI
SalI
XhoI/SalI
XhoI
ScaI
XhoI
SalI
ScaI
Restriction using ScaI and XhoI
Restriction using SalI and ScaI

Figure 3.7: Schematic illustration of the duplication strategy that was followed to make a 4×mbp protein. Two unique restriction sites with complementary cohesive ends (SalI and XhoI) were introduced on both sides of the *malE* gene (black) that was previously cloned in a plasmid (top left). Next, the plasmid was separately digested with ScaI/XhoI (bottom left) and SalI/ScaI (bottom right) and the indicated fragments were extracted from gel and ligated (top right), leading to a plasmid with a duplicated *malE* gene. This duplication strategy was subsequently repeated, resulting in a plasmid with four repeats of *malE*.

3.2.2 Cloning and protein expression of mbp constructs.

The *malE* gene of *E. coli* (encoding protein mbp) was cloned into plasmid pET3a, without the sequence corresponding to the translocation signal sequence. Using a polymerase chain reaction (pcr), a cysteine codon was introduced at the end of the gene corresponding to the N terminus of the protein. The sequence for a c-myc tag was introduced at the other end of the gene. Next, three more copies of this c-myc sequence were added by cycles of restriction, gel extraction of fragments and ligation.

For the 4×mbp construct, two unique restriction sites with complementary cohesive ends (SalI and XhoI) were introduced using pcr at both sides of the *malE* gene. Using the duplication strategy depicted in Figure 3.7, another copy of the *malE* gene was added, leading to a plasmid with two in-tandem copies of the *malE* gene. A second application of the duplication strategy led to a plasmid with four in-tandem copies of the *malE* gene with a single cysteine at one side and four c-myc tags at the other side of the gene.

After cloning, the proteins (mbp or 4×mbp) were expressed in *E. coli*. After lysis of the cells, mbp could be purified using the binding affinity of native mbp to an amylose resin (mbp binds to amylose with its maltose binding pocket). Also 4×mbp was successfully purified using an amylose resin, indicating that a 4×mbp polypeptide indeed folds into native, single-mbp subunits.

Finally, the cysteine at the N terminus of the mbp-constructs was biotinylated using biotin-maleimide. Free biotins were subsequently removed using dialysis.

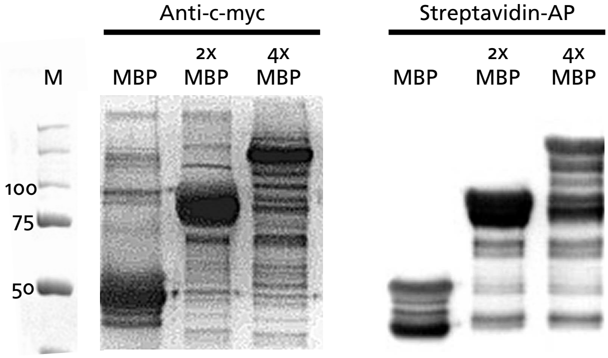

Figure 3.8: Immunoblots of purified MBP, 2×MBP and 4×MBP after biotinylation. The purified MBP constructs were positively tested for the presence of a c-myc tag at the C terminus and for a biotin at the N terminus using anti-c-myc and streptavidin-AP (alkaline phosphatase), respectively.

Figure 3.8 shows two immunoblots of purified MBP, 2×MBP and 4×MBP after biotinylation. These blots show that both biotinylation and cloning of the c-myc tag were successful.

3.2.3 Optical Tweezers setup

For the folding and unfolding experiments, the optical tweezers setup that was presented in Chapter 1 was used. The laser diode current of the setup was kept at 9 A. By fitting a Lorentzian to the power spectral density (PSD) of the movements of a trapped microsphere (see Chapter 1), the force constant of the optical tweezers and the sensitivity of the QPD were determined every day before doing experiments. On average, the force constant for a 1.88 µm polystyrene microsphere along the x coordinate was 169 pN/µm with a standard deviation of 24 pN/µm. The sensitivity of the QPD was on average ~2.74 V/µm with a standard deviation of 0.24 V/µm. The standard deviation of trap stiffness and sensitivity can be partially explained from the polydispersity of the microsphere suspension. The root mean square (RMS) of the noise in our force measurement was 0.11 pN (measured during 1 s).

During the experiments, microsphere movements were measured by recording the normalized QPD V_x and V_y signals at a frequency of 50 Hz. The analog electronics anti-aliasing filter was set at a filter frequency of 20 Hz. Additionally, the Labview particle tracking algorithm was used to track microspheres at a lower frequency (~5 Hz). For the analysis and for plots, the QPD data was used. The particle tracking data was only used for calibration.

FU sweep For the reproducibility of the folding and unfolding experiments, a special folding/unfolding (FU) sweep mode was developed with the following design

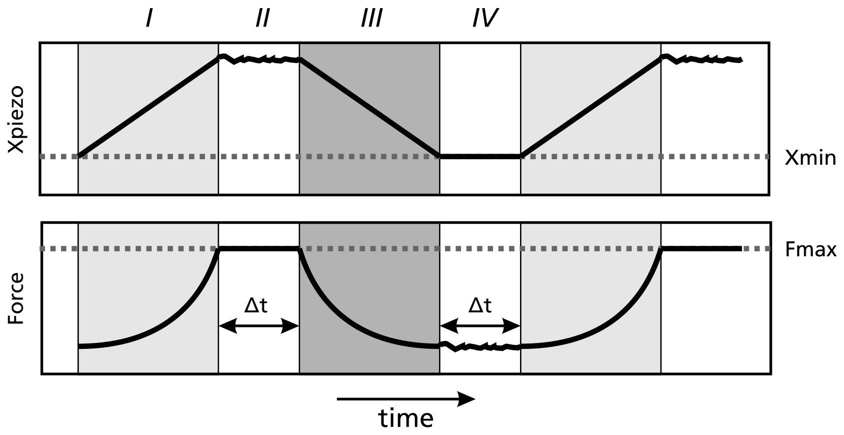

Figure 3.9: Schematic demonstration of the folding/unfolding (fu) sweep mode that was introduced for the mbp-unfolding experiments. The top graph shows the piezo x coordinate as a function of time. The bottom graph shows the force on a trapped microsphere in the x direction, measured by the quadrant photodiode (qpd) as a function of time. (i) the piezo x coordinate is increased at a constant rate (µm/s) until a force $F_{\max}$ on the tethered construct is reached. (ii) Next, the force was held at $F_{\max}$ for Δt seconds using a force-feedback mode. (iii) Now, the tether length was decreased again by moving back the piezo at a constant rate until position $x_{\min}$ is reached. (iv) At this position, the piezo was kept for Δt seconds before again increasing the tether length.

criteria in mind: (1) In forced unfolding experiments, the expected unfolding force (and also refolding) is dependent on the pulling rate (in µm/s). Hence, to keep the probability of unfolding of the protein at a certain force constant, the experiment should be performed at constant pulling rate. (2) After unfolding of a protein, refolding of a tethered polypeptide occurs after it has been held at low force for a certain period. To keep the probability of refolding between relaxing and pulling constant throughout the experiment, the time to allow the refolding should be kept fixed. (3) To avoid breaking of the construct, the exerted force should remain limited.

In Figure 3.9, the fu sweep mode is demonstrated schematically. The fu sweep consists of different phases: (i) Stretch phase: After switching on the sweep mode, the piezo x coordinate is moved at a constant rate (µm/s) such that the force increases. (ii) Hold phase: Once the force on the tethered construct reaches a preset force $F_{\max}$, the force is held at this force for Δt seconds (generally set at 10 s) to make sure the protein is completely unfolded. (iii) Relax phase: Now, the tether length is decreased again by moving back the piezo at a constant rate until position $x_{\min}$ is reached. (iv) Slack phase: At this position, the piezo is kept for Δt seconds before again (i) increasing the tether length.

If $F_{\max}$ is set high enough (40 pN), unfolding will occur before the hold phase is reached. Refolding can occur after again relaxing the construct (i. e., in the relax phase or the slack phase).

In the stretch and relax phases of the FU sweep, the piezo was moved with a rate of 50 nm/s. At the force range where unfolding occurs, this corresponds to a loading rate of ~7 pN/s (at these forces, the DNA is already at >95% extension and piezo movement will mostly result in movement of the trapped microsphere inside the trap where the force F is proportional to the distance x with trap stiffness k_x ca. 150 pN/µm).

3.2.4 Microsphere preparation

Anti-c-myc and anti-digoxigenin (anti-DIG) antibodies (Roche Diagnostics) were covalently coupled to carboxyl-functionalized 1.87 µm-sized polystyrene microspheres (Spherotech) using the crosslinker carbodiimide. A commercially available kit including all needed buffers was used for this crosslinking reaction (Polysciences, cat. no. 19539-1). In this protocol, 100 µg of antibody was coupled to 250 µl 5% w/v microsphere suspension.

Both the anti-c-myc- and the anti-DIG-coated microspheres were blocked using bovine serum albumin (BSA, Sigma-Aldrich). Here, 20 µl of microsphere suspension was diluted in 500 µl 1× HMS (50 mM HEPES-KOH, pH 7.6, 100 mM KCl, 5 mM $MgCl_2$) with 1% w/v BSA. The microspheres were incubated with the BSA for 30 minutes at room temperature in a hand-over-hand mixer. Next, the microspheres were spun down by a table centrifuge for 1 minute at full speed after which the supernatant was removed. This blocking protocol was repeated and the microspheres were resuspended in 20 µl HMS with 0.1% w/v BSA.

Next, the anti-c-myc microspheres were coated with the biotinylated MBP-4×c-myc. First, the MBP was diluted 100-500 times in HMS/0.1% BSA. Next, 0.5 µl of the diluted MBP and 2 µl of anti-c-myc microspheres were diluted in 20 µl of HMS/0.1% BSA. The microspheres were incubated with the MBP for 30 minutes at 4°C in a hand-over-hand mixer. Next, to remove unbound MBP, microspheres were washed in 500 µl HMS/0.1% BSA and, after spinning the microspheres down, resuspended in 400 µl HMS/0.1% BSA.

In the MBP-unfolding experiments, a DNA linker was used with a contour length of 920 nm. This linker was created by performing a polymerase chain reaction (PCR) on pUC19 DNA with a forward primer carrying two biotin groups and a reverse primer carrying two DIG groups. This DNA linker was bound to streptavidin (SA) by mixing ~250 ng of DNA with 0.4 µg/ml streptavidin (Molecular Probes) in 10 µl HMS/0.1% BSA. This is an excess of streptavidin, hence every streptavidin tetramer has at most one DNA linker bound.

Next, the DNA/SA mixture was added to 2 µl anti-DIG microspheres diluted in 10 µl HMS/0.1% BSA. After incubating the DNA and the microspheres for 30 minutes at 4°C in a hand-over-hand mixer, 400 µl of HMS/0.1% BSA was added.

3.2.5 Steered molecular dynamics studies

SMD simulations were performed at AMOLF by Harald Tepper. For the SMD simulations, the crystal structure of MBP without a bound sugar (PDB-ID 1JW4 [54]) was used as a starting structure. Missing atoms were added after analysis of the PDB structure using the SCWRL program [72]. Moreover, some side chains were flipped as suggested by this program. Next, several histidines were replaced by an HSD (neutral histidine with a proton on the N_δ) and hydrogens were added to the protein using `psfgen`.

Next, the protein and its crystallographic water molecules were solvated in a previously equilibrated water box, extending at least 10 Å from the protein in all directions. All water molecules within 2.4 Å from the atoms in the crystal structure were removed. Subsequently, the system was neutralized by replacing 8 water molecules by Na^+ ions. The final box contained 5378 protein atoms, 13,613 water molecules and 8 counterions (46,217 atoms in total). To relax unphysical contacts between protein and water, the system was energy-minimized for 500 steps, followed by 2000 time steps (4 ps) of canonical MD (298 K) with the protein atoms fixed in space, and 10,000 steps (20 ps) with all atoms free. The pressure at the end of this stage was -700 bar. In a series of consecutive constant pressure simulations (10,000 steps each), the system was brought to a pressure of 1 bar. From this stage, a further extensive equilibration run was launched (T = 298 K, p = 1 bar) that lasted $1 \cdot 10^6$ steps (2 ns). After ~0.5 ns, the total energy and volume had become stable. The final box dimensions measured $68.03930 \times 76.66410 \times 87.2054$ Å^3.

For the MD simulations, the program NAMD [73] was used with force field CHARMM22 [74] for the protein and the TIP3P model [75] for the water molecules. The long-range electrostatic interactions were treated with the Particle Mesh Ewald (PME) technique, with a tolerance of 10^{-6} and a Fourier grid size of $72 \times 81 \times 90$. Van der Waals interactions were cut off at 10 Å with smooth interpolation to 0 from 9 Å. Full electrostatics were calculated every 2nd time step. A Langevin thermostat was applied to the non-H atoms, with a damping coefficient of 5 per ps. All bonds to hydrogens were fixed.

To induce unfolding in the simulated protein, two springs (with force constant 5 kcal/mol/Å^2, or $3.5 \cdot 10^6$ pN/μm) were attached to the N of Lys1 and the C_α of Lys370, respectively. In the unfolding simulations, one of the two springs was moved along the vector between the initial positions of the two atoms while the other spring was kept fixed. In our study, we used pulling rates of 0.1 nm/ns (slow) or 1 nm/ns (fast). For analysis purposes, configuration files were written to disk every 1000 time steps and spring forces every time step.

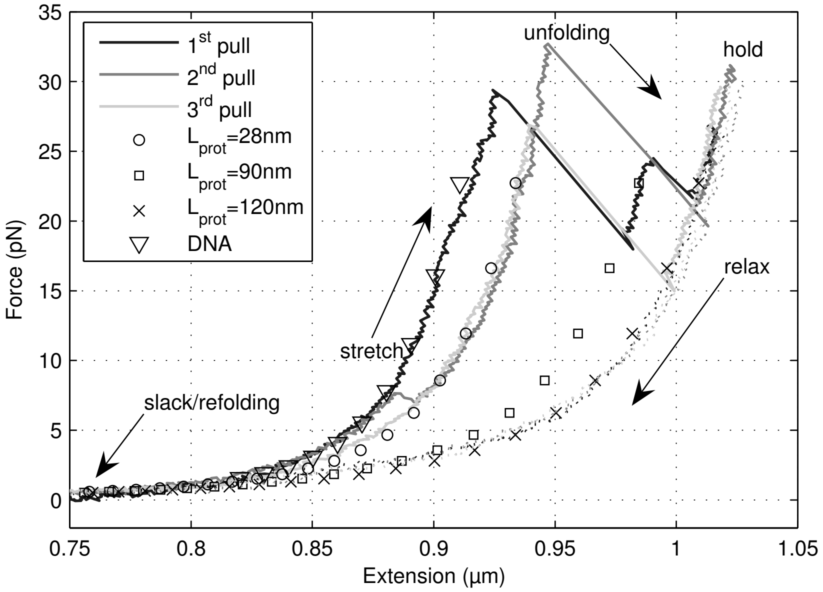

Figure 3.10: Forced unfolding of MBP using optical tweezers. Three consecutive stretch-relax cycles are shown. Two unfolding intermediates can be observed. Additionally, calculated WLC curves are shown for a DNA strand (L = 920 nm, P = 53 nm, S = 1200 pN) and for DNA/polypeptide constructs with different polypeptide contour lengths (L = 28, 90, 120 nm, P = 1.5 nm, S = 1200 pN).

3.3 Results

3.3.1 Forced unfolding of MBP using optical tweezers

To characterize the forced unfolding of MBP, an MBP/DNA construct was tethered between two microspheres, as described in the previous section. By starting the FU piezo sweep mode, an unfolding experiment was started. In Figure 3.10, an example is shown of the force–extension curve resulting from such an experiment showing three consecutive cycles of the FU sweep (stretch→hold→relax→slack, etc.) in increasingly lighter shades of gray.

The triangles (▽) show the force–extension of an extensible worm-like chain (WLC, see Appendix A) corresponding to the dsDNA linker with a persistence length P of 54 nm, a contour length L of 920 nm and an elastic stretch modulus S of 1200 pN. The crosses (×) show the force–extension of two coupled worm-like chains: an extensible WLC corresponding to DNA with properties as mentioned before and an inextensible WLC corresponding to a polypeptide with contour length L = 120 nm. For the polypeptide WLC, a persistence length of 1.5 nm was chosen as

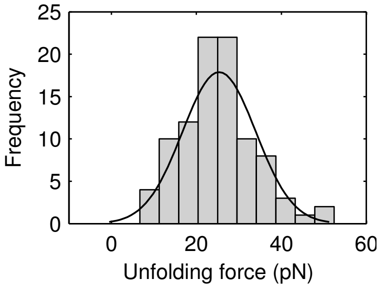

Figure 3.11: Histogram of unfolding forces from 94 unfolding events of 27 MBP molecules. A Gaussian fit to the data is shown. The average unfolding forces was found to be 25.4 pN with a standard deviation of 8.6 pN.

it gave the best fit to the data.

The first stretch curve (black) in Figure 3.10 first follows the DNA WLC curve. At a force of ~29 pN, a sudden change in force and extension can be observed, indicating an unfolding event of the tethered protein. By fitting DNA+polypeptide WLC curves with varying polypeptide length, it was determined that the additional contour length of the polypeptide due to this unfolding event amounts to ~90 nm (cf. □-curve). When the force is further increased to a force of ~24 pN, the protein further unfolds. The total polypeptide contour length due to this unfolding event is 120 nm (cf. ×-curve). This length corresponds to a fully extended MBP polypeptide chain (taking 3.3 Å per amino acid [9]) indicating that here, the protein has completely unfolded to a conformation with all secondary structure removed. Apparently, in the first unfolding event, a part of the MBP structure corresponding to 90 nm/120 nm×370 amino acids = ~278 amino acids has unfolded.

After complete unfolding, the first relax curve (black) follows the DNA+polypeptide WLC curve until the slack phase (10 s waiting time at low force) of the FU sweep is reached, indicating that MBP did not significantly refold during that stage.

The second stretch curve (dark gray) first follows the DNA WLC curve again, indicating that the polypeptide has completely folded in the 10 s waiting time. At ~7 pN, the protein unfolds to an unfolding intermediate with a polypeptide contour length of 28 nm (cf. ○-curve), corresponding to ~85 amino acids. Eventually, at ~32 pN, this intermediate also completely unfolds. After relaxing the construct again, the third stretch curve shows that the polypeptide apparently only partially refolded to the same intermediate that was reached in the second cycle. Similar to the first relax curve, the second and third relax curves showed no refolding.

Next, the unfolding force of 94 unfolding events from 27 unfolded MBP molecules were analyzed. The histogram that is shown in Figure 3.11 gives an overview of the observed unfolding forces. If unfolding occurred via one or several intermediates, the unfolding event leading to the highest additional polypeptide contour length was analyzed for this histogram. In >90% of the analyzed stretch curves, these events corresponded to the unfolding event with the highest unfolding force. In >65% of the cases, these events led to the complete unfolding of the protein. The average unfolding force for the analyzed unfolding events was at 25.4 pN with standard deviation 8.6 pN. The spread in the force can be partially explained from

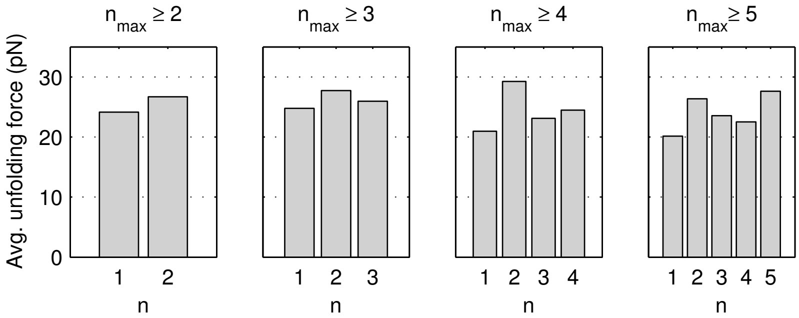

Figure 3.12: Development of the unfolding force of MBP. Every bar represents the unfolding force of the *n*th unfolding event, averaged over all measurements with a total number of unfolding events n_{max} before the end of a measurement.

the stochastic nature of protein unfolding. Additionally, inaccuracy of the trap stiffness parameter contributed to the width of the distribution.

To study whether MBP is folding back to its native state after having unfolded it, the unfolding force as a function of the number of times a protein has been unfolded was studied. Figure 3.12 shows the development of the unfolding force of MBP proteins that were unfolded multiple times. For the graphs in this figure, we used the same dataset as for the unfolding forces histogram in Figure 3.11. It can be observed that the first unfolding event of a molecule occurs at the same force as later unfolding events. No trend up- or downward can be observed, indicating that refolding happens to the same state every time. This state is thus a reproducible starting state before pulling and is most likely the native state of the protein.

Next, the same set of measurements was analyzed for the occurrence of intermediates. All measurements gave clear evidence of intermediates that are stable for seconds under load. An unfolding intermediate with a polypeptide contour length of ~25–30 nm, as in the above example, was observed in all measurements. The mean unfolding force for 17 unfolding events leading to this intermediate was 16.5 pN with standard deviation 11.1 pN.

The refolding of the polypeptide to the native state only occurred in the slack phase of the FU sweep, in all of the analyzed measurements except one. In one of the measurements, however, refolding was observed in the relax phase of the FU sweep. Refolding was visible as an increase of force because of the increased tension due to the shortening of the tether. The event is shown in Figure 3.13.

Several control experiments were performed to confirm that the observed phenomena indeed originated from unfolding of a tethered MBP protein, and not from artifacts stemming from the other components used in the experimental configuration: (I) To check whether the connection between the protein and the micropipette microsphere is via the 4×c-myc tag and the anti-c-myc antibody and not through aspecific interactions between the protein and the microsphere, a

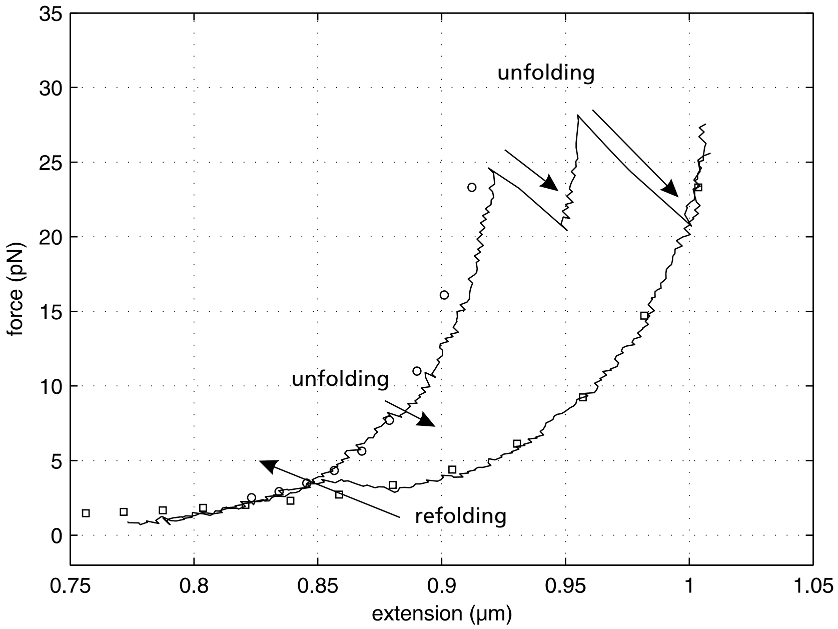

Figure 3.13: Forced unfolding experiment of mbp showing three unfolding events and a clear refolding event at low force. Two wlc curves are shown as in Figure 3.10.

control experiment was performed with anti-His$_6$ microspheres instead of anti-c-myc microspheres. (Microspheres were prepared with anti-His$_6$ antibodies [Roche Diagnostics] as described in §3.2.4). In this control experiment, the observed tethers broke at very low force, indicating that non-specific protein-antibody interactions are not strong enough to sustain forces needed to unfold a protein. (ii) To ensure that the observed drop in force was indeed from unfolding of the mbp protein, a control experiment was performed using biotinylated c-myc epitopes (a 10-aa polypeptide). In this experiment, tethers were observed that could be extended to overstretching of the dna linker (>60 pN), but without sudden force drops, indicating that the observed force drops were from unfolding of mbp.

3.3.2 Forced unfolding of a 4×mbp construct.

To further investigate the unfolding behavior of mbp, we performed unfolding-and-refolding experiments with the 4×mbp construct that was described in §3.2.2. For a 4×mbp construct, the distance between each of the mbp subunits and the polystyrene surface is higher, so less surface effects are expected. The protein was tethered between a dna spacer and a micropipette microsphere as described in §3.2.1 and an experiment was started by switching on the fu sweep.

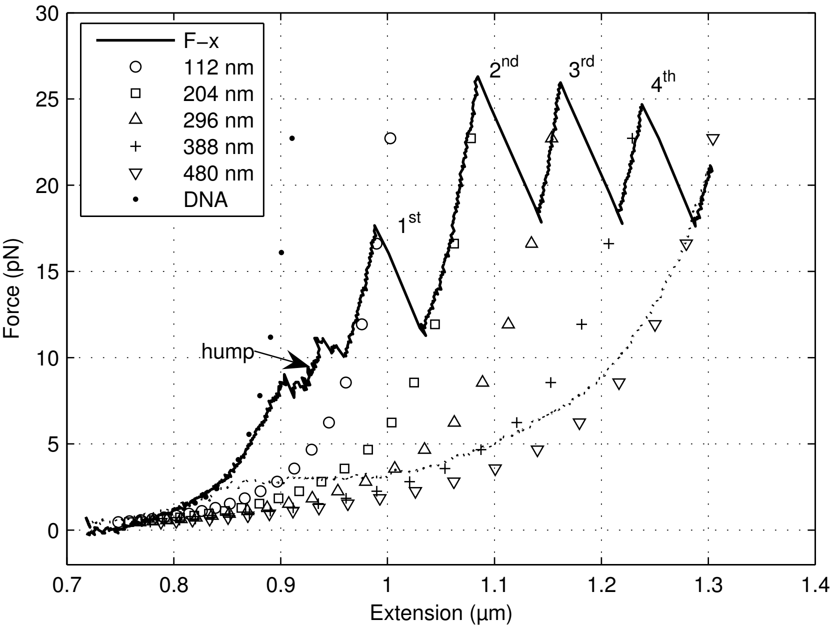

Figure 3.14: Forced unfolding of 4×MBP using optical tweezers. A stretch and relax curve are shown. Four major unfolding events can be observed (labeled 1st–4th), corresponding to unfolding of each of the four MBP subunits. Moreover, a hump-like feature can be seen at extension 0.8 µm. WLC curves were fit to estimate contour lengths.

An example of an unfolding measurement of 4×MBP is shown in Figure 3.14. Following the stretch curve of the measurement, the force–extension curve first resembles DNA WLC behavior. At a force of ~10 pN, a rugged force plateau or 'hump' can be observed that extends until an additional ~100 nm extension. Now, the force further increases and four major unfolding events (labeled 1st–4th) can be seen at forces between 15 and 21 pN. WLC curves were fit to the observed intermediate in order to estimate contour lengths. These fits are shown in the figure.

The observed 'hump' at a force of 10 pN was observed in most of the 4×MBP-unfolding measurements. Careful examination of the hump shows multiple small force drops, resembling unfolding of domains each leading to a several-nm increase of contour length. These events resemble the ~16.5 pN/~25–30 nm unfolding events that were observed in the single-MBP case. A likely explanation for the 'hump' is the unfolding of four of these easily unfoldable domains in the MBP subunits that unfold prior to the complete unfolding of the rest of each of the proteins. Figure 3.14 shows a WLC fit to the intermediate that is reached after the hump. This intermediate leads to an additional polypeptide contour length of 112 nm, or four times 28 nm, which fits perfectly in the range of the first intermediate which we found to be between 25

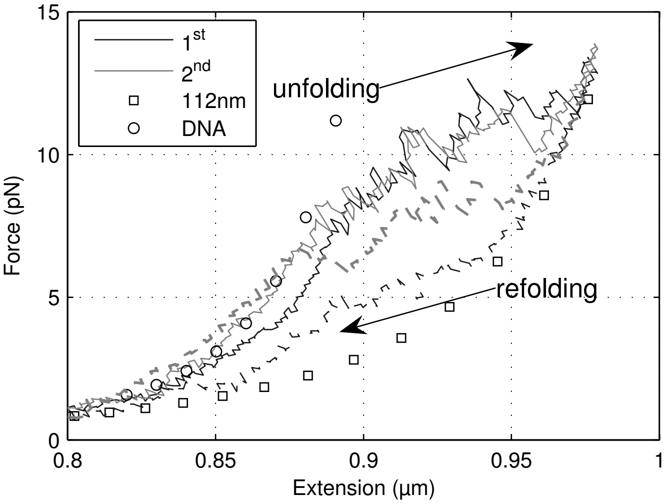

Figure 3.15: Detail showing unfolding and refolding of subdomains in the 4×mbp construct. As a reference, two calculated wlc curves are shown, corresponding to the dna linker and to the dna linker coupled to a polypeptide of 112 nm contour length.

and 30 nm. In the next section we will show molecular dynamics simulations that suggest a molecular mechanism for these low-force unfolding events.

Figure 3.15 shows a zoomed-in representation of a hump feature in a different measurement. After the hump was observed at ~10 pN, the force was decreased again by moving the micropipette. First, one can see that the force–extension curve follows a dna/polypeptide wlc curve with a polypeptide contour length of 4×28 nm = 112 nm. At a force of 8 pN and lower, a decrease in extension could be observed, that was more than what could be predicted by the wlc model (□-curve). This can be explained by refolding of the domains that previously unfolded in the hump feature.

The four labeled unfolding events in Figure 3.14 likely represent the consecutive unfolding of the rest of each of the mbp subunits. All four unfolding events led to a similar increase in polypeptide contour length and happen at comparable forces. The unfolding forces for 26 of such unfolding events are plotted in the histogram in Figure 3.16. These unfolding force correspond very well to unfolding forces observed for the single-mbp experiments (see the histogram in Figure 3.11).

Consistent with the single mbp studies, no sudden refolding events can be observed in the subsequent relax curve. This was the case in all other measurements that were performed on this 4×mbp construct.

No refolding as in the single-mbp case was observed after the 10 s waiting time in the slack phase. If the extension was again increased in a second stretch sweep, the contour length of the unfolded polypeptide appeared to have become shorter,

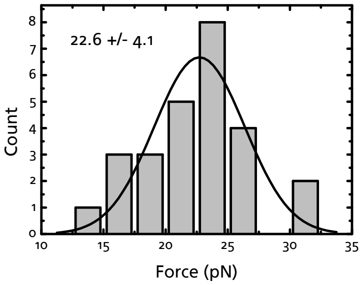

Figure 3.16: Histogram of unfolding forces from 26 unfolding events of 7 4×MBP molecules. A Gaussian fit to the data is shown. The average unfolding forces was found to be 22.6 pN with a standard deviation of 4.1 pN.

indicating that refolding did happen to some degree. However, often the construct could be extended to overstretching of the DNA linker without any unfolding occurring, possibly indicating that the different MBP subunits had formed one big aggregate that was too stable to unfold.

In several cases, refolding of some of the MBP subunits was observed, however. Figure 3.17 shows an experiment in which refolding was observed multiple times. It shows three cycles of the FU piezo sweep in increasingly lighter shades of gray. In the first stretch curve, the unfolding of three MBP subunits can be observed. In the next stretch curve, it can be seen that one of the three previously unfolded MBP subunits has refolded: two unfolding events (at 4 pN and at 14 pN) can be observed before the construct reaches its full extension. The third stretch curve shows the same pattern, indicating that, again, two of the four MBP subunits have refolded.

These experiments also confirm that in our novel single-DNA linker approach, the surface has no detectable influence on the unfolding and refolding of a protein. In the 4×MBP case, the chain of MBP subunits has to be pulled away from the surface, before they can be unfolded. In the subsequent unfolding, three of the four MBP subunits will unfold at a distance from the microsphere larger than the size of one MBP subunit (5 nm). Hence the polystyrene surface is too far away from the protein to affect its unfolding. The unfolding forces found in the unfolding of 4×MBP fall well within the distribution of unfolding forces that was found for MBP (see Figure 3.11). Moreover, similar unfolding intermediates can be observed. This strongly suggests that also in the single-MBP case, unfolding happens without significant influences from the nearby polystyrene surface. Moreover, the results summarized in Figure 3.12 indicate that also the *folding* of a protein can occur unaffected by the nearby surface. Apparently, the anti-c-myc antibody that is connected to the C terminus of the protein provides enough distance to the microsphere surface. Moreover, the constant tension at which the construct is held during a measurement, orients the molecule away from the surface. Hence, the experiments shown in this section support the use of our approach in single-molecule protein unfolding experiments.

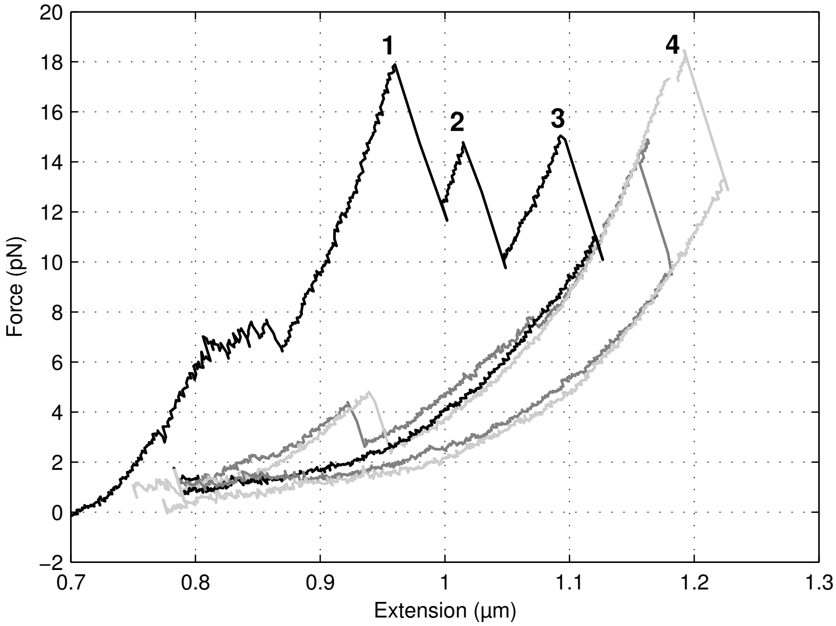

Figure 3.17: Forced unfolding and refolding of 4×mbp using optical tweezers. Force–extension curves from three consecutive fu cycles are shown. Refolding of two mbp subunits can be observed between the first and the second cycle and between the second and the third.

3.3.3 Steered molecular dynamics simulations on the forced unfolding of mbp

The single-molecule unfolding experiments on the maltose-binding protein that were presented in the previous section showed unfolding intermediates. Some of these intermediates were remarkably strong and were stable for up to seconds under a load of sometimes more than 30 pN. From the visual inspection of the mbp crystal structure (shown in Figure 3.4), no obvious intermediates could be predicted. Also previous bulk unfolding studies on the maltose-binding protein did not point to stable unfolding intermediates. The bilobate mbp structure suggests a stepwise unfolding mechanism, in which both lobes unfold separately. Close examination, however, shows that both lobes are highly entangled and the polypeptide chain crosses the 'bridge' between the two lobes several times. It is thus likely that separate unfolding of a lobe will cause the unfolding of the full protein.

To better explain the observed unfolding intermediates, we undertook steered molecular dynamics (smd) simulations. In steered molecular dynamics, external forces can be exerted on individual atoms in a molecular-dynamics simulation to drive—on the timescale of md simulations—rare events such as protein translocation [76] and protein unfolding [77, 68]. We performed MD simulations on the unfolding of the MBP structure, while exerting an external force on C and N termini. This was done by attaching virtual springs with a fixed spring constant to both termini and increasing the force by moving one or both springs. Note that to be able to observe an unfolding event within the timescales typical for MD simulations using a high-end, multi-node computer—tens of nanoseconds—one must move the spring with a speed that results in a pulling rate (in pN/s) that is many orders of magnitude higher than in optical tweezers experiments (~10^{12} pN/s vs ~10 pN/s). The discrepancy between the sampled timescales in simulation and experiment makes that we have to be cautious with the interpretation of the results. We will show that by pulling on both ends of the molecules and by comparing two different pulling speeds, we can still draw reasonable conclusions about the order in which the different residues will unfold when force is applied to MBP.

In Figure 3.18, a number of snapshots is shown from two SMD simulations that were performed at a high pulling rate ($3.5 \cdot 10^{12}$ pN/s). The four snapshots on the left side show an experiment where the spring that was attached to the C terminus was moved at a speed of 1 nm/ns. In the four snapshots on the right side, the moving spring was attached to the N terminus. Close examination of the C-terminal structure (see, e. g., Figure 3.20) shows a surface-exposed α-helix. At the N terminus, the first five amino acids constitute a loop domain that is coupled to a buried β-strand. Figure 3.18 shows that, when pulling from the C terminus, the first α-helix can detach from the MBP structure within nanoseconds, while the N-terminal loop is still attached to the surface. When pulling from the N terminus, it is the loop domain that detaches first from the structure. After 3–4 ns, also the C-terminal α-helix detaches, while the first N-terminal β-strand remains buried and the hydrogen-bonds to neighboring β-strands are maintained.

The difference between the two experiments seems remarkable. Because of Newton's third law, one would expect the force exerted on the termini to be equal in magnitude and opposite in direction. Unfolding behavior is then independent of the position of the moving spring. Instead, we do see a difference. This shows that the effect of the force on one of the two termini propagates through the protein at a finite speed. The other protein terminus will only be affected by a force after a certain time.

During the SMD simulations, the forces exerted on the two termini were recorded. Figure 3.19 shows the forces that were exerted on the termini during the experiment that was shown in Figure 3.18. In both graphs, the light gray curves on the background shows the force signal as it was recorded during the simulations. Note that the RMS of this signal—that is mostly caused by collisions with the surrounding water molecules—is enormous (~100 pN) compared to the forces measured in optical tweezers experiments. On longer timescales, the average effect of this thermal force is nearly zero. After processing the raw force data using a Savitzky-Golay smoothing algorithm, we can analyze the force exerted by the springs. In both graphs, the black curve shows the force exerted on the C terminus, projected on the line connecting the two termini at $t = 0$. The dark gray curve shows the force exerted

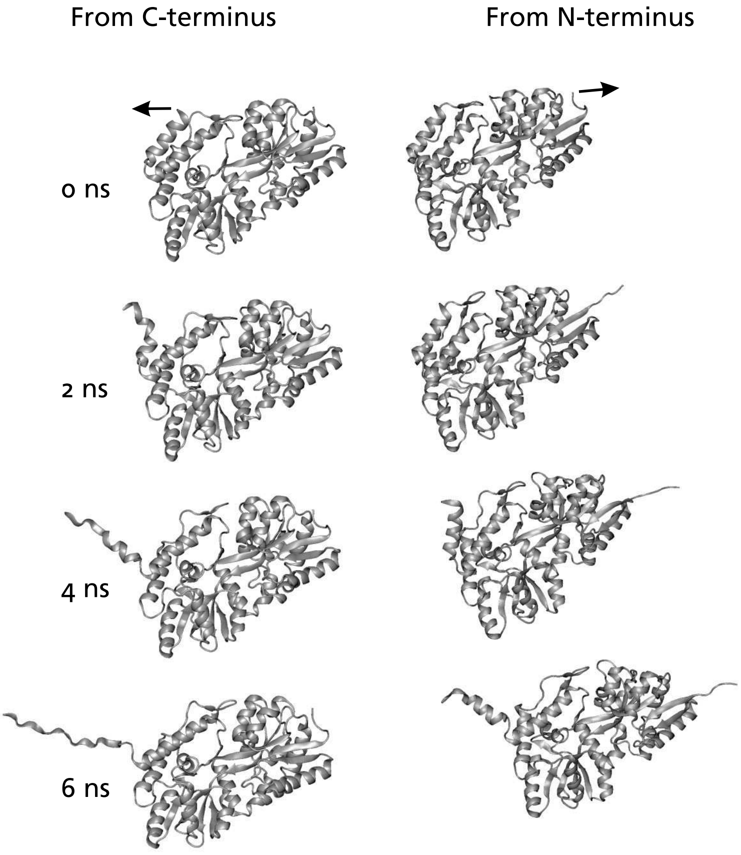

Figure 3.18: Steered molecular dynamics (smd) simulations on the forced unfolding of mbp. Two separate experiments are shown with each four snapshots. On the left side, the spring attached to the C terminus is moved at a speed of 1 nm/ns (see arrow) while the other spring is held fixed. On the right, the spring attached to the N terminus is moved. Figures were prepared using vmd [50].

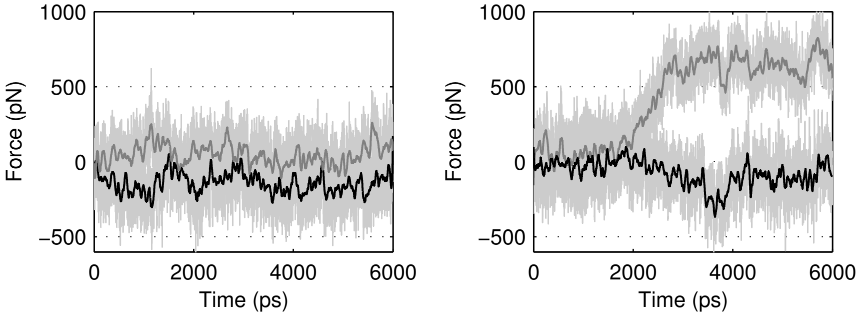

(a)

(b)

Figure 3.19: Forces exerted on C and N terminus during the SMD experiments that were shown in Figure 3.18. (a) Pulling from C terminus. The light gray signal is the force as it was measured. The dark gray and the black curves are the forces exerted on the N terminus and the C terminus respectively after smoothing the raw (light gray) data using a Savitzky-Golay smoothing algorithm. (b) Pulling from N terminus.

on the N terminus. The forces shown in Figure 3.19a must be averaged with forces from additional experiments to anneal out viscous effects in the measured forces. In Figure 3.19b, we can see a significant rise in the force exerted on the N terminus starting at ~2 ns. The force rises until the value is around 700 pN. Comparison with the snapshots in Figure 3.18 shows that the rise in force likely corresponds to the moment when the easily unfoldable N-terminal loop has detached and force is mainly used to translate the protein and to detach the C-terminal α-helix at the other side of the protein.

These simulations clearly show that the C-terminal α-helix can be detached from the MBP structure at forces that are several times lower than those needed for the eventual disruption of the N-terminal β-strand from the structure. In fact, we did not see such a disruption.

Because of the finite size of the simulation box with periodic boundary conditions, it was not possible to drive extension of the protein further than what is shown above. Instead, we developed a new technique to avoid problems with the finite size of the simulation box. We performed a series of SMD simulations with progressively truncated MBP primary structures. After each SMD simulation, we removed those residues from the PDB structure that detached most easily, filled the resulting gaps with water molecules and performed a new pulling SMD simulation. Thus, we progressively removed the sequence that is indicated in black in the structure representation of MBP that is shown in Figure 3.20 (corresponding to amino acids 1–5 and 285–370). The carbon atoms of the residues at the positions where the protein was truncated are indicated as white spheres. Between these amino acids, the structure mostly consisted of surface-exposed α helices. The sequence between amino acids Gly327 and Met336 was partially covered by a hairpin-like

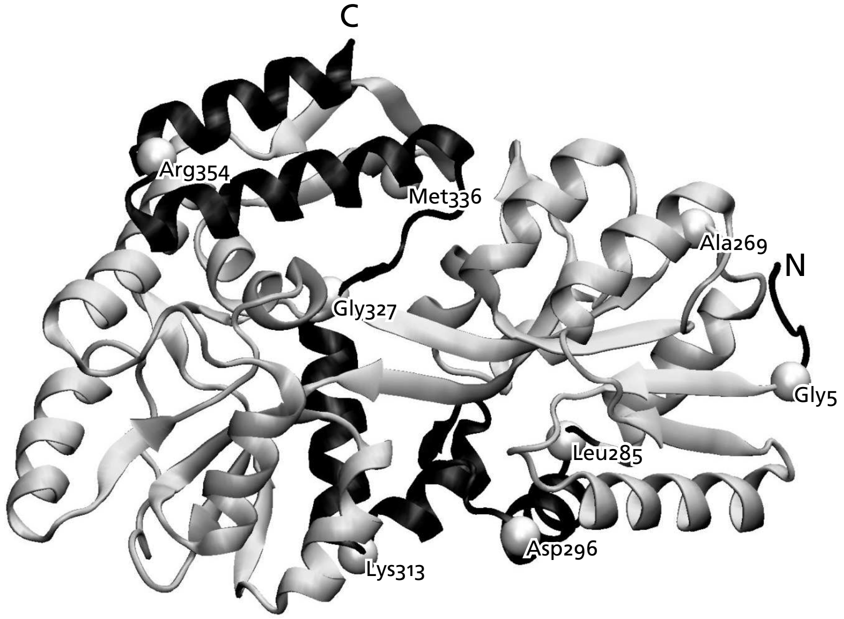

Figure 3.20: Cartoon representation of the MBP structure. Amino acids 1–5 and 285–370 are indicated in black. The C atoms of the residues at which the protein was truncated before SMD simulations are shown as white spheres. Figure was prepared using VMD [50].

structure, but in the simulations, this structure was shown to be flexible enough to allow detachment of the sequence shown in black.

These simulations suggest that in the unfolding of MBP, it is amino acids 285–370 that will detach from the protein in a first unfolding event. Earlier bulk mutation studies [58] support the existence of a more stable structure beyond this sequence. These studies showed that in the adjoining α helix (amino acids 269–285) two amino acids (276 and 283) are located that are crucial for folding [58]. Detachment of this α-helix from the MBP structure might lead to global instability of the protein and hence to complete unfolding. Indeed, an unfolding simulation (at high pulling rate) with also amino acids 269–285 removed did lead to global loss of tertiary structure. A simulation at a lower pulling rate should be performed to confirm this. In an extended conformation without secondary structure, detached amino acids 285–370 correspond to a polypeptide contour length of ~28 nm (using 0.33 nm as the contour length per amino acids). In our optical tweezers studies, we observed a predominant unfolding intermediate having a remarkably similar polypeptide contour length. Long equilibration simulations are underway for the different truncated constructs to test their long-term stability.

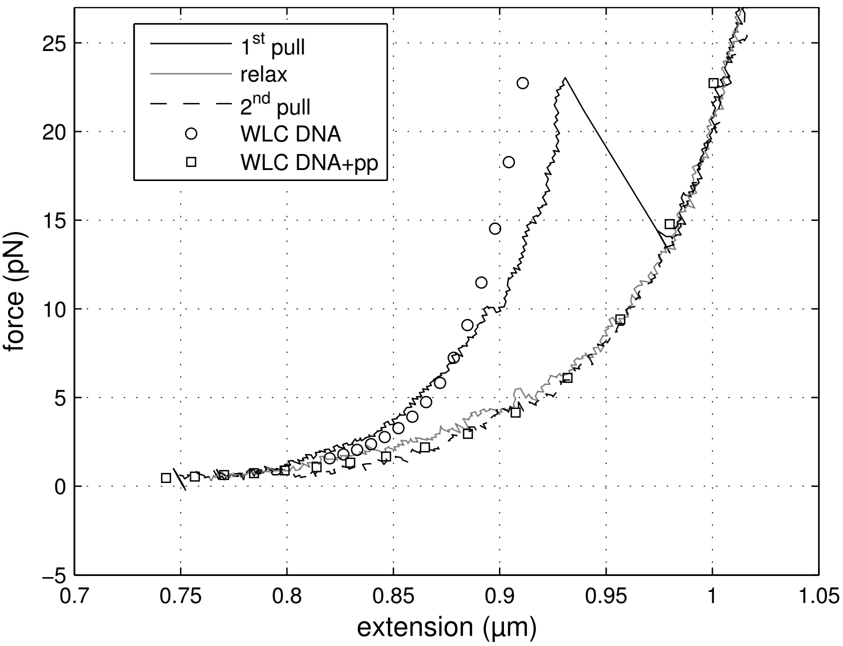

Figure 3.21: Forced unfolding of MBP in the presence of a nearly-physiological concentration of chaperone protein SecB. Two consecutive stretch-and-relax sweeps are drawn. These show that the addition of SecB alone is not enough to unfold MBP and that the eventually unfolded MBP cannot refold.

3.3.4 The effect of chaperone SecB on the forced unfolding of MBP

To study the effect of chaperone protein SecB on the unfolding and the folding of a protein, we used the single-MBP construct that was used in the unfolding-refolding experiments described in §3.3.1. These experiments showed that this protein can repeatedly be unfolded and refolded to its native state, making it an ideal substrate protein for studies of the effect of SecB.

After performing a normal unfolding-refolding experiment to ensure that a single MBP protein was tethered and that it could be unfolded completely and repeatedly refolded to its native state, the construct was held at a force low enough to allow the protein to refold and high enough to extend the DNA to ~80% of its contour length to avoid microsphere-microsphere interactions. Now, buffer with a nearly-physiological concentration of SecB (HMS/0.1% BSA with 0.1 µM SecB added) was introduced via a fourth input in the flow cell. Once the SecB-containing buffer had reached the tethered protein, another FU sweep was started.

In Figure 3.21, an example is shown of an unfolding-refolding experiment after the addition of SecB. The first stretch curve follows the DNA WLC curve, until a first

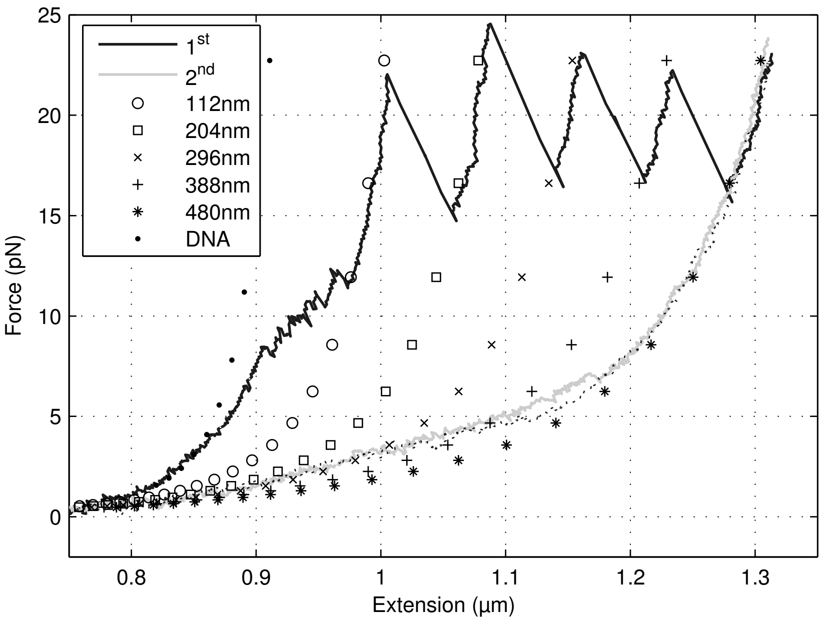

Figure 3.22: Unfolding of 4×mbp in the presence of SecB. Two consecutive stretch-relax cycles are shown. Stretch curves are shown as uninterrupted lines; relax curves are shown as interrupted lines. Different calculated wlc curves are shown to suggest the contour length of the unfolded polypeptide(in nm) of each of the observed intermediates.

minor unfolding event at ~10 pN. Complete unfolding of the resulting intermediate occurs at ~22 pN, which agrees with our observations described in §3.3.1. This shows that mbp remains in its native state when SecB is added. As in the absence of SecB, the subsequent relax curve follows the dna+polypeptide wlc curve. Remarkably, the 2nd stretch curve again follows this dna+polypeptide wlc curve, showing that no refolding of the mbp occurred in the slack phase. Also the subsequent stretch curves showed this same behavior. In all the measurements performed in the presence of SecB, careful analysis of the stretch curves also did not reveal any low-force unfolding events that could be explained from a lowering of the unfolding force due to the effect of SecB.

After a second buffer replacement to remove the SecB, often some of the connections of a tethered construct would break due to the strong flow. Hence, We could not perform a measurement to show the eventual unbinding of SecB from mbp as of yet.

Next, we performed unfolding experiments with the 4×mbp construct with SecB present continuously. Figure 3.22 shows an example of a measurement. This figure shows two consecutive stretch-relax cycles, measured in a buffer containing 0.1 µM

SecB. The first stretch curve shows similar features to the measurements that were discussed in §3.3.2: first the hump at ~10 pN, and then four consecutive unfolding events at 20–25 pN. Different calculated WLC curves are drawn, showing that the observed measurements can well be described by the simultaneous unfolding of 4×85 amino acids (4×28 = 112 nm) in a first low-force event, the hump, followed by the sequential unfolding of the rest of each MBP protein (92 nm) at a higher force.

After relaxing the construct, the second stretch curve shows no refolding of each of the four MBP proteins. The stretch curve follows the earlier relax curve. This is a behavior that is quite different from the situation where SecB was absent. There, the protein construct would show refolding or—more often—irreversible aggregation. Hence, this measurement confirms that indeed, SecB prevents folding of a polypeptide as well as the irreversible aggregation of multiple polypeptides.

The relax curves and the second pull curve in Figure 3.22 show a striking deviation at low force from the theoretical curve of a DNA/polypeptide WLC with a polypeptide contour length corresponding to the fully unfolded 4×MBP polypeptide (∗). At a force of 5 pN, the extension of the construct is shorter than what can be predicted by the worm-like chain model (see Appendix A). This indicates that here, the unfolded polypeptide is compacted more than what can be explained by entropic fluctuations of the polymer. A possible explanation lies in the formation of secondary structure (α helices) or condensation of (parts of) the polypeptide chain due to hydrophobic interactions between nearby amino acids. The similarity between stretch and relax curves suggests that this is a reversible process; no hysteresis can be observed. We observed similar features in the single-MBP measurements. Close examination of Figure 3.14 (i. e., in the absence of SecB) shows similar features, showing that this effect is not SecB-specific. Comparative analysis should be performed to show whether this extra compaction is enhanced or attenuated by the presence of SecB.

3.4 Discussion

We have used optical tweezers to study the effect of *E. coli* chaperone protein SecB on the forced unfolding and refolding of a protein, the maltose-binding protein (MBP). In the unfolding of MBP, we observed unfolding intermediates. We employed steered molecular dynamics (SMD) simulations to find an explanation for one of these intermediates. After the forced unfolding of a protein, it could repeatedly be refolded by decreasing the force exerted on C and N termini. After adding SecB, this refolding was quenched, a result that is consistent with previous bulk experiments.

In this section, we will further discuss our results. We will relate our unfolding experiments to previous single-molecule unfolding experiments performed on other proteins. Furthermore, we will discuss our results on the effect of SecB and will discuss the implications on protein translocation and on protein (un)folding.

Protein [ref.]	F_{unfold} (pN)
MBP	25
Tenascin [78]	47
Spectrin [79]	22
Ribonuclease H [9]	17

Table 3.1: Comparison of unfolding forces for several proteins, extrapolated to a pulling rate of 7 pN/s.

3.4.1 Unfolding forces

In our MBP-unfolding experiments in the absence of SecB, we found an average value of ~25 pN ± 8.6 pN for the unfolding force of MBP, at an unfolding rate of 7 pN/s. This force was compared to the unfolding force of three other proteins. The results are summarized in Table 3.1. For tenascin and spectrin, forces were measured using atomic force microscopy (AFM); for ribonuclease H, an optical tweezers setup similar to ours was used. The published unfolding forces were extrapolated to a pulling rate of 7 pN/s using the relation $F \propto \log v_F$ [80] where F is the unfolding force and v_F is the pulling rate in pN/s. It can be seen that the unfolding force for MBP lies in the same range as the other unfolding forces summarized in Table 3.1.

In bulk unfolding studies using chemical denaturation, the folding stability of a protein is expressed in the free energy difference $\Delta G_{\text{D}\to\text{N}}$ between the denatured state and the native state. Beena et al. [60] found for MBP a $\Delta G_{\text{D}\to\text{N}}$ equal to −37.2 kJ/mol at room temperature using guanidinium chloride. This corresponds to $-15.0\ k_{\text{B}}T$ at room temperature. To directly compare this value to our experiments, we considered the thermodynamics of an unfolding event as we observe it in our measurements.

Figure 3.23a shows a schematic representation of the model that was used in this analysis. The microsphere on the right is held by an optical trap. The total extension x_{tot} is increased by moving the micropipette (not shown) that holds the left microsphere (r→1). As a result, the extension x of the DNA/protein construct increases and x_{trap} increases, resulting in a higher force exerted on the construct. If the force F is high enough, the protein will unfold (1→2). Figure 3.23b shows a force–extension curve $F(x)$ with a hypothetical unfolding event 1→2. In this graph, states 1 and 2 are as indicated in Figure 3.23a. During the unfolding event, the trapped microsphere moves to a position that is closer to the center of the optical trap potential well. The decrease in potential energy of the trapped microsphere is converted to work performed on the trapped construct (DNA+protein). The work W^{tot} performed by the microsphere is equal to:

$$W^{\text{tot}} = \int_{x_1}^{x_2} F \mathrm{d}x = \frac{1}{2}(x_2 - x_1)(F_2 + F_1), \tag{3.1}$$

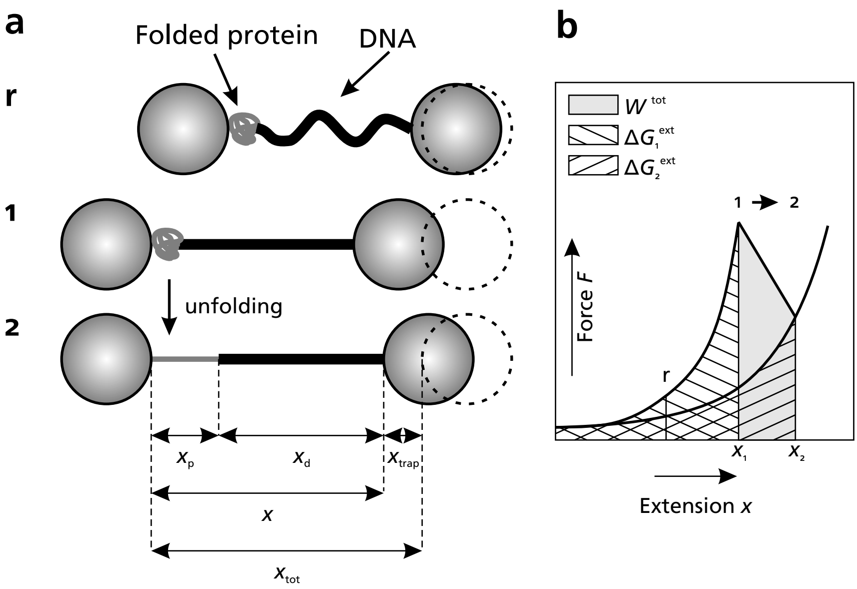

Figure 3.23: Schematic view of all the parameters used in the energy analysis that was performed to study the MBP-SecB binding mechanism. (a) Experimental configuration immediately before (1) and after (2) an unfolding event. The micropipette microsphere is shown on the left, the trapped microsphere is shown on the right, with the position of the trap microsphere at zero force indicated as an interrupted circle. 'r' shows the relaxed conformation of the construct. (b) Schematic force–extension curve showing an unfolding event and showing the work W_{total} that is returned to the machine in an unfolding event.

which is graphically equivalent to the gray area indicated in Figure 3.23b.

This work is put in denaturing the protein and in the subsequent extension of the DNA/polypeptide tether from x_1 to x_2. Hence:

$$W^{\text{tot}} = W^{\text{u}} + W^{\text{ext}}, \tag{3.2}$$

with W^{u} equal to the work needed to denature the protein and W^{ext} equal to the work needed for the subsequent extension of the polypeptide and the DNA from a cumulative extension x equal to x_1 to an extension of x_2.

At the pulling rate that was used in our experiments, W^{ext} is approximately reversible (i. e., the work required to extend the DNA/polypeptide construct from x_1 to x_2 equals the work performed by the construct on the trapped microsphere when relaxing the construct over the same distance.). It can be calculated as follows:

$$W^{\text{ext}} = \Delta G_2^{\text{ext}} - \Delta G_1^{\text{ext}}, \tag{3.3}$$

with ΔG_2^{ext} equal to the work needed to extend a DNA/polypeptide construct from extension 0 to extension x_2 and ΔG_1^{ext} the work required to extend the DNA linker from 0 to x_1, respectively. Both $\Delta G_2^{\mathrm{ext}}$ and $\Delta G_1^{\mathrm{ext}}$ are indicated in Figure 3.23b. They can be calculated by numerically integrating appropriate WLC force–extension relations (see Appendix A).

The unfolding work W^{u} can be expressed in terms of a reversible part $W_{\mathrm{rev}}^{\mathrm{u}}$ and a dissipative part $W_{\mathrm{dis}}^{\mathrm{u}}$:

$$W^{\mathrm{u}} = W_{\mathrm{rev}}^{\mathrm{u}} + W_{\mathrm{dis}}^{\mathrm{u}}. \tag{3.4}$$

In this equation, the reversible part $W_{\mathrm{rev}}^{\mathrm{u}}$ resembles the free energy difference between the native and the denatured state $\Delta G_{\mathrm{N}\to\mathrm{D}}$, as determined by bulk reactions. The second law of thermodynamics states that the average dissipative work $\langle W_{\mathrm{dis}}^{\mathrm{u}} \rangle \geq 0$, but note that in rare events, $W_{\mathrm{dis}}^{\mathrm{u}}$ can be smaller than 0, i. e., when unfolding is partially driven by energy gained from the thermal bath.

Without any force applied, the unfolding rate of MBP is very low ($k_{\mathrm{unfolding}} = 0.003\,\mathrm{s}^{-1}$ [60]. In our experiments, we observe unfolding in seconds, indicating that we unfold a protein faster than its internal dynamics. Hence, we expect dissipative effects. Let us now assume an experiment with an infinitesimally small pulling rate v_F. Now, we expect a $W_{\mathrm{dis}}^{\mathrm{u}}$ that can be close to zero. Without dissipative effects, Eq. 3.2 reduces to:

$$W^{\mathrm{tot}} = W_{\mathrm{rev}}^{\mathrm{u}} + W^{\mathrm{ext}}. \tag{3.5}$$

Hence:

$$W^{\mathrm{tot}} - W^{\mathrm{ext}} \approx \Delta G_{\mathrm{D}\to\mathrm{N}}. \tag{3.6}$$

For a quantitative analysis of these relations, we calculated energies W^{tot} and W^{ext} for an unfolding event at a given value of the experimental parameter x_{tot}. First we calculated both the force F and all the parameters x that are shown in Figure 3.23a, as a function of x_{tot}, using (see Figure 3.23a):

$$x_{\mathrm{d},1} + x_{\mathrm{trap},1} = x_{\mathrm{d},2} + x_{\mathrm{p},2} + x_{\mathrm{trap},2} = x_{\mathrm{tot}}, \tag{3.7}$$

with x_{d}, x_{trap}, x_{p} and x_{tot} as indicated in Figure 3.23a, subscripts 1 and 2 denoting the folded and the unfolded state of the system, respectively, and force–extension relations (see Appendix A):

$$\frac{x_{\mathrm{d}}}{L_{\mathrm{d}}} = 1 - \frac{1}{2}\left(\frac{k_{\mathrm{B}}T}{F_{\mathrm{d}}p_{\mathrm{d}}}\right)^{1/2} + \frac{F_{\mathrm{d}}}{S_{\mathrm{d}}}, \tag{3.8}$$

$$\frac{F_{\mathrm{p}}p_{\mathrm{p}}}{k_{\mathrm{B}}T} = \frac{1}{4}\left(1 - \frac{x_{\mathrm{p}}}{L_{\mathrm{p}}}\right)^{-2} - \frac{1}{4} + \frac{x_{\mathrm{p}}}{L_{\mathrm{p}}}, \tag{3.9}$$

$$F_{\mathrm{trap}} = k_{\mathrm{trap}} \cdot x_{\mathrm{trap}}, \tag{3.10}$$

$$F_{\mathrm{d}} = F_{\mathrm{p}} = F_{\mathrm{trap}} = F, \tag{3.11}$$

with contour lengths $L_d = 920\,\mathrm{nm}$ and $L_p = 120\,\mathrm{nm}$, persistence lengths $p_d = 53\,\mathrm{nm}$ and $p_d = 1\,\mathrm{nm}$, temperature $T = 298\,\mathrm{K}$, DNA elastic stretch modulus $S_{\mathrm{d}} = 1200\,\mathrm{pN}$ and trap stiffness $k_{\mathrm{trap}} = 150\,\mathrm{pN/s}$.

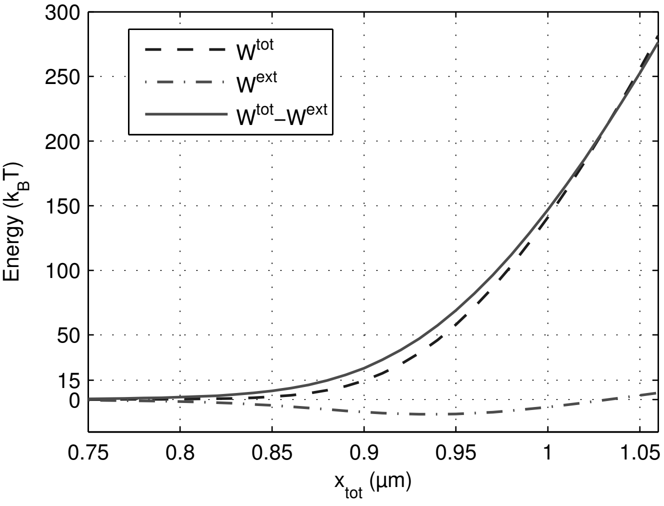

Figure 3.24: Calculated thermodynamic parameters of the experiment sketched in Figure 3.23. The work W^{tot} performed on the tethered construct by the trapped microsphere is shown as a function of x_{tot}. Furthermore, the work W^{ext} needed to extend the DNA/polypeptide construct from extension x_1 to x_2 is shown. An additional curve $W^{\text{tot}} - W^{\text{ext}}$ is shown.

The energies W^{tot} and W^{ext} could now be calculated using Eq. 3.1 and numerical integration of Eqs 3.8 and 3.9. In Figure 3.24, these energies are shown as a function of x_{tot}, together with their difference, $W^{\text{tot}} - W^{\text{ext}}$. Note that according to Eq. 3.2 this difference equals the total work needed for the unfolding of a protein (i. e., both reversible and dissipative work). $\Delta G_{\text{N}\to\text{D}} = 15.0\,k_{\text{B}}T$ [60] is indicated in the graph as a reference. Note that $W^{\text{ext}} < 0$ for $x_{\text{tot}} < 1.03$ μm. After the unfolding event, the DNA extension has decreased, resulting in an increase of conformational entropy in the DNA that is larger than the decrease of entropy due to extension of the unfolded polypeptide.

At $x_{\text{tot}} = 0.89$ μm, it can be seen that $W^{\text{tot}} - W^{\text{ext}}$ equals $\Delta G_{\text{N}\to\text{D}}$. This is the point where Eq. 3.6 holds, i. e., where the free energy increase due to the denaturation of a protein is fully compensated by a cumulative free energy loss of the DNA/polypeptide construct and the microsphere in the optical trap (and *vice versa*). The system is in equilibrium here. Now, it is interesting to see what the unfolding force would be in such an equilibrium unfolding event. Figure 3.25 shows the relation between $W^{\text{tot}} - W^{\text{ext}}$ and the force F_1 at which an unfolding event will take place. In this graph, it can be seen that in the absence of dissipative effects, the expected unfolding force F_1 equals 3.7 pN, if one assumes a free energy difference $\Delta G_{\text{D}\to\text{N}}$ equal to the value found in bulk experiments ($15.0\,k_{\text{B}}T$). It is clear that this force is considerably smaller than the value we measured in our

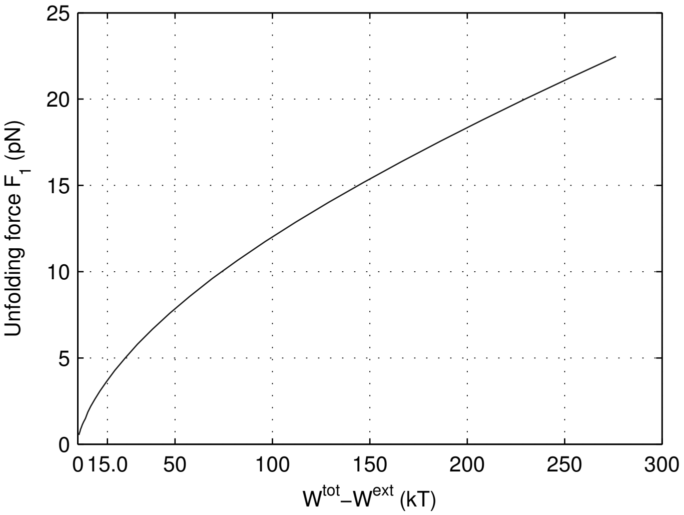

Figure 3.25: The relation between work $W^{\text{tot}} - W^{\text{ext}}$ and the unfolding force F_1 in an unfolding experiment as sketched in Figure 3.23.

experiments (~25 pN). This discrepancy can be explained from the pulling rate that we use in our experiments (~7 pN/s). At this finite pulling rate, we expect a dissipation unfolding term $W^{\text{u}}_{\text{dis}}$ higher than zero. Figure 3.25 shows that at an unfolding force of 20 pN, the difference between total work W^{tot} and the work W^{ext} needed to extend the DNA/polypeptide construct is ~230 $k_{\text{B}}T$. Hence, the total dissipated energy is $W^{\text{tot}} - W^{\text{ext}} - \Delta G_{\text{D}\rightarrow\text{N}} =$ ~215 $k_{\text{B}}T$. This shows that forced protein unfolding is a highly dissipative, non-equilibrium process.

3.4.2 Unfolding intermediates

In our protein unfolding experiments, we observed intermediates in the unfolding of MBP. These were found at different levels of unfolding, but there was one predominant one leading to a polypeptide contour length of 25–30 nm. This unfolding intermediate was remarkably stable: further unfolding of the intermediate occurred only after seconds at pulling forces that were sometimes higher than 30 pN. Our measurements on the 4×MBP construct confirmed the existence of this intermediate. Moreover, we performed measurements that showed that refolding from this intermediate to the native state could occur at a force between 5 and 10 pN.

Surprisingly, from bulk experiments, no unfolding intermediates are known for the unfolding of MBP. The structure of MBP (see Figure 3.4) suggests a two-step unfolding where each of the two lobes on both sides of the maltose-binding cleft unfolds independently. Close inspection of the structure reveals, however, that the polypeptide chain crosses the bridge between the two lobes three times. It is thus unlikely that separate unfolding of these lobes is possible at all.

Unfolding intermediates in single-molecule protein unfolding have been observed before. Dietz and Rief [69] saw short-lived (~1 ms) intermediates in the unfolding of the green fluorescent protein (GFP) using AFM and Cecconi et al. [9] saw an intermediate in the folding and refolding of ribonuclease H that had already been observed previously in bulk studies.

We have performed steered molecular dynamics simulations to find an explanation for the observed intermediate(s). The simulations showed a possible explanation for the predominant unfolding intermediate. The last ~85 C-terminal amino acids (285–370) of MBP mainly fold into a series of α-helices that are partially exposed to the surrounding buffer. In the sequence beyond this point, residues are more buried in the structure and moreover, the structure contains two residues at positions 276 and 283, that have been proven crucial for folding [58]. Possibly, in our unfolding experiments, the surface-exposed α-helices are 'peeled' off in a low-force (~16.5 pN) unfolding event, before the tertiary structure around amino acids 276 and 283 is disrupted, leading to further complete unfolding. The resulting 85 denatured residues would result in an additional contour length of 28 nm, which remarkably well matches the contour length of the predominant intermediate in the optical tweezers studies. Additional SMD simulations will be performed to show that the stability of the MBP structure without amino acids 285–370, is stable enough to explain the intermediate.

In our protein unfolding experiments, we observed features in the relax curves that suggested an additional compaction of the polypeptide at forces below 10 pN. This effect was most prominent for the experiments in which the 4×MBP construct was unfolded. A likely explanation for this effect is the condensation of the polypeptide chain due to interactions between nearby hydrophobic residues, or the early formation of secondary structure.

3.4.3 Binding of SecB to MBP

One of the aims of our experiments was to explore, on a single-molecular level, the molecular mechanism of SecB-preprotein binding. We performed unfolding experiments of MBP in the presence of 0.1 μM SecB. These experiments showed that SecB had no effect on the protein before its complete forced unfolding. The force at which MBP unfolds to the denatured state was similar to the unfolding force in the absence of SecB. This result is consistent with literature. Bulk experiments have shown that SecB has no affinity for native, stably folded polypeptides [67].

After the complete unfolding of a protein, both the stretch and the relax force–extension curve of the DNA/polypeptide construct resembled worm-like chain behavior. No features could be seen in the force–extension curve that would point to the (partial) refolding of the protein. Hence, the effect of SecB was of an all-or-nothing kind: no refolding of the protein could be observed upon decreasing the

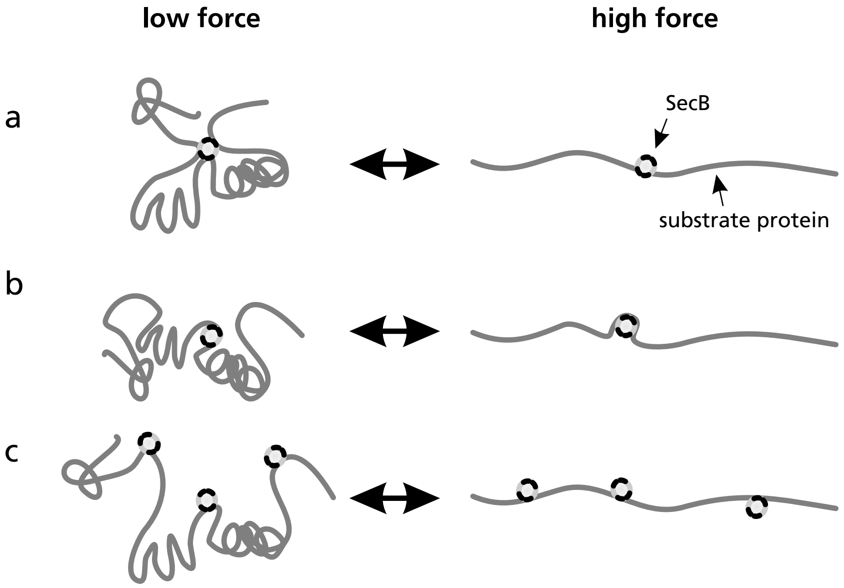

Figure 3.26: Different possible binding mechanisms of mbp to SecB in our stretch-relax experiments. Each of the mechanisms is shown under relaxed (low-force) conditions, and under stretched (high-force) conditions. (a) Binding mechanism with a 1:1 (SecB tetramer : preprotein) stoichiometry with all four binding channels binding to peptides throughout the preprotein sequence. (b) Binding mechanism with a 1:1 stoichiometry with all four preprotein-binding sites of SecB binding locally to the preprotein. (c) Configuration with multiple SecB tetramers per preprotein.

tension exerted on the SecB-bound polypeptide—not even to a folding intermediate.

In our measurements, we also looked for features that would reveal details of the binding geometry of SecB to a preprotein. Our measurements did not show such features. In Figure 3.26, different models for the binding geometry of SecB to a denatured polypeptide are shown schematically. Two of them show a 1:1 stoichiometry of SecB tetramers to polypeptide, with the four putative preprotein-binding sites binding either locally (b) or to sites throughout the preprotein sequence (a). In Figure 3.26c multiple SecB tetramers bind to a single polypeptide. It is not known whether the parts of the polypeptide that are not bound to SecB can form a primordial secondary or tertiary structure, as is shown in Figure 3.26. Our data suggests that if structure is formed, its stability is insignificant.

To extend the polypeptide in the configuration sketched in Figure 3.26a, several preprotein-binding channels have to unbind from the preprotein, before the protein can be fully extended. In our experiments, we looked for the unbinding of the binding channels from the protein as sudden decreases in force, similar to unfolding events. Our measurements do not show such events (see Figs 3.21 and 3.22). We can, however, not exclude the binding mechanism of Figure 3.26a, taking into account the unbinding rate of SecB from MBP, 3 s^{-1} [66]. Unbinding is a rapid process and is expected to happen within the first second of a stretch sweep in our experiments, where it will go unnoticed due to the compliance of the DNA linker at low force. Experiments at a higher pulling rate should be performed to increase the force at which unbinding is expected.

From bulk studies using MBP, it is known that there is a 1:1 stoichiometry in the binding of SecB tetramers to MBP [51]. More than in the condensed, guanidinium-chloride-denatured state of a polypeptide that is used in these bulk studies, the extended denatured configuration of the MBP polypeptide in our experiments may allow for the binding of multiple SecB tetramers, leading to a mechanism as sketched in Figure 3.26c. Likely binding sites for SecB along the MBP amino acid sequence are indicated in Figure 3.5. To ensure a 1:1 binding of SecB to MBP, unfolding experiments should be performed with an MBP construct that has been bound to SecB prior to tethering the construct between two microspheres, in a bulk reaction in denaturing conditions.

3.4.4 Protein translocation context

Here, we will discuss our experiments in the broader perspective of protein translocation. In our experiments on the forced unfolding of MBP, we found an unfolding force of ~25 pN at a pulling rate of 7 pN/s, a speed that is comparable to the rate of translocation by the Sec translocase.

Our experiments suggest that in the translocation of a polypeptide by ATPase SecA in the presence of chaperone SecB, only a small part of the energy from ATP hydrolysis is used for the unraveling or the unfolding of a preprotein. We performed experiments where a SecB-bound polypeptide was slowly extended using the optical trap. This experiment can be directly compared with the initiation of protein translocation by the Sec translocase. After a SecB-bound preprotein has arrived at the Sec translocase, the preprotein is transferred to ATPase SecA and translocated by ~40 aa upon binding of SecB to SecA and a subsequent ATP hydrolysis by SecA [21]. The free energy from hydrolysis of a single molecule of ATP is estimated to be 50.2 kJ/mol or ~19 $k_\mathrm{B}T$ *in vivo* at 37°C. A central question in protein translocation has been whether this energy is coupled to a 'power stroke' by SecA that drives the unfolding of a preprotein and its translocation by 40 aa. We observed that the force–extension curve of a SecB-bound polypeptide resembles that of an entropy-dominated random polypeptide coil. This shows that to extend a preprotein in a translocation-competent state, only entropic fluctuations have to be pulled out. The free energy that is released by hydrolysis of ATP by SecA is considerably larger than the free energy required to extend a random polypeptide coil by the distance corresponding to a polypeptide of 40 aa (estimated to be ~0.9 $k_\mathrm{B}T$ using an analysis similar to that used in §3.4.1). This strongly suggests that the free energy from ATP hydrolysis is mainly used for other purposes than the unfolding of the preprotein. Here, one can think of, e. g., the induction of conformational changes in the translocase pore. Single-molecule experiments on protein translocation by the Sec translocase, as suggested in Chapter 2 could shed more light on the thermodynamics of SecA hydrolysis.

Previously, Wilcox et al. [81] and Sato et al. [82] performed afm protein unfolding experiments on mutants of *E. coli* dihydrofolate reductase (dhfr) and the I27 domain of titin, respectively, and studied the relation between the unfolding force and the rate of mitochondrial import of a protein. Mitochondrial import is a process that is comparable to protein translocation by the Sec translocase. It was found that the time needed to import a protein, directly scales with its resistance to mechanical unfolding. Nouwen [83] showed that multiple titin I27 domains—with an unfolding force of ~229 pN at a pulling rate of 135,000 pN/s [81]—can be efficiently translocated by the *E. coli* Sec translocase, when fused with their N terminus to the C terminus of proOmpA (a protein that can readily be translocated; see Chapter 2), even in the absence of SecB.

Remarkably, translocation of mbp—with a considerably lower unfolding force, ~25 pN at a pulling rate of ~7 pN/s—does require SecB to keep the protein in a translocation-competent state. This observation can be explained from the fact that in the Nouwen experiments, translocation of the I27 subunits is preceded by translocation of proOmpA—a membrane protein that cannot fold in its native state before translocation. Moreover, the structure of mbp near the N terminus is very strongly folded; it contains the four residues that have been proven crucial for folding (Val8, Gly19, Ala276 and Tyr283 [58]). De Cock and Randall [65] even suggested that this structural element could form if mbp is in complex with SecB. Hence, this structure is not easily disrupted, when the pulling is performed only from the N terminus, as is the case in translocation. Our high-pulling-rate smd simulations confirm this notion: to disrupt the interactions between the N-terminal β-strand and the residues in its surroundings, forces are required that are several times higher than those needed to remove the first C-terminal α-helix (see Figure 3.19).

Hence, our study shows the importance of the structure of a protein adjacent to the signal sequence to its translocation efficiency. Translocation experiments using a protein construct with the N terminus of mbp cloned to the C terminus of proOmpA could further show the importance of the N terminal structure in translocation by the Sec translocase. Alternatively, one could use circular permutants [84] of mbp that have their N terminus at a position with less structural rigidity (See Wilcox et al. [81] for afm protein unfolding studies using circular permutants).

4

Optical tweezers measurements on dsDNA-packaging by bacteriophage φ29

We have used optical tweezers to study the packaging of double-stranded DNA by bacteriophage φ29. We will show the results of these experiments and we will present the synthesis of a DNA construct that was required for these experiments.

4.1 Introduction

This chapter will describe the different optical tweezers experiments we performed on the packaging of dsDNA by bacteriophage φ29. Bacteriophages are viruses that have bacteria as a host. For bacteriophage φ29, this is *Bacillus subtilis*. Figure 4.1 shows a schematic representation of a bacterial cell and bacteriophages in different stages of their life cycle. First, a bacteriophage infects its host by injecting its genetic material. For phage φ29, this is double-stranded DNA with 19,285 base pairs. An important feature of the φ29 DNA is the presence of terminal proteins called gp3 at the two 5′ termini. After infection, the host's transcription and translation machinery is used to express the genes on the bacteriophage DNA. Eventually, the bacteriophage DNA is replicated, a process in which the gp3 terminal proteins play an important role. Next, new bacteriophage shells or capsids are formed, that are called *proheads* before they have developed into mature viruses. Before maturation, the proheads have to be filled with DNA in a process called *packaging*. After packaging, the proheads can further develop into mature bacteriophages. After maturation, the host cell is lysed, and mature bacteriophages are released to the surrounding medium, where they can infect new hosts.

For bacteriophage φ29, packaging is driven by a DNA-packaging motor that lies at a unique portal vertex of the prohead. The motor contains: (I) the head-tail connector (a dodecamer of phage protein gp10), (II) the portion of the prohead that surrounds the connector; (III) a ring of prohead RNAs (pRNA), which surrounds the protruding narrow end of the connector; and (IV) a multimer of phage protein gp16, an ATPase that first binds DNA-gp3 and then assembles onto the connector/pRNA

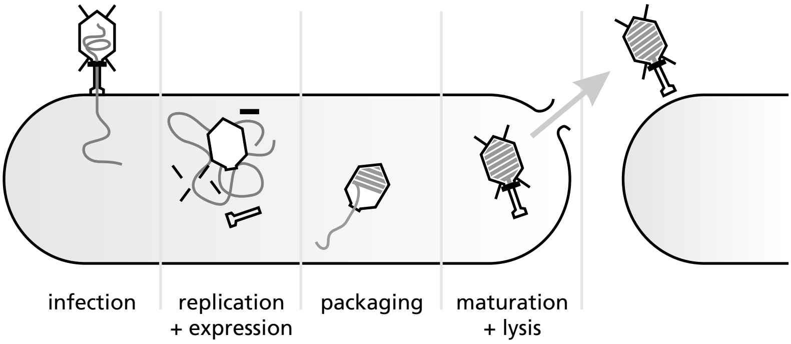

Figure 4.1: The bacteriophage life cycle. Different stages in the bacteriophage life cycle are shown, from infection of a host cell to cell lysis.

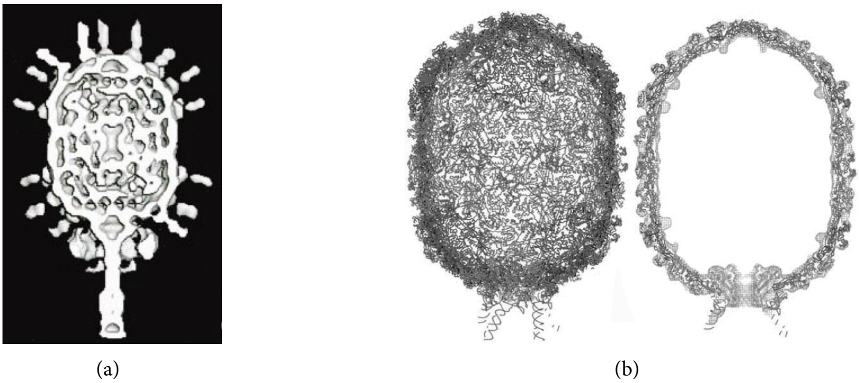
(a)
(b)

Figure 4.2: Different representations of the bacteriophage ϕ29 capsid. (a) cross section of a mature ϕ29 bacteriophage. Cryo-EM picture adapted from Tao et al. [87]. (b) pseudo-atomic structure of an empty ϕ29 prohead, adapted from Morais et al. [88]

complex prior to packaging. For more information about bacteriophage ϕ29 and its packaging mechanism, see review articles by Meijer et al. [85] and Grimes et al. [86]. Figure 4.2a shows a cross section of a mature ϕ29 bacteriophage [87]. In this picture, also the bacteriophage tail and the head fiber proteins can be seen. The tightly packed DNA can also be observed inside the bacteriophage head. Figure 4.2b shows a pseudo-atomic structure of an empty ϕ29 prohead [88], with the connector and the pRNA in the bottom.

During packaging, the 6.6 μm-long gp3-DNA is compressed into a cavity of 42 nm in width and 54 nm in length. Large entropic, electrostatic and bending energies must be overcome to package the highly negatively-charged DNA to near-crystalline density. Figure 4.2a clearly shows the density of the DNA inside the

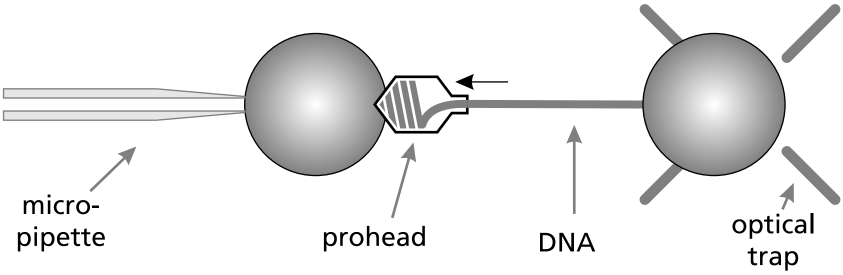

Figure 4.3: The experimental configuration used in the optical tweezers experiments performed by Smith et al. [5] and also in the experiments shown in this chapter. The prohead was bound to a microsphere using anti-ϕ29 antibodies and the DNA was bound to the optically-trapped microsphere using biotin-streptavidin interactions.

bacteriophage capsid. Smith et al. [5] used optical tweezers to measure the packaging of individual ϕ29 complexes in real time. They showed that the packaging motor can exert forces on the DNA of as high as 57 pN during packaging. When the capsid is >50% full, an internal pressure as high as ~60 atm builds up due to the confinement of the DNA. This pressure might drive the ejection of DNA during infection of a new host cell [89, 90].

Figure 4.3 shows the experimental configuration that Smith et al. [5] used in their optical tweezers measurements. A DNA-packaging prohead was bound to a polystyrene microsphere on a micropipette. The free end of the DNA was bound to another polystyrene microsphere that was held by an optical trap. Because of the packaging, the DNA shortens and the optically-trapped microsphere is slowly pulled out of the optical trap. By keeping the force on the DNA constant by correcting the micropipette position using a piezo stage, the packaging can be followed in time. Figure 4.4a shows two examples of these packaging measurements, clearly showing the decrease of the DNA tether length with time. As the bacteriophage fills up, the packaging speed decreases. Figure 4.4b shows the packaging speed as a function of the DNA tether length, relative to the ϕ29 19.3-kbp genome. It can be seen that until ~50% of the ϕ29 genome has been packaged, the packaging speed remains constant. After 50%, the packaging speed goes down to zero. At ~110%, packaging has stopped (percentages higher than 100% could be reached, because Smith et al. used a DNA construct larger than the ϕ29 genome).

We have performed similar optical-tweezers experiments to study packaging in this high-density regime of packaging. Our aim was to investigate the role of both electrostatic repulsion and bending forces in the DNA on the development of the packaging speed as the capsid is filling up. First, to tune the electrostatic repulsion between DNA strands, we wanted to add spermine [91], a tetravalent cation, to the packaging reaction. Of polyvalent cations, such as spermine, it is known that they can induce condensation of DNA in toroidal condensates [92, 93], as shown in Figure 4.5. In a spermine condensate, the positively charged spermine

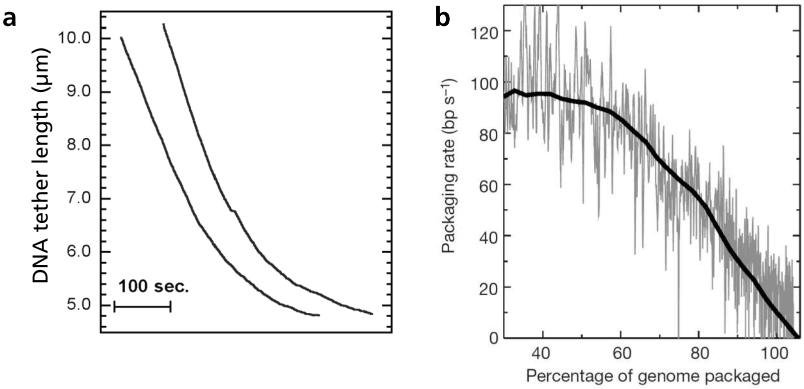

Figure 4.4: Measurements performed by Smith et al. [5] (a) Two measurements showing the decrease of the length of packaged DNA as a function of time. (b) DNA packaging speed as a function of the length of the packaged DNA, relative to the ϕ29 19.3-kbp genome.

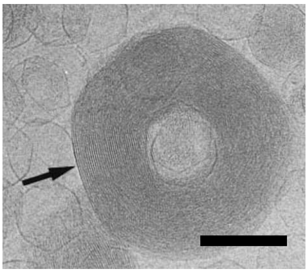

Figure 4.5: Toroidal DNA condensate induced by spermine, adapted from Lambert et al. [92]. This picture shows a unilamellar proteoliposome, into which numerous T5 bacteriophages have injected their 120-kbp DNA via a membrane-incorporated receptor. The spermine inside the liposome caused the DNA to form toroidal condensates that can be 200 nm in diameter. The scale bar indicates 100 nm.

cations form 'ion bridges' between neighboring DNA strands, thus compensating for the negative charges on the DNA. Evilevitch et al. [90] showed that ejection of dsDNA by bacteriophages—the inverse process of packaging—can be inhibited by adding 1 mM spermine chloride. Conversely, in the presence of spermine cations, packaging could be easier. In microorganisms, notably gram-negative bacteria, large concentrations of polyamines such as spermine can be found. Various *E. coli* bacteriophages contain high concentrations of polyamines. To find the spermine concentrations at which DNA condenses under our conditions, we performed DNA extension experiments using optical tweezers. These were in accordance with literature [94].

To study the role of the bending of DNA on the pressure inside the bacteriophage capsid as it fills up, we aimed to introduce nicks, or single-stranded breaks, in the dsDNA that is being packaged. These nicks might change the structure of the coiled DNA strands such that it, for example, might be easier to wind up the DNA in a cavity with a diameter equal to its persistence length. Moll and Guo [95] performed bulk packaging experiments with bacteriophage ϕ29 using nicked DNA. It was found

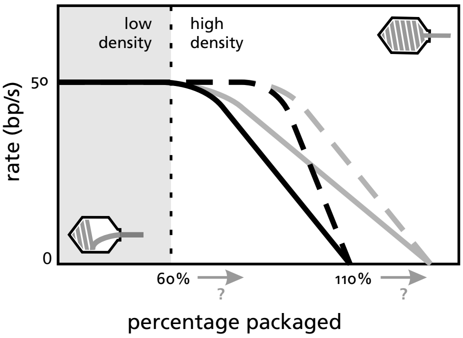

Figure 4.6: Possible effects of spermine and nicks in the DNA on the packaging speed throughout the packaging process. Possible effects are indicated with a question mark. See the text.

that the presence of nicks does not alter the bulk packaging properties. This can be understood since without applied stress, the structure of nicked DNA is similar to that of normal DNA [96]. If the DNA is under stress, however, e. g., by exerting a force using optical tweezers or due to confinement in a bacteriophage capsid, this might be not the case.

We were interested in the effect of either spermine or nicks on the high-density regime of packaging (see Figure 4.6). Possible effects are indicated in this cartoon (cf. Figure 4.4b): it could be that DNA can be packaged to a higher density inside the capsid, so that more than 110% of the ϕ29 genome can be packaged. Another effect could be that the amount of DNA that can be packaged before the packaging speed goes down (normally at 50%) is increased.

For measurements in this high-density regime of packaging, a DNA construct had to be synthesized with the following three properties: it should be packageable by bacteriophage ϕ29; it should be at least 10% longer than the ϕ29 genome and it should contain a biotin at one of the two ends. To make this construct, it was necessary to extend ϕ29 DNA. The method that was used by Smith et al. was not suitable to us, for reasons that will be explained. Therefore, a novel method was developed of making a long ϕ29 DNA construct. This construction method featured digestion using non-palindromic restriction enzymes and the use of linker oligonuclotides to extend ϕ29 DNA using phage T7 DNA. Construction of this DNA was not straightforward and will be described in detail in this chapter.

Because of reasons that will be given in this chapter, the concentration of our long DNA sample was rather low. We will present some recommendations for an increased success of the synthesis of long DNA in the future. Single-molecule packaging experiments have been performed using this long DNA construct, but because priority had been given to a different project while performing the experiments, we could not address the questions asked in the above text. We did use an alternative short DNA construct to study the effect of spermine and nicks on packaging in the low-density regime. Here, the measurements did not show that these had a detectable effect on the packaging behavior.

4.2 DNA constructs

For our optical trapping experiments on DNA-packaging by bacteriophage ϕ29, different DNA constructs were required. For the experiments where the high density packaging regime was of interest, i. e., where the proheads were >50% filled with DNA, a DNA construct had to be manufactured that could fill the proheads completely. This implies a number of base pairs equal to 110% of the ϕ29 genome (19,285 base pairs). To achieve this, the ϕ29 DNA somehow had to be extended. In the experiments where the low density packaging regime was of interest, a simpler, shorter DNA construct was sufficient. In this section, the synthesis of both the short and the long DNA construct will be described. Synthesis of the short DNA construct was successful. Also the longer DNA construct was synthesized successfully, however with less efficiency. Both constructs could be successfully applied in single-molecule DNA packaging experiments.

4.2.1 Construction of a short DNA construct

In some of the performed optical trapping experiments, a ϕ29 DNA construct could be used of a shorter length than the ϕ29 genome. For these experiments, a construct was used consisting of NcoI-digested ϕ29 DNA, of which the resulting cohesive ends were biotinylated by Klenow filling. In this procedure, 5′ overhangs resulting from restriction are filled with free nucleotides by the Klenow fragment of DNA polymerase I. Here, biotinylated nucleotides were added to provide the DNA construct with covalently bound biotin groups. This protocol yields a sample with two biotinylated DNA fragments (15.0 kbp and 4.3 kbp) of which the larger left end is preferentially packaged by proheads.

The exact protocol was as follows: 15 μl of a 0.5 μg/ml ϕ29 DNA(DNA-gp3) stock solution (kindly provided by Shelley Grimes of the University of Minnesota). was dialyzed for 40 minutes against 50 ml 20 mM Tris-HCl, pH 7.6 to exchange buffers and to remove CsCl from the stock solution. This was done by placing a ∅25 mm membrane filter with 25-nm pores (Millipore) on top of the buffer, and carefully placing the DNA-gp3 solution on top. Next, the DNA was digested using 30 units of NcoI (New England Biolabs) in 30 μl of NEBuffer 4 for 90 minutes at 37°C. Next, dGTP and dTTP (New England Biolabs) were added until an end concentration of 61 μM, and biotin-14-dATP and biotin-14-dCTP (Invitrogen) were added until an end concentration of 12 μM. To start Klenow filling, 2.5 units of Klenow Fragment (3′→5′ exo$^-$ mutant; New England Biolabs) was added and the sample was incubated for 15 minutes at 37°C. Next, EDTA was added until an end concentration of 20 mM to terminate the reaction and the sample was dialyzed twice for 30 minutes as described before to remove free biotinylated nucleotides. The DNA sample, with a concentration of 250 ng/μl, was stored at 4°C.

To examine the biotinylation efficiency, the binding efficiency of the biotinylated fragments to streptavidin microspheres was tested on a gel. 10 μl of a 0.5% streptavidin-microsphere suspension (Spherotech) was washed twice with 100 μl

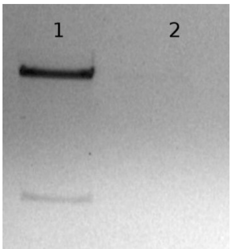

Figure 4.7: The efficiency of biotinylation by Klenow filling was tested by incubation of biotinylated, NcoI-digested DNA with streptavidin-polystyrene microspheres. After 1 hour, microspheres were spun down and the supernatant was put on gel (lane 2). The input is shown on lane 1.

0.5× TMS (25 mM Tris-HCl, pH 7.8; 5 mM $MgCl_2$; 50 mM NaCl) and resuspended in 6 µl 0.5× TMS. 1 µl of the biotinylated DNA sample was diluted in 10 µl of 0.5× TMS. 4 µl of this diluted sample was added to the washed streptavidin microspheres and was incubated for 1 hour at room temperature under constant rotation. Next, the microspheres were spun down using a table centrifuge at full speed and the supernatant was run on a 0.5% agarose gel and compared to 4 µl of the unbound diluted DNA sample. Before loading the DNA on gel, the gp3 terminal protein was digested by adding 0.5 µl of proteinase K (Qiagen) and a 20 minutes incubation at 65°C. The results in Figure 4.7 show that biotinylation was 100% efficient, and moreover, that biotinylated ϕ29 fragments can efficiently be bound to streptavidin-polystyrene microspheres. A control experiment (not shown) showed that the binding of the ϕ29 DNA to the microspheres is not caused by non-specific interactions between DNA and the polystyrene surface.

4.2.2 Construction of a long DNA construct

For the optical tweezers experiments in which packaging in the 'full' regime was of interest, a packageable DNA-construct had to be constructed that was at least ten percent longer than the ϕ29 genome, and that would allow the binding of a polystyrene microsphere for optical trapping purposes. Hence, it should contain at least 21,300 base pairs, and to make the construct packageable, it should contain the left end of ϕ29 DNA(ϕ29-L) with a covalently bound gp3 protein. Furthermore, a biotin was needed at the other end of the DNA construct for binding to a streptavidin microsphere.

In their optical trapping experiments on packaging by bacteriophage ϕ29, Smith et al. [5] used a construct consisting of the left end of NcoI-digested ϕ29 DNA, ligated to a biotinylated fragment of phage λ DNA, yielding a construct of 34.4 kbp. For several reasons, this method was not suitable to us. First of all, Smith et al. used a sucrose gradient in an ultracentrifuge to separate the ϕ29-L fragment from the ϕ29-R fragment before ligation to the λ DNA fragment. In our lab, we could not perform this technique. A second, more general, disadvantage of the method used by Smith et al. was the *palindromic* restriction enzyme that was used, NcoI. This enzyme leaves two identical cohesive ends after restriction. Hence, in the final ligation of ϕ29 to λ DNA fragments, also ligation of ϕ29 fragments to other ϕ29

	Palindromic		Non-palindromic
BglII	•••A⌊GATCT•••	SfiI	•••GGCCACAA⌋CGGCC•••
	•••TCTAG⌉A•••		•••CCGGT⌈GTTGCCGG•••

Figure 4.8: An example of a palindromic restriction enzyme, BglII, yielding two identical cohesive ends (`GATC`), and an example of a non-palindromic restriction enzyme, SfiI that yields two non-identical cohesive ends.

fragments can occur. This produces side products that can interfere with the final experiments, notably the ϕ29-L–ϕ29-L construct.

To overcome these problems, we developed a novel protocol of creating a long, packageable construct, with the following features:

Non-palindromic restriction sites To obtain the ϕ29-L fragment, we performed a restriction reaction on ϕ29 DNA using non-palindromic restriction enzymes. A restriction reaction with these enzymes results in non-identical cohesive ends (see, e. g., the sequence for restriction site SfiI in Figure 4.8), hence no self-ligation of ϕ29-L fragments could occur.

T7 DNA To extend the ϕ29-L fragment, we used commercially available bacteriophage-T7 DNA. This DNA was long enough for our purposes (39.9 kbp; cf. phage-λ DNA: 48.5 kbp). Moreover, it contained several non-palindromic restriction sites that we could use in our procedures.

Linker dsDNA oligonucleotides After restriction of the ϕ29 DNA, the ϕ29-L fragment could not be separated from the ϕ29-R fragment using a sucrose gradient. Neither could we use agarose gel extraction protocols, because DNA with a covalently bound gp3 terminal protein does not migrate through agarose gels. Therefore, we specifically ligated dsDNA oligonucleotides (34-bp) to the ϕ29-L fragments that alter the cohesive end such that rebinding of ϕ29-R becomes impossible. The oligonucleotides were designed such that the new cohesive end can ligate to the T7 fragment. A large excess of oligonucleotides was added to the ϕ29-L fragments to ensure that virtually none of the fragments could religate to the ϕ29-R fragment. Note that prior to the final ligation of ϕ29-L/oligonucleotide fragments to T7 DNA, excess free oligonucleotides should be removed.

Klenow filling To biotinylate our DNA construct, we used the Klenow fragment of DNA polymerase I as described before.

In Figure 4.9, a schematic representation of our DNA extension strategy is shown. This figure shows schematically (1) how ϕ29 DNA is digested using non-palindromic restriction enzyme BglI to obtain the 8.4-kbp ϕ29-L fragment; (2) how oligonucleotides are bound to the ϕ29-L BglI cohesive ends; (3) how T7 DNA is digested at palindromic restriction site BglII and subsequently biotinylated by

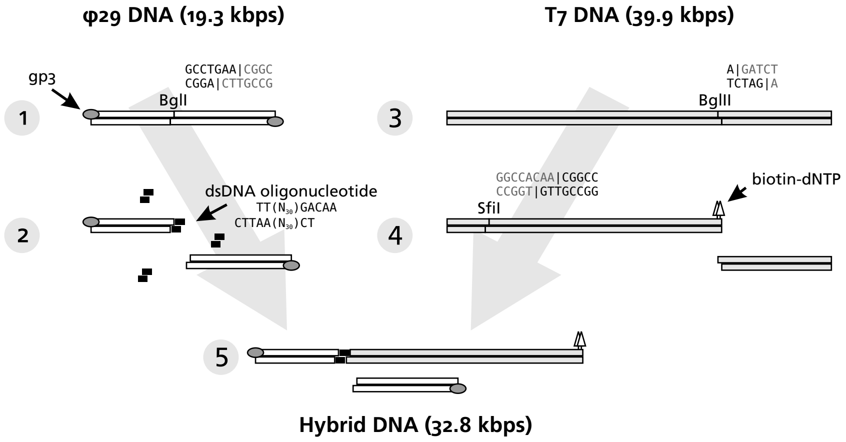

Figure 4.9: The construction of the ϕ29-T7 hybrid DNA construct shown schematically: (1) ϕ29 DNA with terminal protein gp3 covalently linked to the 5′ ends. (2) The DNA is restricted using restriction enzyme BglI, and a 34-bp long dsDNA oligonucleotide is ligated to the resulting left end. The overhang resulting from the BglI restriction is non-palindromic, preventing ligation of the oligonucleotide to the right end. (3) Bacteriophage T7 DNA is used to extend the ϕ29 DNA. T7 DNA is restricted using restriction enzyme BglII and the resulting 5′ overhangs are biotinylated by Klenow filling. (4) Next, the DNA is digested using restriction enzyme SfiI. Before the final ligation, resulting in the construct shown in (5), free oligonucleotides are removed from the ϕ29 DNA sample and the 24-kbp long fragment resulting from the SfiI-restriction of T7 DNA is purified using agarose gel extraction. In the final ligation, self-ligation of the fragments does not occur because of the non-palindromic overhangs. For details concerning all different substeps, see the text.

Klenow filling; (4) how T7 is further digested using non-palindromic restriction enzyme SfiI; and (5) how, finally, the ϕ29-L fragment and the purified 24.4-kbp T7 fragment are ligated to obtain the wanted 32.8-kbp packageable DNA construct.

In the rest of this section, we will describe all the different steps that are shown in Figure 4.9 in greater detail. At the end of this section, we will show that our strategy can indeed be used to obtain a DNA construct that can be used in optical trapping experiments on DNA packaging by ϕ29 in the high-density regime of packaging.

4.2.3 Removal of dsDNA oligonucleotides

In step 2 of Figure 4.9, oligonucleotides are ligated to the ϕ29-L fragment. Subsequently, all free, unligated oligonucleotides have to be removed from the ϕ29 DNA mixture before the final ligation step. To separate the free oligonucleotides from the ϕ29 fragments, one can think of different methods. Methods that use the affinity of DNA to silica membranes, such as, e. g., the Qiagen Qiaquick PCR purification kit, cannot be used, since the chaotropic salts in the used elution buffer denature the gp3 terminal protein. We have tried two alternative methods:

Filtration By using a Millipore centrifugal filter, with its nominal molecular weight limit (NMWL) between the molecular weight of an oligonucleotide and that of the ϕ29 fragments, oligonucleotides will flow through the filter, and longer ϕ29 fragments will remain on top and can be recovered.

PEG precipitation In the presence of ~10% polyethylene glycol-8000 (PEG-8000), fragments >100 bp will precipitate and oligonucleotides can be removed by spinning down the precipitate and removing the supernatant [97].

The applicability of both methods was tested using a commercially available DNA ladder with DNA fragments of 50–1000 bp (Fermentas O'RangeRuler 50bp). Dyes and glycerol were removed from this DNA ladder using a Qiaquick spin column before each of the tests. These tests showed that both methods can efficiently separate 34-bp oligonucleotides from significantly larger DNA fragments. With the PEG precipitation method, higher recovery efficiencies for large DNA fragments could be obtained, making it a more useful method for our purpose.

For filtration, Microcon YM-100 centrifugal filters (Millipore) were used with a NMWL of 100 kDa. For this test, 10 μl of the DNA ladder was used. The filtration protocol was performed as described in the manual, using 1× T4 DNA ligase buffer (New England Biolabs), two 15–20 minutes filtration spins at 500×*g*, and a 3 minute recovery spin with inverted membrane at 1000×*g*, yielding 5–15 μl of DNA solution. Figure 4.10 shows a 2% agarose gel with the results of two *in duplo* tests with filtering the O'Rangeruler with the Microcon filters. For comparison, 2.5 μl of the DNA ladder was loaded on the leftmost lane. For both tests, no 50-bp bands can be seen. The 100-bp band is invisible for test 'out1,' and very faint for test 'out2.' This shows that fragments smaller than ~100 bp can efficiently be removed from a DNA sample using filtration. Comparison of the 1000-bp bands in all three lanes shows that apparently, only ~25% of the 1000-bp fragments could be recovered after filtration in both tests. For larger fragments, even lower recovery efficiencies were observed. Possibly, this was due to adhesion to the membrane material or due to breaking of the DNA during the centrifugation steps.

Next, the PEG precipitation method was performed with the O'Rangeruler DNA ladder. 10 μl of this DNA ladder was diluted in 0.5× TMS with 10% PEG-8000 to an end volume of 30 μl. After a 10 minute incubation at room temperature, the DNA precipitate was spun down for 30 minutes using a table centrifuge at full speed. The DNA pellet was dissolved in distilled water and loaded on a 2% agarose gel. Figure 4.11 shows a gel with the results of two *in duplo* tests of PEG precipitation. In lanes 3 and 4 of this gel, a significant decrease in intensity of bands <300 bp can be observed. Moreover, a recovery efficiency of the 1000-bp band of 100% can be seen for lane 4 in the profile plot of Figure 4.11b. Also for fragments larger than 1000 bp, recovery efficiencies of >95% were observed. For ϕ29 DNA, resuspension of the

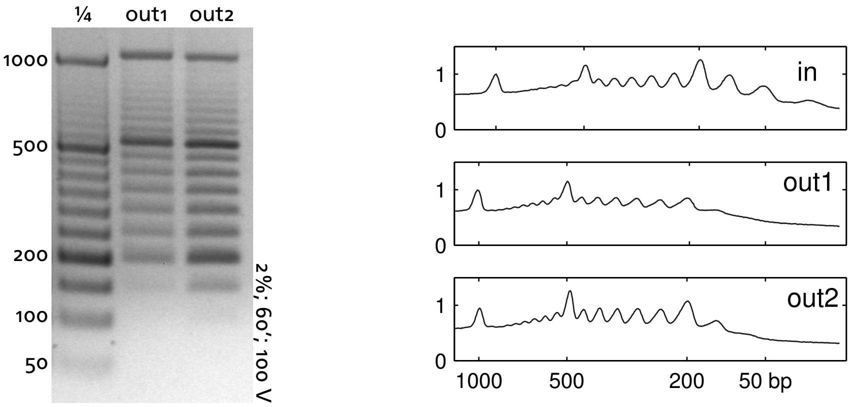

(a) (b)

Figure 4.10: The applicability of Microcon centrifugal filters was tested using a Fermentas O'Rangeruler 50bp DNA ladder. (a) Gel showing the results of two *in duplo* tests of the centrifugal filters ('out1' and 'out2'). For these tests, 10 µl of the DNA ladder was used. For reference, 2.5 µl of the unfiltered DNA ladder was loaded on the left lane. (b) Intensity profile plot of the different lanes. Intensities were normalized with the intensity of the 1000-bp band of lane 'in.'

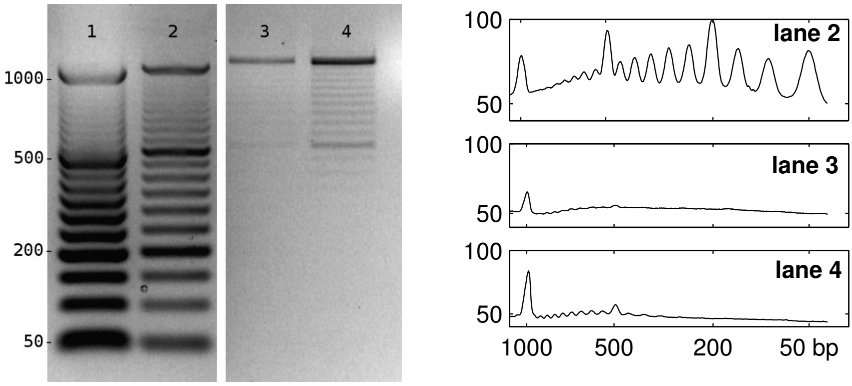

(a) (b)

Figure 4.11: The applicability of PEG-precipitation (10% PEG-8000) for removal of dsDNA oligonucleotides from a DNA mixture is tested on a Fermentas O'Rangeruler 50bp DNA Ladder. (a) The results shown on gel, with on lane 1 the unprocessed ladder, on lane 2 the ladder after DNA purification using a Qiagen Qiaquick spin column, and finally on lane 3 and 4 the yield after PEG precipitation. (b) Intensity profile plot of the different lanes.

DNA pellet was hampered by the gp3 terminal proteins. To improve resuspension for ϕ29 DNA, it was necessary to add 1 µl of glycogen before precipitation.

4.2.4 Ligation of dsDNA oligonucleotides to ϕ29-L fragments

Now that we know how to separate 34-bp oligonucleotides from a DNA mixture with fragments of different lengths, we can perform the ligation of oligonucleotides to the ϕ29-L fragment. This section described the steps followed in this ligation and will show that oligonucleotides can efficiently be ligated to a ϕ29-L fragment to alter its cohesive end.

30 µl of ϕ29 DNA(DNA-gp3) stock solution (corresponding to ~15 µg) was dialyzed for 40 minutes against 50 ml 20 mM Tris-HCl, pH 7.6 to exchange buffers and to remove CsCl from the stock solution. This was done by placing a ∅25 mm membrane filter with 25-nm pores (Millipore) on top of the buffer, and carefully placing the DNA-gp3 solution on top. Next, the DNA-gp3 was digested using 30 units of BglI (New England Biolabs) in 50 µl NEBuffer 3 for one hour at 37°C. Next, the enzyme was inactivated at 65°C for 20 minutes.

A ~0.15 mmol 34-bp dsDNA oligonucleotides (~100× molar excess; for the sequence, see Figure 4.9) and 400 units of T4 DNA ligase (New England Biolabs) were added. ATP was added until an end concentration of 1 mM to start the ligation reaction. The ligation was performed overnight at 16°C, whereafter the T4 DNA ligase was inactivated for 10 minutes at 65°C. Next, unligated oligonucleotides were removed using PEG precipitation: first, 1 µl of glycogen was added and a solution containing 30% PEG-8000 and 10 mM $MgCl_2$ was added until the PEG-8000 concentration was 10%. After a 10 minute incubation at room temperature, the precipitate was spun down for 30 minutes using a table centrifuge at full speed. Now, the pellet was washed by carefully adding 150 µl of 70% ethanol. After 10 minutes of incubation at room temperature, the pellet was again spun down for 5 minutes. Next, the supernatant was removed and the pellet was dried for 15 minutes at room temperature and resuspended in 30 µl (10:0.1) TE buffer (10 mM Tris-HCl, pH 7.8; 0.1 mM EDTA). The DNA concentration was determined by digesting the gp3 and loading 0.5 µl on a 0.3% agarose gel and comparing the intensity of the resulting bands with a Massruler DNA ladder (high range; Fermentas).

To check if all ϕ29-L fragments had an oligonucleotide ligated, the religation of ϕ29-L to ϕ29-R fragments was examined. ϕ29-L fragments without an oligonucleotide ligated to its cohesive end can, after removing free oligonucleotides, ligate to the ϕ29-R fragments and will appear as a 19.3-kbp band on an agarose gel. Figure 4.12 shows the results of this test. In lane 1, BglI-digested ϕ29 DNA is shown after removal of oligos. This DNA was religated by adding T4 DNA ligase and ATP and incubating for 16 hours at 16°C. The result of this ligation is shown in lane 2. As a reference, the efficiency of a 16-h ligation of ϕ29-L to ϕ29-R fragments in the absence of oligonucleotides is shown in lanes 4 and 5. Comparison of lanes 1 and 2 shows that religation of ϕ29-L to ϕ29-R fragments is >99% prevented by ligation

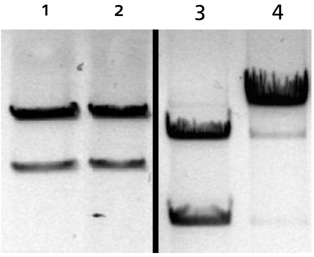

Figure 4.12: Ligation efficiency of 34-bp dsDNA oligonucleotides to ϕ29 DNA fragments. Lane 1 shows BglI-digested DNA after oligonucleotide ligation. After removal of free oligonucleotides, a second 16-h, 16°C ligation was started, yielding lane 1. As a reference, the efficiency of a 16-h ligation of ϕ29-L to ϕ29-R fragments in the absence of oligonucleotides is shown in lanes 4 (before ligation) and 5 (after ligation).

of an oligonucleotides to the ϕ29-L fragments. Hence, all ϕ29-L fragments have an oligonucleotide bound.

4.2.5 Preparation of the 24.4-kbp T7 DNA fragment

Now that we can perform steps 1 and 2 of the ligation strategy depicted in Figure 4.9, we proceed with the preparation of the 24.4-kbp T7 DNA fragment. In summary, bacteriophage T7 DNA is digested with BglII, biotinylated by Klenow filling, further digested using SfiI and consecutively, the 24.4-kbp fragment is purified from the other restriction fragments by gel extraction. Restriction and biotinylation were straightforward and without problems. The gel extraction, however, was inefficient due to the size of the T7 fragment. This section describes the steps followed to obtain the 24.4-kbp T7 fragment.

30 μl of 0.5 mg/ml phage T7 DNA (Bioron) was digested with 30 units of BglII (New England Biolabs) in 50 μl NEBuffer 2 supplemented with 0.1 mg/ml BSA for 1 hour at 37°C. Next, the 5′ ends were biotinylated by adding 2 μl 0.4 mM dATP-14-biotin, 2 μl 0.4 mM dCTP-14-biotin, 0.4 μl 10 mM dGTP, 0.4 μl 10 mM dTTP and 1 μl Klenow Fragment ($3' \rightarrow 5'$ exo$^-$; 15 units) and a 30 minutes incubation at 37°C, after which the Klenow fragment was inactivated at 75°C for 20 minutes. To remove nucleotides and proteins, the DNA sample was dialyzed for 45 minutes against 50 ml water as described earlier. Next, the DNA was further digested by incubation with 40 units of SfiI and 30 units of BclI at 50°C for 1.5 hours. The second restriction enzyme, BclI, was added to facilitate the later gel extraction. After digestion, the DNA sample was run on a 0.8% agarose gel with wide slots for 2 hours at 100 V.

The biotinylated 24-kbp fragment was extracted from the agarose gel by electro-elution using a Genecapsule kit (Genotech). In electro-elution, a gel piece containing the wanted DNA fragment is cut out of the gel. By applying a voltage, the DNA fragment is moved out of the gel piece, where it is captured on a membrane. This yielded DNA in 20–60 μl of the buffer that was used during electrophoresis, 0.5× TBE buffer (Tris-borate EDTA; Sigma-Aldrich). For the 24-kbp fragment, the efficiency of electro-elution was rather low. 70–95% of the DNA was lost in the protocol, mostly due to irreversible binding to the membrane that was used in the elution. Gel extraction techniques using DNA adsorption onto silica surfaces,

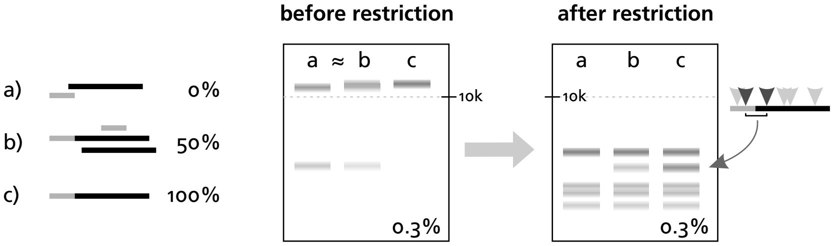

Figure 4.13: Illustration of the restriction analysis that was used to check the ligation efficiency of large DNA fragments. At a–c, three DNA samples are shown with different ligation efficiencies of the gray to the black fragment (0, 50, 100%). When directly loaded on a 0.3% agarose gel, no significant difference can be seen between the lanes corresponding to samples a and b (left). After restriction, however, ligation can be determined from the presence of the DNA fragment that was originally located around the point of ligation (right).

like, e. g., the Qiagen Qiaex II kit, could not be used for fragments >10 kbp. Large fragments either break or do not come off the silica substrate during elution.

After gel extraction, the DNA concentration of the sample was determined by loading 0.5 μl on a 0.3% agarose gel, and comparing the intensity of the resulting band to a Massruler DNA ladder (high range; Fermentas). Because of the high amounts DNA that was lost during electro-elution, the concentration of the T7 DNA sample was usually rather low: 10–100 ng/μl.

4.2.6 Restriction analysis design

To measure the success of ligation of the ϕ29-L fragment to the T7 fragment, we performed a so-called restriction analysis on our DNA sample after ligation. In Figure 4.13, the principle behind this restriction analysis is demonstrated. In the synthesis of our DNA constructs, we used conventional agarose gel electrophoresis to analyze the DNA fragments resulting from the different substeps. Using a 0.3% agarose gel, fragments of up to ~20,000 base pairs can be separated. Larger fragments, however, migrate through the gel at comparable speeds during electrophoresis hence will be visible at equal positions when imaging the gel. Figure 4.14 shows how all fragments >24 kbp of a sample with DNA fragments of various lengths can be seen at equal position. Figure 4.13 shows how a DNA sample is digested with a set of carefully-chosen restriction enzymes, such that the length of the resulting fragments falls in the range where agarose gel electrophoresis has an increased resolving power. The efficiency of ligation can be determined by examining the gel for the presence of the fragment around the point of ligation. Note that if ligation is 100% efficient, the bands corresponding to the fragments that were adjacent to the ligation site in the original black and gray fragment will vanish.

In step 5 of the ligation strategy depicted in Figure 4.9, an 8.4-kbp fragment of ϕ29 DNA is ligated to a 24.4-kbp fragment of T7 DNA, yielding the ϕ29-T7 construct

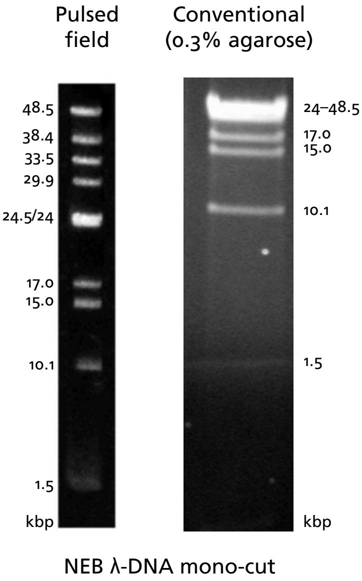

Figure 4.14: Illustration of the limited resolving power of conventional agarose gel electrophoresis for DNA fragments >20 kbp. A sample with DNA fragments of different lengths (1.5–48.5 kbp; New England Biolabs λ DNA-Mono Cut Mix) was run on a 0.3% agarose gel (right). The gel on the left shows the result after pulsed-field gel electrophoresis (adapted from the NEB website).

DNA sample	before restr. (kbp)	NcoI/NheI (kbp)
ϕ29	8.4, 10.9	**2.7**, 4.3, 5.7, 6.7
T7	24.4	**6.3**, 6.7, 11.5
L	32.8, 10.9	4.3, 5.7, 6.7, **8.9**, 11.5

Table 4.1: Fragment lengths of DNA samples before and after digestion by restriction enzymes NcoI and NheI. Sample L represents a DNA sample after ligation of the ϕ29 and T7 fragments with 100% ligation efficiency. The lengths of the fragments that are adjacent to the ligation site are in bold.

of 32.8 kbp. Using conventional agarose gel electrophoresis with 0.3% agarose, the 24.4-kbp fragment cannot be distinguished from the 32.8-kbp fragment, hence this method cannot be directly applied to test the ligation effiency. Making a gel with a lower concentration of agarose is not possible. Moreover, no pulsed-field gel electrophoresis (PFGE, [98]) apparatus was available in our lab to enable separation of larger DNA fragments. For these reasons, we performed a restriction analysis.

To test the efficiency of our ligation strategy, we chose restriction enzymes NcoI and NheI. Table 4.1 shows the fragments resulting from digestion by NcoI and NheI of both the ϕ29 and T7 fragments and of the ligated 32.8-kbp construct (L). If ligation has been 100% efficient, an 8.9-kbp fragment should appear on gel (and a 2.7 and a 6.3-kbp fragment should disappear). Note that in the DNA sample 'L' after ligation, there will be other fragments in the DNA sample: the ϕ29-R fragment and unligated ϕ29-L and T7 fragments. None of these fragments contain both a biotin and a gp3 terminal protein, hence they will not pose a problem in our optical

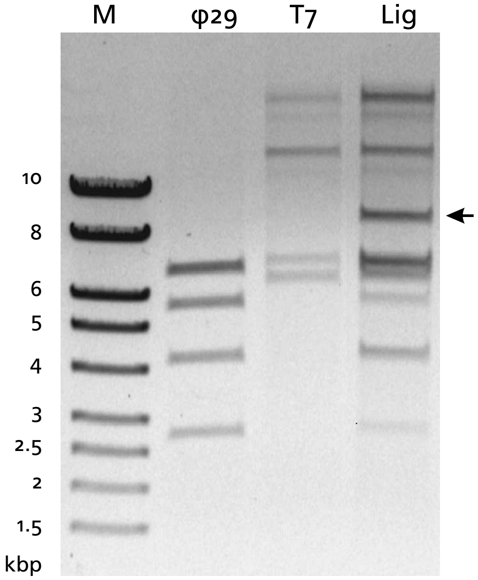

Figure 4.15: The efficiency of ligation of the ϕ29 8.4-kbp fragment to the T7 24.4-kbp fragment was tested using a restriction check with restriction enzymes NcoI and NheI. For comparison, the ϕ29 fragments and the T7 24.4-kbp fragment after digestion by NcoI and NheI are shown with a DNA ladder. The arrow points at the band at 8.9 kbp that shows that ligation has been successful.

tweezers experiments.

4.2.7 Synthesis of a 32.4-kbp ϕ29-T7 construct

Next, the 8.4-kbp ϕ29 fragment was ligated to the 24.4-kbp T7 fragment. ϕ29 sample from PEG precipitation and T7 sample from electro-elution were mixed such that for every T7 fragment, there is around one ϕ29-L fragment. In practice, the concentration of the ϕ29 DNA sample was higher than that of the T7 sample. Therefore, we used all the T7 DNA recovered by electro-elution in the ligation reaction, and the amount of added ϕ29 DNA was tuned such that the molar ratio ϕ29-L:T7 was ~1. Next, 2 µl of T4 DNA ligase (New England Biolabs) was added and 10× T4 DNA ligase buffer was added until the end concentration was 1×. Ligation was performed for 16 hours at 16°C, after which the enzyme was inactivated at 65°C for 10 minutes. Dialysis against 50 ml water as described before was performed to exchange buffers.

To determine the ligation efficiency, ~100 ng of the DNA sample after ligation was subjected to restriction analysis using restriction enzymes NcoI and NheI as described in the previous section. 1 µl of NcoI and 1 µl of NheI were added and the sample was diluted in NEBuffer 2 to an end volume of 20 µl. After 1 hour incubation at 37°C, gp3 was digested and the sample was loaded on a 0.3% agarose gel.

Figure 4.15 shows the results of a restriction analysis after ligation of the 8.4-kbp ϕ29-L fragment to the 24.4-kbp T7 fragment. For comparison, a DNA ladder (M) is shown. In the second and third lane, the ϕ29 and T7 DNA samples are shown, respectively, digested by enzymes NcoI and NheI. Note that in these lanes, all the fragments predicted in Table 4.1 appear. In the T7 lane, some additional bands can be seen with a higher base pair number. These show that digestion has not been 100% complete. The 'Lig' lane shows the results of restriction analysis of the mixed ϕ29 and T7 samples after 16-h ligation. In this lane, a band can be seen between 8 and 10 kbp (indicated with an arrow) that is not present in the ϕ29 and T7 lanes. This band likely corresponds to the 8.9-kbp fragment around the ligation site in the ligated construct, showing that ligation has been successful. Analysis of the band intensities shows that the ligation efficiency has been approximately 60%.

The above example shows a rather high ligation efficiency. In other preparations, we did not reach these efficiencies. Normally, a ligation efficiency of ~10% or lower was reached. Moreover, because of the low concentration of the T7 24-kbp sample, the concentration of the eventual ϕ29-T7 hybrid sample was also rather low (10–100 ng/μl; cf. short DNA sample: 250 ng/μl). Expressed in the concentration of packageable DNA fragments, this comes down to (for ligation efficiency 10%, total DNA concentration 50 ng/μl, number of ϕ29-L fragments in solution equal to T7 fragments) 0.18 nM (cf. short DNA fragment: 20 nM). The reason for the lowered ligation efficiency is unknown as of yet. Independent tests showed that ligation efficiencies of >95% can be reached in the ligation of two 20-kbp fragments. Possibly, the oligonucleotide SfiI-cohesive end was not perfect and therefore could not ligate to the T7 DNA fragment perfectly. An alternative explanation could be the presence of the gp3 terminal protein on the ϕ29 DNA fragments. These enhance supercoiling in DNA [99], thereby possibly hampering ligation due to the altered DNA dynamics.

Optical tweezers packaging experiments that will be presented later in this chapter will show that the ϕ29-T7 construct can indeed be packaged by ϕ29 proheads.

4.3 Optical tweezers experimental procedures

In the previous section, the different DNA constructs that were needed for our optical trapping experiments were described. This section will describe the other steps that were required in our experiments: first the preparation of a trapping sample will be described and next, the optical trapping setup will be briefly introduced.

4.3.1 Preparation of optical tweezers experiment.

In Figure 4.3, the measurement configuration that we used in our optical tweezers experiments was already briefly introduced. Figure 4.16 shows a more step-by-step illustration of an optical tweezers packaging experiment. Before an experiment, stalled prohead-DNA complexes were made in bulk by starting a packaging reaction by mixing DNA-gp3, proheads, ATPase gp16 and ATP, and stalling the reaction prematurely by adding a high concentration of a non-hydrolyzable ATP analogue, ATP-γ-S. These stalled complexes were bound to streptavidin-coated polystyrene microspheres via a biotin on the free end of the DNA. Next, these prohead microspheres were trapped using the optical trap and (1) pushed against another

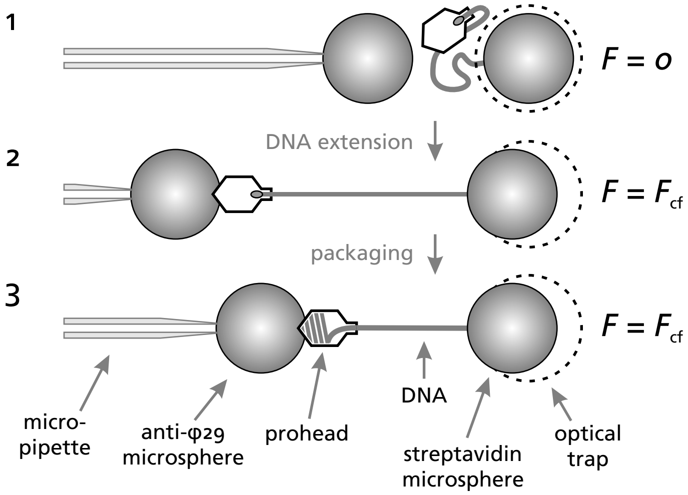

Figure 4.16: Schematic illustration of a constant-force optical tweezers experiment on DNA packaging by bacteriophage ϕ29. (1) By moving the micropipette, an anti-ϕ29 microsphere is touched against an optically trapped microsphere with a prohead attached via its partially packaged DNA. (2) After a connection has been made, the distance between the microspheres is again increased to extend the DNA. (3) The ATP in the surrounding buffer restarts the packaging and the contour length of the DNA tether decreases. The force-feedback mode of the optical tweezers apparatus keeps the force on the construct constant and the micropipette is moved back to the optical trap.

polystyrene microsphere that was previously coated with anti-ϕ29 antibodies. If a connection was obtained via a single-DNA, an experiment could be started by (2) again increasing the distance between the two microspheres by moving the micropipette. The ATP in the surrounding buffer will again start the packaging reaction. Because of the packaging, the contour length of the tethered DNA would decrease and the force on the trapped microsphere is increased. By switching on the constant-force mode of the optical tweezers setup, the force exerted on the trapped microsphere will be kept constant by moving the micropipette. (3) Now, the distance between the two microspheres will slowly decrease as packaging proceeds.

Next, we give a more step-by-step protocol for the experiment: first, the stalled complexes were prepared. Components of the ϕ29 *in vitro* packaging assay, including proheads, DNA-gp3 and gp16, were purified as described previously [99]. Next, we mixed 2 µl of the short, biotinylated DNA (~0.5 µg) and 1 µl 0.5 mg/ml gp16 with 10 µl of water and 1.5 µl of 5× TMS. In the experiments where the less concentrated long-DNA sample was used, the water and DNA were replaced with 12 µl of the dialyzed long DNA sample. After 1 minute, 1.5 µl 6 mg/ml prohead solution was added. After another minute incubation, 4 µl of 0.25 mM ATP in TM buffer (50 mM Tris-HCl, pH 7.6; 3 mM $MgCl_2$) was added (end concentration 50 µM) to start the

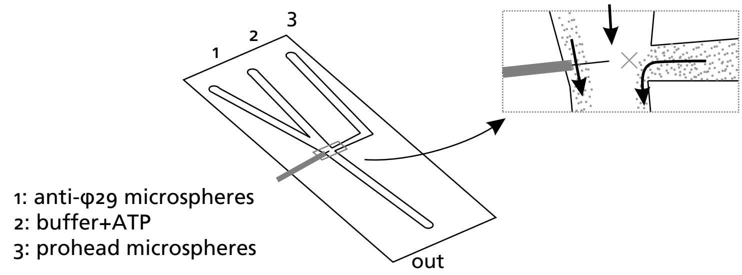

Figure 4.17: Cartoon of the flow cell that was used in the optical tweezers experiments on packaging by bacteriophage ϕ29. The inset in the top right shows in detail the direction of the different flows around the flow cell center.

packaging reaction. After ~30 s of packaging, the reaction was stopped by adding 4 μl 2.5 mM ATP-γ-S in TM buffer (end concentration 2.5 mM).

5 μl of streptavidin-coated polystyrene microspheres (2.2 μm; 0.5%; Spherotech) were washed twice with 200 μl of 0.5× TMS, using protein LoBind centrifuge tubes (Eppendorf). The microspheres were resuspended in 20 μl of 0.5× TMS, and subsequently blocked by adding 1 μl 100 mg/ml bovine serum albumin (BSA) and a 5 minute incubation under constant rotation. Next, 1 μl of RNase inhibitor (Eppendorf) was added and 5 μl of the stalled complex solution was added to 5 μl of the microsphere suspension and incubated for >20 minutes under constant rotation. For the long-DNA sample, a relatively lower amount of microsphere suspension was added (down to 0.5 μl of microsphere suspension per 20 μl of long-DNA stalled complexes). Before the trapping experiment, the microspheres were diluted in 0.5 ml 0.5× TMS.

Anti-ϕ29 microspheres were prepared as follows: 50 μl of protein G-coated polystyrene microspheres (2.88 μm; 0.5%; Spherotech) were washed 2 times with 200 μl PBS (Biochrom AG) and resuspended in 20 μl PBS. Next, 1 μl of rabbit antisera against ϕ29 was added. After a 20 minutes incubation under constant rotation, the microspheres were washed twice in PBS and 3 times in 0.5× TMS. The microspheres were resuspended in 20 μl 0.5× TMS and 1 μl of RNase inhibitor was added. Before the trapping experiment, the microspheres were diluted in 1 ml 0.5× TMS.

The experiment was performed in a flow cell as sketched in Figure 4.17 (see also Chapter 1). Channel 1 is connected to a syringe with the diluted anti-ϕ29 microspheres. Channel 3 is connected to a syringe with the diluted prohead microspheres. The reaction buffer in channel 2 consists of 0.5× TMS supplemented with 0.5 mM ATP and 0.5% BSA. To start an experiment, first, an anti-ϕ29 microsphere was trapped and transferred to the micropipette using the optical trap. Next, a microsphere carrying stalled complexes was grabbed from the prohead microsphere flow and an experiment could be started. The outlet of channel 3 into the main channel was designed such that the exposure of the stalled complexes to the ATP in the main channel flow was minimized (see top right of Figure 4.17).

4.3.2 Optical tweezers setup

For these experiments, the optical tweezers setup that was presented in Chapter 1 was used, with the Nd:YVO_4 laser as a trapping laser. The laser diode current of the setup was kept at 9 A. By fitting a Lorentzian to the power spectral density (PSD) of the movements of a trapped microsphere (see Chapter 1), the force constant of the optical tweezers and the sensitivity of the QPD were determined every day before doing experiments. On average, the force constant for a 1.88 µm polystyrene microsphere along the x coordinate was 169 pN/µm with a standard deviation of 24 pN/µm. The sensitivity of the QPD was on average ~2.74 V/µm with a standard deviation of 0.24 V/µm. The standard deviation σ_F of the noise in force measurement was 0.11 pN (measured during 1 s).

During the experiments, microsphere movements were measured by recording the normalized QPD x and y voltage signals at a frequency of 50 Hz. The analog electronics anti-aliasing filter was set at a filter frequency of 20 Hz. Additionally, the Labview particle tracking algorithm was used to track microspheres at a lower frequency (~5 Hz). For the analysis and for plots, the QPD data was used. The particle tracking data was only used for calibration.

The contour length of DNA (in base pairs) was determined from the measured force and the DNA end-to-end distance, and through using the inextensible worm-like chain (WLC) model assuming a persistence length of 53 nm [7], a stretch modulus of 1200 pN [5] and a distance per base pair of 0.34 nm [100].

4.4 Results

This section will show the results of our optical tweezers experiments on the packaging of DNA by bacteriophage ϕ29. First, the packageability of the long DNA construct was tested. It was shown that this construct can indeed be packaged by bacteriophage ϕ29. We did not have enough time, however, to fully explore our research aims: the effect of spermine, and single stranded breaks or nicks, on packaging in the high density regime. Using the short DNA construct, we did perform packaging experiments in the presence of spermine.

4.4.1 Packaging of long DNA

In the previous text, we described a novel method of making an extended ϕ29 DNA construct. In this section, we will show that this DNA construct can be packaged by ϕ29 proheads in an optical tweezers assay. As said before, the concentration of packageable fragments in the long-DNA sample was rather low (~0.18 nM vs 20 nM for the short DNA sample). In the preparation of the optical tweezers sample (see previous section), this was compensated for by increasing the volume of DNA sample that was added in the preparation (from 2 µl to 12 µl). Nevertheless, the total number of packageable DNA fragments in the preparation was still ~19× lower in the preparation of a long-DNA trapping sample, compared to a short-DNA

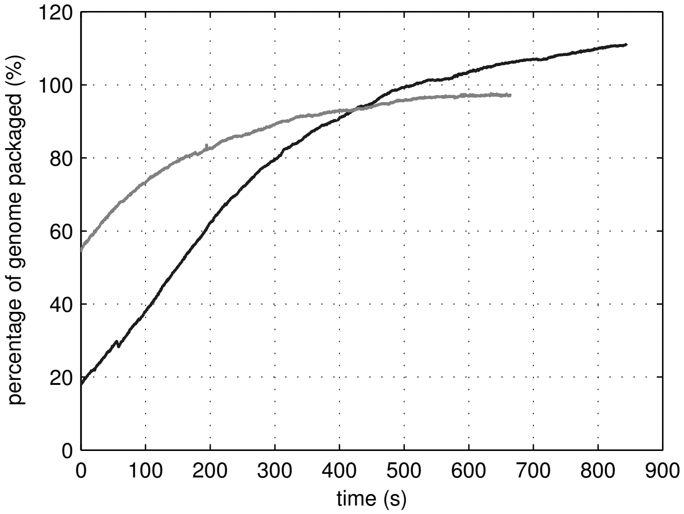

Figure 4.18: Two optical tweezers measurements of packaging by bacteriophage ϕ29. The *y* axis represents the length of the DNA that has been packaged, relative to the ϕ29 genome length (19,285 bp).

trapping sample. To increase the average number of packageable DNA fragments per microsphere, the amount of microsphere suspension added to the stalled complex sample could be lowered to increase the DNA density on the microsphere surface.

For our experiments, microspheres and flow cell were prepared as described in the previous section. A single prohead-DNA construct was tethered and extended and relaxed several times. The constant-force mode was switched on as soon as packaging was observed as a slow increase in the force. During packaging, the construct was held at a force of ~5 pN.

Figure 4.18 shows two packaging measurements. Plotted are the contour length of the packaged DNA construct, relative to the 19.3-kbp ϕ29 genome, as a function of time. At the start of the measurement, the gray curve is in a further state of packaging than the black curve. In both curves, initially, the amount of DNA packaged rises more or less linearly with time. After a certain amount of time, it can be seen that a plateau is reached, showing that the bacteriophage has been filled and no more DNA can be packaged anymore. In Figure 4.19, the packaging speed (in bp/s) is shown as a function of the percentage of the ϕ29 genome that has been packaged. Again, the black curve of this graph shows that initially, the packaging rate is more or less constant (~45 pN) and at 60% packaging, the packaging speed slowly goes down to 0 at ~110%.

In the beginning of this chapter, some data taken by Smith et al. [5] was shown. In comparison, Figure 4.4b and the black curve of Figure 4.19 are very similar. Both show a decrease of the packaging speed starting at 50%, lasting until an amount

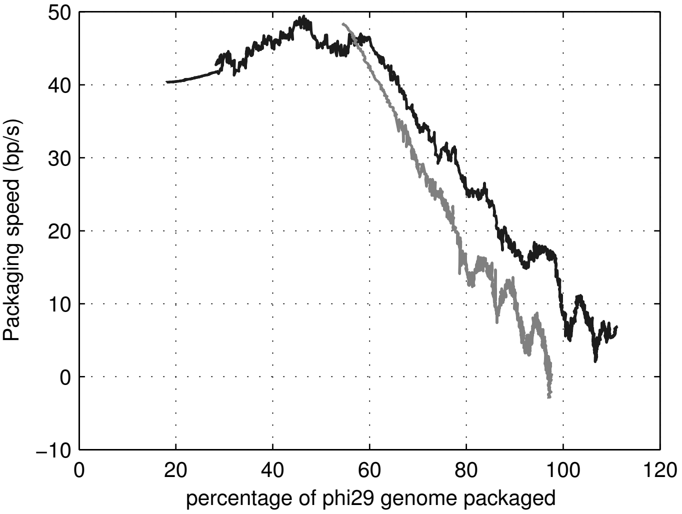

Figure 4.19: Packaging speeds of two optical tweezers measurements on DNA packaging by bacteriophage φ29. Packaging speeds were obtained by downsampling the data from 50 Hz to 2 Hz, differentiation, and smoothing the data using a Savitzky-Golay filter with polynomial order 2 and a frame size of 201 points.

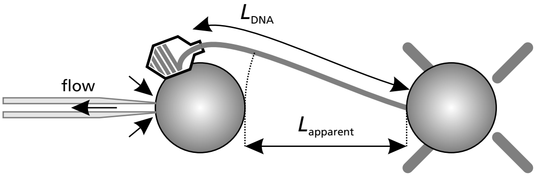

Figure 4.20: Schematic illustration of a tethered prohead that did not bind at the original point of contact between the two microspheres. This effect was sometimes enhanced by buffer flow along the microsphere surface due to an insufficient seal between microsphere and micropipette (indicated with arrows).

of DNA equivalent to 110% the φ29 genome has been packaged. Remarkably, the packaging rate we observe in the low density regime (50 bp/s) is around twice as low as the packaging speed observed by Smith et al.. The packaging speed of the gray curve is already in decline at the beginning of the measurement. For this curve, packaging stops if ~90% of the φ29 genome has been packaged. This observation can be explained from the artifact that is sketched in Figure 4.20: when the prohead and the anti-φ29 microsphere are brought together, a free prohead may bind to the anti-φ29 microsphere at a point different from the point of contact between the two microspheres. This was sometimes enhanced by buffer flow along the

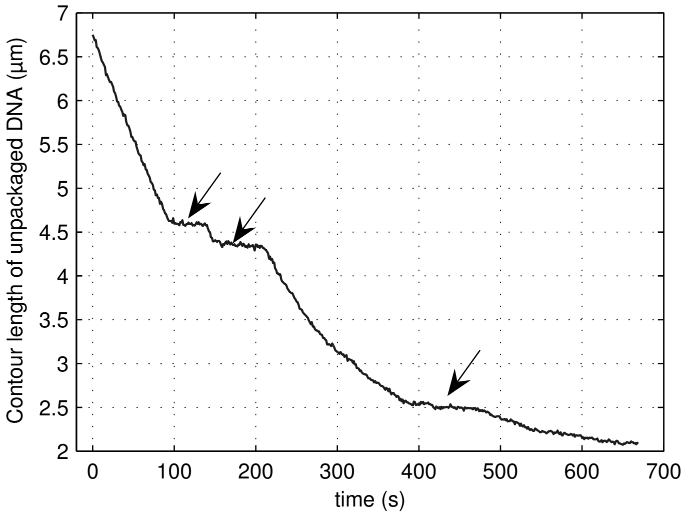

Figure 4.21: Example of a packaging experiment that shows at least three pauses in the packaging. Pauses could take up to 1 minute.

anti-ϕ29 microsphere into the micropipette, due to a non-perfect seal between the micropipette tip and the microsphere. Because of this artifact, the contour length appeared shorter than the actual contour length, hence packaging appeared to have proceeded further.

In our measurements, we sometimes observed pauses in the packaging. An example of a measurement showing pauses is shown in Figure 4.21. Smith et al. observed similar pauses, but molecular mechanism for these pauses could not be given.

4.4.2 The effect of spermine on packaging of DNA by bacteriophage ϕ29

DNA force–extension measurements in the presence of spermine Next, we looked at the effect of the tetravalent cation spermine on the packaging process. Before doing the packaging experiments, we did not know the range of concentrations where spermine induces condensation of DNA under our conditions. Raspaud et al. [101] performed condensation studies with different concentrations of DNA, spermine and sodium chloride, but did not include the magnesium chloride that is required in our packaging assay. To find the range of concentrations where spermine induces condensation of DNA in the buffer that was used in our experiments, 0.5× TMS(25 mM Tris-HCl, pH 7.8; 5 mM $MgCl_2$; 50 mM NaCl), we performed single-molecule DNA stretching experiments in the presence of spermine, as sketched in Figure 4.22. In this experiment, a ~5700-bp DNA fragment

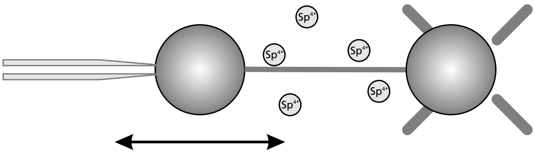

Figure 4.22: Optical trapping configuration in DNA extension experiments in the presence of spermine. Sp^{4+} indicates a spermine cation.

with covalently bound biotin groups on one end, and digoxigenin groups on the other end is tethered between an optically-trapped streptavidin microsphere and an anti-digoxigenin microsphere that is being held by a micropipette. The experiment is performed in 0.5× TMS. The micropipette microsphere is sweeped to and from the optically-trapped microsphere several times to measure the force–extension curve in the absence of spermine. Next, 0.5× TMS supplemented with spermine is flown in the flow cell. Experiments have been performed at spermine concentrations of 0.1–10 mM. After spermine had been flown in, some more force–extension curves were measured.

From literature [94], it is known that in force–extension curves in the presence of condensing agents, one can expect four regimes, at different concentrations of the condensing agent: (I) At low concentrations, no condensation effects can be observed. (II) From a certain critical concentration, a force plateau of several piconewtons can be observed in the force–extension curve. (III) At slightly higher concentrations, a stick-release pattern can be observed. (IV) From a second critical concentration, no condensation effects can be observed anymore.

In our measurements, we observed both regimes of condensation. At concentrations of 1 mM and below, no condensing effect of the spermine could be observed. At 3 mM, we observed force plateaus of several pN in the force–extension curves. Figure 4.23 shows an example of such a measurement. This graph shows one force–extension curve measured in the absence of spermine (black) and two measured in the presence of 3 mM spermine. For the latter two curves, a distinct plateau can be observed at 2–4 pN. When looking at the plateau in more detail, one can even observe 2-pN transitions between different levels within these plateaus. In the light gray curve, three different of these transitions can be observed (at extensions 0.8, 1.3, 1.6 μm). Wada et al. [102] have modeled these force plateaus as the transient formation and dissociation of condensates in the DNA molecule. Similar steps in the force plateau have not been observed before.

Figure 4.24 shows an example of a measurement performed in the presence of 10 mM spermine. This graph shows two force–extension curves measured in the presence of 10 mM spermine (interrupted lines) and one measured in 0.5× TMS without spermine. Stick-release features can clearly be observed in the spermine measurements, as a rise in force (up to 23 pN) at low extensions. For one of the curves, two subsequent stick-release features can be seen (at ~0.7 μm and at 1 μm).

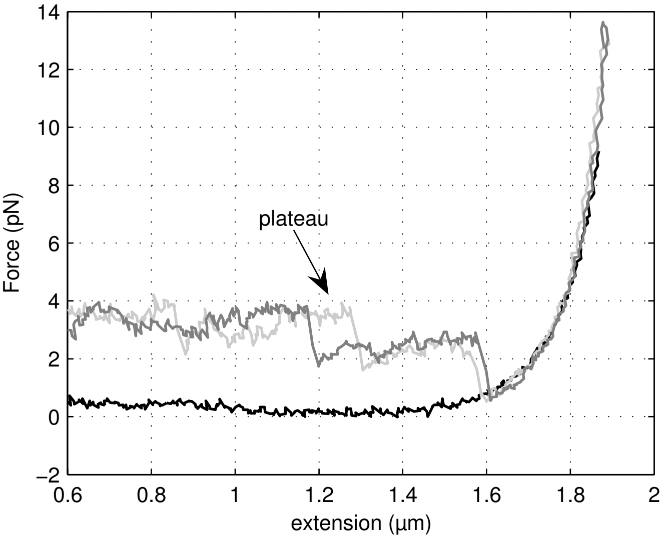

Figure 4.23: Force–extension curves of 5700-bp dsDNA measured in the presence of 3 mM spermine. The black curve is measured in the absence of spermine.

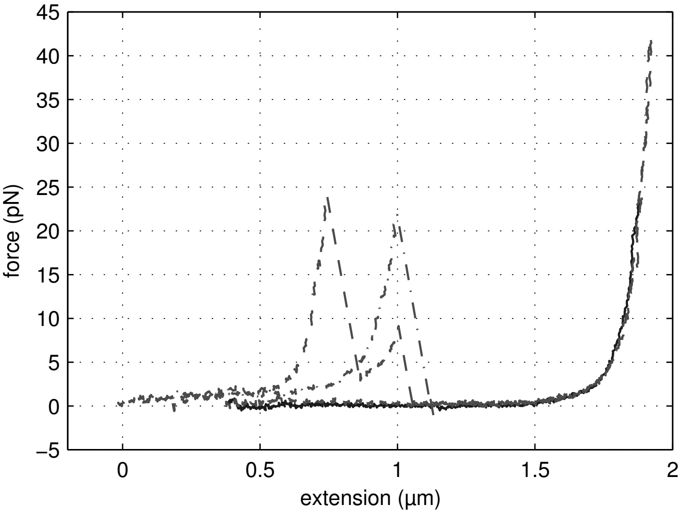

Figure 4.24: Force–extension curves of 5700-bp dsDNA measured in the presence of 10 mM spermine. The black, uninterrupted curve is measured in the absence of spermine.

In literature, similar stick-release patterns were attributed to the sudden unraveling of relatively stable toroidal condensates (see Figure 4.5) in the DNA.

The steps in the force plateau that we observed at 3 mM of spermine could be attributed to a combined effect of stick-release features and a force plateau (i. e., a combined transient condensation and the formation of more stable condensates that are not as stable as in the 10 mM case).

Optical tweezers packaging experiments in the presence of spermine Knowing the spermine concentrations at which condensation of the DNA takes place, we can start adding spermine during optical tweezers packaging experiments. To check whether packaging of DNA by ϕ29 proheads is at all possible in the presence of condensing concentrations of spermine, we performed packaging experiments using the short DNA that was introduced before, at spermine concentrations of 3 mM and at 10 mM. These experiments were performed as described before, with spermine added to the packaging buffer. Before each packaging experiment, the DNA was fully extended to pull condensates out of the DNA. The packaging experiments we did at different spermine concentrations showed that, at all the used spermine concentrations, even in the stick-release regime, packaging is similar to when no spermine is there, with comparable packaging speeds. Hence, in the low density regime of packaging, condensation of the DNA inside and outside the prohead does not apparently affect the packaging.

As outlined at the beginning of this chapter, the most interesting effect of spermine on packaging is to be expected when the prohead is more than ~50% full with DNA and spermine would be able to compensate for electrostatic repulsion between DNA strands. Follow-up measurements are required to study this effect. Before doing more experiments, we had given priority to other experiments (see Chapter 3), hence they could not yet be performed.

4.4.3 Packaging of nicked DNA by bacteriophage ϕ29

Next, optical tweezers packaging experiments were performed to look at the effect of nicks, or single-stranded breaks in the DNA, on the packaging process. Before doing the optical tweezers experiment, we used nicking enzymes Nb.BsmI or Nt.AlwI, to specifically nick the DNA at distinct sites. Also aspecific nicking with low concentrations of DNase I [95] has been explored. Packaging experiments were performed in the force-feedback mode at forces of 5–25 pN. We expected that at higher forces, the structure of DNA around a nick would be most different from the structure of intact DNA. A possible effect of a nick could be that the packaging motor loses grip on the DNA. This could then be detected as a slipping back of the DNA until the motor grabs on the DNA again. Higher pulling forces than 25 pN were not practical, since the connection often would break somewhere along the construct.

In the measurements that were performed up to now, at all the used forces, no specific effects (e. g., pauses, slips) could be observed as the packaging motor passed a nick in the DNA. Apparently, the applied force did not alter the structure of DNA enough around the nick to affect the passing motor in a visible way. More measurements are needed to confirm this. A DNA construct with multiple nicks such as the DNase I-nicked DNA can help because a higher number of 'nick-passing' events per packaging measurement can be reached in this way.

4.5 Discussion

This chapter presented optical tweezers measurement on dsDNA packaging by bacteriophage ϕ29. In our experiments, we were interested in the high-density regime of packaging, i. e., when more than ~50% of the ϕ29 genome has been packaged, and large entropic, electrostatic and bending energies have to be overcome to package the full 19.3-kbp genome in a cavity of only 42 nm×54 nm. One of our aims was to study the effect of lowering the electrostatic repulsion between neighboring strands of the packaged DNA by adding the polyvalent cation spermine during the packaging reaction. Furthermore, we wanted to study the effect of altering bending energies in the tightly bent packaged DNA by introducing nicks, or single-stranded breaks in the DNA.

To perform these experiments, we introduced a novel method of extending the ϕ29 DNA by 68%. We used non-palindromic restriction enzymes and linker oligonucleotides to link a 8.4-kbp ϕ29-L fragment to a 24.4-kbp phage T7 fragment. We have shown that this method can lead to a construct that can indeed be used in optical-tweezers packaging experiments.

In the synthesis of the long DNA construct, there appeared to be room for improvements. Purification of the 24.4-kbp T7 DNA fragment from gel appeared cumbersome and up to 95% of the DNA was lost in the process. This problem is mostly due to the length of the fragment. Most of the available protocols for gel extraction of DNA fragments are quite inefficient for fragments over 10 kbp. To reduce the loss of T7 DNA, gel extraction methods with increased efficiency should be explored. Alternatively, gel extraction could be avoided by ligating a second oligonucleotide to the T7 cohesive end. This oligonucleotide could then be designed such that it ligates to the ϕ29-L oligonucleotide, while preventing the religation to the other T7 fragments that remain in the DNA sample.

Another problem was the low efficiency in the final ligation of this T7 DNA fragment to a ϕ29 DNA left end. It has been shown that it is possible to reach efficiencies in ligation of ~60%, but in most of the preparations, up to ~10% was reached. A more controlled ligation procedure should be developed to consistently reach ligation efficiencies of >50%.

We used a short DNA construct to study the effect of both nicks and spermine on the low-density regime of packaging. No detectable effects on both the packaging speed and the presence of slips and pauses could be observed here. This agrees with the idea that electrostatic effects play no role in the first phase of packaging. To find the spermine concentration at which DNA is condensed in 0.5× TMS, we performed optical tweezers DNA stretching experiments. These showed a force plateau in the force–extension curve in 0.5× TMS supplemented with 3 mM and stick-release phenomena when 10 mM spermine was added.

Further measurements, using the long DNA construct in packaging experiments involving spermine or nicks, are needed to further address the questions asked in the beginning of this chapter.

A

The worm-like chain (WLC) model

To model the extension of dsDNA and polypeptides in our experiments, we used the worm-like chain model. We will present two variants of this model: the inextensible and the extensible worm-like chain model.

For the experiments that are presented in this thesis, knowing the elastic properties of double-stranded DNA (dsDNA) is extremely important. In Chapters 2 and 3, dsDNA is used as a molecular spacer between the (pre-)protein that is being studied and the optically trapped microsphere that is used to measure forces. In Chapter 4, the shortening of dsDNA as it is being packaged by a bacteriophage is measured. In the measurements presented in these chapters, DNA compliance obscures the phenomena of interest: protein translocation, polypeptide extension after unfolding and packaging speeds, respectively. Knowing the elastic properties of dsDNA, one can remove effects stemming from DNA compliance from the measurements and focus on the phenomenon of interest.

In solution, a relaxed dsDNA molecule bends and curves locally as a result of thermal fluctuations. Even when a small force is exerted on both ends, these fluctuations will cause the end-to-end distance to be smaller than the DNA contour length L. This bending results in an elasticity that is purely entropic of origin.

For low forces (F<5 pN), DNA elasticity can best be described by the inextensible *worm-like chain* (WLC) model. In this model, the DNA is treated as a flexible rod of length L that curves smoothly as a result of thermal fluctuations. The rod's local direction decorrelates at a distance s along the curve according to $\exp(-sP)$, where the decay length, P, is the persistence length. In this thesis, we used the value of the persistence length that was found by Smith et al. [103] and that is used most often in literature: 53 nm. Using the inextensible WLC model, the force required to extend a DNA strand of contour length L to end-to-end distance x can be calculated numerically. Moreover, a useful approximation was given by Bustamante et al. [7]:

$$\frac{FP}{k_{\mathrm{B}}T} = \frac{1}{4}\left(1 - \frac{x}{L}\right)^{-2} - \frac{1}{4} + \frac{x}{L}. \tag{A.1}$$

At forces higher than ~5 pN, the DNA force–extension curve deviates from the inextensible WLC model. At forces between 5 and 50 pN, the DNA elasticity is no longer merely entropic. The DNA can be extended here to extensions beyond

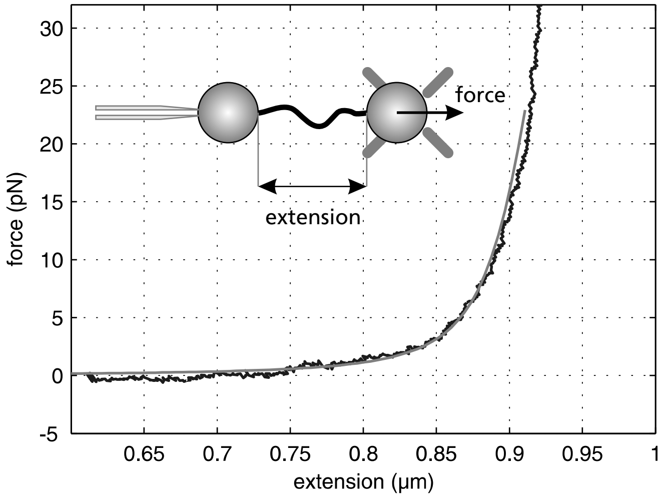

Figure A.1: Force–extension curve of a dsDNA molecule with a contour length of 920 nm (black). The experimental configuration is shown. The gray curve indicates an extensible worm-like chain (WLC) model with a persistence length of 53 nm, a contour length of 920 nm and an elastic stretch modulus of 1200 pN.

its contour length, indicating the existence of an intrinsic elasticity of the fully extended molecule. The extension x of a DNA molecule that is being held by a force F can here be approximated using the *extensible* worm-like chain model [104, 100]:

$$\frac{x}{L} = 1 - \frac{1}{2}\left(\frac{k_\mathrm{B}T}{FP}\right)^{1/2} + \frac{F}{S}, \tag{A.2}$$

where S is the elastic stretch modulus of DNA. In this thesis, a value of 1200 pN is used for S. This value is used often in literature (see, e. g., Smith et al. [5]) and gives good agreement with experimental data.

In Figure A.1, an example of a dsDNA force–extension curve is shown, measured using our optical-tweezers setup. For this measurement, a DNA molecule with a contour length L of 920 nm was tethered between an optically trapped microsphere and a microsphere that was held by a micropipette as shown. For the connections of the DNA to the microspheres, biotin/streptavidin and digoxigenin/anti-digoxigenin interactions were used. By moving the micropipette away from the optical trap, the DNA extension was increased and the trapped microsphere was slowly pulled away from the trap center by the increased force. This graph also shows the force–extension curve that is predicted by the extensible WLC model, showing a clear overlap between theory and experiment.

In Chapters 2 and 3, we model the force–extension of a DNA molecule and a coupled unfolded polypeptide. Here, the polypeptide is modeled using the inex-

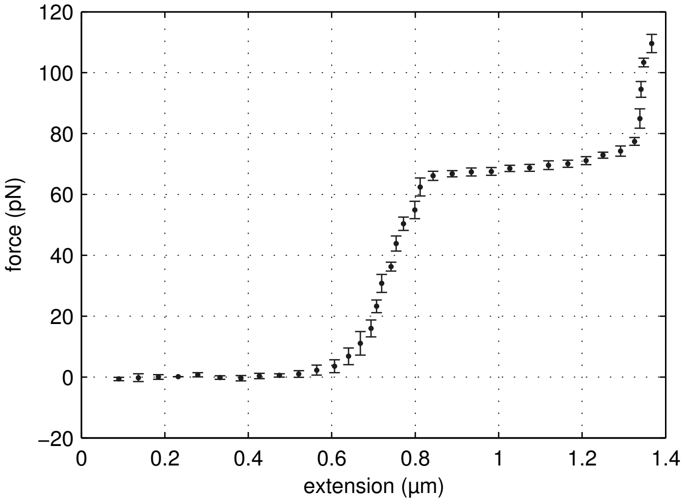

Figure A.2: Overstretching transition in a dsDNA molecule with contour length 800 nm.

tensible WLC model with a persistence length of 0.5–2 pN and the force–extension curve can be calculated by regarding the DNA and the polypeptide as two springs in series ($F_{\mathrm{DNA}}(x_{\mathrm{DNA}}) = F_{\mathrm{polypeptide}}(x_{\mathrm{polypeptide}})$ and $x_{\mathrm{DNA}} + x_{\mathrm{polypeptide}} = x_{\mathrm{tot}}$). For, polypeptides, we used the inextensible WLC model rather than the extensible WLC model because it gave better agreement with the data.

At forces of 65 pN or more, the extended DNA molecule undergoes a so-called overstretching transition [105, 106]. In this transition, the DNA molecule can be extended up to 70% beyond its contour length. Figure A.2 shows the overstretching transition of a 800-nm DNA strand, tethered between two microspheres. In the overstretching transition, the canonical B-form DNA is deformed into so-called S-form DNA. It is thought that during the overstretching transition from B-DNA to S-DNA the double helix structure is slowly unwound. The force–extension curve of this S-DNA resembles that of single-stranded DNA.

Bibliography

[1] A. Ashkin, J. M. Dziedzich, J. Bjorkholm, and S. Chu. Observation of a single-beam gradient force optical trap for dielectric particles. *Opt. Lett.*, 11(5):288–290, 1986.

[2] A. Ashkin and J. M. Dziedzic. Optical trapping and manipulation of viruses and bacteria. *Science*, 235(4795):1517–1520, 1987.

[3] K. Svoboda, C. F. Schmidt, B. J. Schnapp, and S. M. Block. Direct observation of kinesin stepping by optical trapping interferometry. *Nature*, 365(6448):721–727, 1993.

[4] J. E. Molloy, J. E. Burns, J. C. Sparrow, R. T. Tregear, J. Kendrick-Jones, and D. C. White. Single-molecule mechanics of heavy meromyosin and S1 interacting with rabbit or Drosophila actins using optical tweezers. *Biophys. J.*, 68(4 Suppl):298S–303S; 303S–305S, 1995.

[5] D. E. Smith, S. J. Tans, S. B. Smith, S. Grimes, D. L. Anderson, and C. Bustamante. The bacteriophage phi29 portal motor can package DNA against a large internal force. *Nature*, 413:748–52, 2001.

[6] G. J. Wuite, S. B. Smith, M. Young, D. Keller, and C. Bustamante. Single-molecule studies of the effect of template tension on T7 DNA polymerase activity. *Nature*, 404(6773):103–106, 2000.

[7] C. Bustamante, J. F. Marko, E. D. Siggia, and S. B. Smith. Entropic elasticity of lambda-phage DNA. *Science*, 265:1599–600, 1994.

[8] M. S. Kellermayer, S. B. Smith, H. L. Granzier, and C. Bustamante. Folding-unfolding transitions in single titin molecules characterized with laser tweezers. *Science*, 276(5315):1112–1116, 1997.

[9] C. Cecconi, E. A. Shank, C. Bustamante, and S. Marqusee. Direct observation of the three-state folding of a single protein molecule. *Science*, 309(5743):2057–2060, 2005.

[10] G. Koster, M. VanDuijn, B. Hofs, and M. Dogterom. Membrane tube formation from giant vesicles by dynamic association of motor proteins. *Proc. Natl. Acad. Sci. U. S. A.*, 100(26):15583–15588, 2003.

[11] J. W. J. Kerssemakers, E. L. Munteanu, L. Laan, T. L. Noetzel, M. E. Janson, and M. Dogterom. Assembly dynamics of microtubules at molecular resolution. *Nature*, 2006.

[12] F. Gittes and C. F. Schmidt. Interference model for back-focal-plane displacement detection in optical tweezers. *Opt. Lett.*, 23:7–9, 1998.

[13] K. Svoboda and S. M. Block. Biological applications of optical forces. *Annu. Rev. Biophys. Biomol. Struct.*, 23:247–85, 1994.

[14] W. Wickner, A. J. Driessen, and F. U. Hartl. The enzymology of protein translocation across the Escherichia coli plasma membrane. *Annu. Rev. Biochem.*, 60:101–124, 1991.

[15] L. Chen and P. C. Tai. ATP is essential for protein translocation into Escherichia coli membrane vesicles. *Proc. Natl. Acad. Sci. U. S. A.*, 82(13):4384–4388, 1985.

[16] K. Shiozuka, K. Tani, S. Mizushima, and H. Tokuda. The proton motive force lowers the level of ATP required for the in vitro translocation of a secretory protein in Escherichia coli. *J. Biol. Chem.*, 265(31):18843–18847, 1990.

[17] K. Yamane, S. Ichihara, and S. Mizushima. In vitro translocation of protein across Escherichia coli membrane vesicles requires both the proton motive force and ATP. *J. Biol. Chem.*, 262(5):2358–2362, 1987.

[18] P. Fekkes and A. J. Driessen. Protein targeting to the bacterial cytoplasmic membrane. *Microbiol. Mol. Biol. Rev.*, 63(1):161–173, 1999.

[19] T. B. Topping and L. L. Randall. Chaperone SecB from Escherichia coli mediates kinetic partitioning via a dynamic equilibrium with its ligands. *J. Biol. Chem.*, 272(31):19314–19318, 1997.

[20] E. Schiebel, A. J. Driessen, F. U. Hartl, and W. Wickner. Delta mu H+ and ATP function at different steps of the catalytic cycle of preprotein translocase. *Cell*, 64(5):927–939, 1991.

[21] J. P. van der Wolk, J. G. de Wit, and A. J. Driessen. The catalytic cycle of the escherichia coli SecA ATPase comprises two distinct preprotein translocation events. *EMBO J.*, 16(24):7297–7304, 1997.

[22] K. Uchida, H. Mori, and S. Mizushima. Stepwise movement of preproteins in the process of translocation across the cytoplasmic membrane of Escherichia coli. *J. Biol. Chem.*, 270(52):30862–30868, 1995.

[23] A. J. M. Driessen, E. H. Manting, and C. van der Does. The structural basis of protein targeting and translocation in bacteria. *Nat. Struct. Biol.*, 8:492–498, 2001.

[24] J. de Keyzer, C. van der Does, and A. J. M. Driessen. The bacterial translocase: a dynamic protein channel complex. *Cell. Mol. Life Sci.*, 60(10):2034–2052, 2003.

[25] A. R. Osborne, , and T. A. Rapoport. A large conformational change of the translocation ATPase SecA. *Proc. Natl. Acad. Sci. U. S. A.*, 2004.

[26] Z. Xu, J. D. Knafels, and K. Yoshino. Crystal structure of the bacterial protein export chaperone SecB. *Nat. Struct. Biol.*, 7(12):1172–1177, 2000.

[27] B. Van Den Berg, W. M. Clemons, I. Collinson, Y. Modis, E. Hartmann, S. C. Harrison, and T. A. Rapoport. X-ray structure of a protein-conducting channel. *Nature*, 427:36–44, 2003.

[28] R. A. Arkowitz, J. C. Joly, and W. Wickner. Translocation can drive the unfolding of a preprotein domain. *EMBO J.*, 12(1):243–253, 1993.

[29] D. Tomkiewicz, N. Nouwen, R. van Leeuwen, S. Tans, and A. J. M. Driessen. SecA supports a constant rate of preprotein translocation. *J. Biol. Chem.*, 281(23):15709–15713, 2006.

[30] F. Baneyx and G. Georgiou. In vivo degradation of secreted fusion proteins by the Escherichia coli outer membrane protease OmpT. *J. Bacteriol.*, 172(1):491–494, 1990.

[31] A. Kaufmann, E. H. Manting, A. K. Veenendaal, A. J. Driessen, and C. van der Does. Cysteine-directed cross-linking demonstrates that helix 3 of SecE is close to helix 2 of SecY and helix 3 of a neighboring SecE. *Biochemistry*, 38(28):9115–9125, 1999.

[32] A. Pautsch and G. E. Schulz. High-resolution structure of the OmpA membrane domain. *J. Mol. Biol.*, 298(2):273–282, 2000.

[33] D. B. Oliver and J. Beckwith. E. coli mutant pleiotropically defective in the export of secreted proteins. *Cell*, 25(3):765–772, 1981.

[34] J. de Keyzer, C. Van Der Does, and A. J. Driessen. Kinetic analysis of the translocation of fluorescent precursor proteins into Escherichia coli membrane vesicles. *J. Biol. Chem.*, 277, 2002.

[35] R. J. Cabelli, L. Chen, P. C. Tai, and D. B. Oliver. SecA protein is required for secretory protein translocation into E. coli membrane vesicles. *Cell*, 55(4):683–692, 1988.

[36] P. Fekkes, J. G. de Wit, J. P. van der Wolk, H. H. Kimsey, C. A. Kumamoto, and A. J. Driessen. Preprotein transfer to the Escherichia coli translocase requires the co-operative binding of SecB and the signal sequence to SecA. *Mol. Microbiol.*, 29(5):1179–1190, 1998.

[37] K. Cunningham, R. Lill, E. Crooke, M. Rice, K. Moore, W. Wickner, and D. Oliver. SecA protein, a peripheral protein of the Escherichia coli plasma membrane, is essential for the functional binding and translocation of proOmpA. *EMBO J.*, 8(3):955–959, 1989.

[38] R. Lill, K. Cunningham, L. A. Brundage, K. Ito, D. Oliver, and W. Wickner. SecA protein hydrolyzes ATP and is an essential component of the protein translocation ATPase of Escherichia coli. *EMBO J.*, 8(3):961–966, 1989.

[39] L. P. Ghislain, N. A. Switz, and W. W. Webb. Measurement of small forces using an optical trap. *Rev. Sci. Instrum.*, 65, 1994.

[40] T. Surrey and F. Jähnig. Kinetics of folding and membrane insertion of a beta-barrel membrane protein. *J. Biol. Chem.*, 270(47):28199–28203, 1995.

[41] Y. Hiller, J. M. Gershoni, E. A. Bayer, and M. Wilchek. Biotin binding to avidin. Oligosaccharide side chain not required for ligand association. *Biochem. J.*, 248(1):167–171, 1987.

[42] W. A. Fenton and A. L. Horwich. GroEL-mediated protein folding. *Protein Sci.*, 6(4):743–760, 1997.

[43] T. Langer, C. Lu, H. Echols, J. Flanagan, M. K. Hayer, and F. U. Hartl. Successive action of DnaK, DnaJ and GroEL along the pathway of chaperone-mediated protein folding. *Nature*, 356(6371):683–689, 1992.

[44] B. Isralewitz, M. Gao, and K. Schulten. Steered molecular dynamics and mechanical functions of proteins. *Curr. Opin. Struct. Biol.*, 11(2):224–230, 2001.

[45] B. Bukau, T. Hesterkamp, and J. Luirink. Growing up in a dangerous environment: a network of multiple targeting and folding pathways for nascent polypeptides in the cytosol. *Trends Cell Biol*, 6(12):480–486, 1996.

[46] N. T. M. Knoblauch, S. Rudiger, H. J. Schonfeld, A. J. M. Driessen, J. S. Mergener, and B. Bukau. Substrate specificity of the SecB chaperone. *J. Biol. Chem.*, 274:34219–34225, 1999.

[47] G. Montoya, C. Svensson, J. Luirink, and I. Sinning. Crystal structure of the NG domain from the signal-recognition particle receptor FtsY. *Nature*, 385(6614):365–368, 1997.

[48] P. Fekkes, C. van der Does, and A. J. Driessen. The molecular chaperone SecB is released from the carboxy-terminus of SecA during initiation of precursor protein translocation. *EMBO J.*, 16(20):6105–6113, 1997.

[49] M. Eser and M. Ehrmann. SecA-dependent quality control of intracellular protein localization. *Proc. Natl. Acad. Sci. U. S. A.*, 100(23):13231–13234, 2003.

[50] W. Humphrey, A. Dalke, and K. Schulten. VMD – Visual Molecular Dynamics. *J. Mol. Graph.*, 14:33–38, 1996.

[51] L. L. Randall, T. B. Topping, D. Suciu, and S. J. Hardy. Calorimetric analyses of the interaction between SecB and its ligands. *Protein Sci.*, 7(5):1195–1200, 1998.

[52] M. Ehrmann, R. Ehrle, E. Hofmann, W. Boos, and A. Schlösser. The ABC maltose transporter. *Mol. Microbiol.*, 29(3):685–694, 1998.

[53] C. F. Higgins. ABC transporters: from microorganisms to man. *Annu. Rev. Cell. Biol.*, 8:67–113, 1992.

[54] X. Duan, J. A. Hall, H. Nikaido, and F. A. Quiocho. Crystal structures of the maltodextrin/maltose-binding protein complexed with reduced oligosaccharides: flexibility of tertiary structure and ligand binding. *J. Mol. Biol.*, 306(5):1115–1126, 2001.

[55] W. L. deLano. *The PyMOL Molecular Graphics System*. 2002. DeLano Scientific, San Carlos, CA, USA. `http://www.pymol.org`.

[56] C. Ganesh, F. N. Zaidi, J. B. Udgaonkar, and R. Varadarajan. Reversible formation of on-pathway macroscopic aggregates during the folding of maltose binding protein. *Protein Sci.*, 10(8):1635–1644, 2001.

[57] S. Sheshadri, G. M. Lingaraju, and R. Varadarajan. Denaturant mediated unfolding of both native and molten globule states of maltose binding protein are accompanied by large deltaCp's. *Protein Sci.*, 8(8):1689–1695, 1999.

[58] S. Y. Chun, S. Strobel, J. P. Bassford, and L. L. Randall. Folding of maltose-binding protein. evidence for the identity of the rate-determining step in vivo and in vitro. *J. Biol. Chem.*, 268:20855–20862, 1993.

[59] G. P. Liu, T. B. Topping, W. H. Cover, and L. L. Randall. Retardation of folding as a possible means of suppression of a mutation in the leader sequence of an exported protein. *J. Biol. Chem.*, 263(29):14790–14793, 1988.

[60] K. Beena, J. B. Udgaonkar, and R. Varadarajan. Effect of signal peptide on the stability and folding kinetics of maltose binding protein. *Biochemistry*, 43(12):3608–3619, 2004.

[61] D. L. Diamond, S. Strobel, S. Y. Chun, and L. L. Randall. Interaction of SecB with intermediates along the folding pathway of maltose-binding protein. *Protein Sci.*, 4(6):1118–1123, 1995.

[62] D. L. Diamond and L. L. Randall. Kinetic partitioning. Poising SecB to favor association with a rapidly folding ligand. *J. Biol. Chem.*, 272(46):28994–28998, 1997.

[63] T. B. Topping and L. L. Randall. Determination of the binding frame within a physiological ligand for the chaperone SecB. *Protein Sci.*, 3(5):730–736, 1994.

[64] C. A. Kumamoto. Escherichia coli SecB protein associates with exported protein precursors in vivo. *Proc. Natl. Acad. Sci. U. S. A.*, 86(14):5320–5324, 1989.

[65] H. de Cock and L. L. Randall. Correlation between requirement for SecA during export and folding properties of precursor polypeptides. *Mol. Microbiol.*, 27(2):469–476, 1998.

[66] L. L. Randall and S. J. Hardy. High selectivity with low specificity: how SecB has solved the paradox of chaperone binding. *Trends Biochem. Sci.*, 20(2):65–69, 1995.

[67] S. J. Hardy and L. L. Randall. A kinetic partitioning model of selective binding of nonnative proteins by the bacterial chaperone SecB. *Science*, 251(4992):439–443, 1991.

[68] R. B. Best, B. Li, A. Steward, V. Daggett, and J. Clarke. Can non-mechanical proteins withstand force? Stretching barnase by atomic force microscopy and molecular dynamics simulation. *Biophys. J.*, 81(4):2344–2356, 2001.

[69] H. Dietz and M. Rief. Exploring the energy landscape of GFP by single-molecule mechanical experiments. *Proc. Natl. Acad. Sci. U. S. A.*, 101(46):16192–16197, 2004.

[70] J. M. Fernandez and H. Li. Force-clamp spectroscopy monitors the folding trajectory of a single protein. *Science*, 303:1674–1678, 2004.

[71] G. Yang, C. Cecconi, W. A. Baase, I. R. Vetter, W. A. Breyer, J. A. Haack, B. W. Matthews, F. W. Dahlquist, and C. Bustamante. Solid-state synthesis and mechanical unfolding of polymers of T4 lysozyme. *Proc. Natl. Acad. Sci. U. S. A.*, 97(1):139–144, 2000.

[72] A. A. Canutescu, A. A. Shelenkov, and R. L. Dunbrack. A graph-theory algorithm for rapid protein side-chain prediction. *Protein Sci.*, 12(9):2001–2014, 2003.

[73] J. C. Phillips, R. Braun, W. Wang, J. Gumbart, E. Tajkhorshid, E. Villa, C. Chipot, R. D. Skeel, L. Kalé, and K. Schulten. Scalable molecular dynamics with NAMD. *J. Comput. Chem.*, 26(16):1781–1802, 2005.

[74] A. MacKerell, D. Bashford, M. Bellott, R. Dunbrack, J. Evanseck, M. Field, S. Fischer, J. Gao, H. Guo, S. Ha, D. Joseph-McCarthy, L. Kuchnir, K. Kuczera, F. Lau, C. Mattos, S. Michnick, T. Ngo, D. Nguyen, B. Prodhom, W. Reiher, B. Roux, M. Schlenkrich, J. Smith, R. Stote, J. Straub, M. Watanabe, J. Wiorkiewicz-Kuczera, D. Yin, and M. Karplus. All-atom empirical potential for molecular modeling and dynamics studies of proteins. *J. Phys. Chem. B*, 102(18):3586–3616, 1998.

[75] W. L. Jorgensen, J. Chandrasekhar, J. D. Madura, R. W. Impey, and M. L. Klein. Comparison of simple potential functions for simulating liquid water. *J. Chem. Phys.*, 79:926–935, 1983.

[76] J. Gumbart and K. Schulten. Molecular dynamics studies of the archaeal translocon. *Biophys. J.*, 90(7):2356–2367, 2006.

[77] P. E. Marszalek, H. Lu, H. Li, C. M. Vazquez, A. F. Oberhauser, K. Schulten, and J. M. Fernandez. Mechanical unfolding intermediates in titin modules. *Nature*, 402, 1999.

[78] A. F. Oberhauser, P. E. Marszalek, H. P. Erickson, and J. M. Fernandez. The molecular elasticity of the extracellular matrix protein tenascin. *Nature*, 393(6681):181–185, 1998.

[79] M. Rief, J. Pascual, M. Saraste, and H. E. Gaub. Single molecule force spectroscopy of spectrin repeats: Low unfolding forces in helix bundles. *J. Mol. Biol.*, 286:553–561, 1999.

[80] I. Tinoco and C. Bustamante. The effect of force on thermodynamics and kinetics of single molecule reactions. *Biophys. Chem.*, 101-102:513–533, 2002.

[81] A. J. Wilcox, J. Choy, C. Bustamante, and A. Matouschek. Effect of protein structure on mitochondrial import. *Proc. Natl. Acad. Sci. U. S. A.*, 102(43):15435–15440, 2005.

[82] T. Sato, M. Esaki, J. M. Fernandez, and T. Endo. Comparison of the protein-unfolding pathways between mitochondrial protein import and atomic-force microscopy measurements. *Proc. Natl. Acad. Sci. U. S. A.*, 102(50):17999–18004, 2005.

[83] N. Nouwen. 2005. Private communication.

[84] U. Heinemann and M. Hahn. Circular permutation of polypeptide chains: implications for protein folding and stability. *Prog. Biophys. Mol. Biol.*, 64(2-3):121–143, 1995.

[85] W. J. J. Meijer, J. A. Horcajadas, and M. Salas. Phi29 family of phages. *Microbiol. Mol. Biol. Rev.*, 65:261–287, 2001.

[86] S. Grimes, P. J. Jardine, and D. L. Anderson. Bacteriophage phi29 dna packaging. *Adv. Virus Res.*, 58:255–94, 2002.

[87] Y. Tao, N. H. Olson, W. Xu, D. L. Anderson, M. G. Rossmann, and T. S. Baker. Assembly of a tailed bacterial virus and its genome release studied in three dimensions. *Cell*, 95(3):431–437, 1998.

[88] M. C. Morais, K. H. Choi, J. S. Koti, P. R. Chipman, D. L. Anderson, and M. G. Rossmann. Conservation of the capsid structure in tailed dsDNA bacteriophages: the pseudoatomic structure of phi29. *Mol. Cell*, 18(2):149–159, 2005.

[89] V. González-Huici, M. Salas, and J. M. Hermoso. The push-pull mechanism of bacteriophage Ø29 DNA injection. *Mol. Microbiol.*, 52(2):529–540, 2004.

[90] A. Evilevitch, L. Lavelle, C. M. Knobler, E. Raspaud, and W. M. Gelbart. Osmotic pressure inhibition of DNA ejection from phage. *Proc. Natl. Acad. Sci. U. S. A.*, 100:9292–9295, 2003.

[91] H. Tabor, C. W. Tabor, and S. M. Rosenthal. The biochemistry of the polyamines: spermidine and spermine. *Annu. Rev. Biochem.*, 30:579–604, 1961.

[92] O. Lambert, L. Letellier, W. M. Gelbart, and J. L. Rigaud. DNA delivery by phage as a strategy for encapsulating toroidal condensates of arbitrary size into liposomes. *Proc. Natl. Acad. Sci. U. S. A.*, 97(13):7248–7253, 2000.

[93] Z. Lin, C. Wang, X. Feng, M. Liu, J. Li, and C. Bai. The observation of the local ordering characteristics of spermidine-condensed DNA: atomic force microscopy and polarizing microscopy studies. *Nucleic Acids Res.*, 26(13):3228–3234, 1998.

[94] Y. Murayama, Y. Sakamaki, and M. Sano. Elastic response of single DNA molecules exhibits a reentrant collapsing transition. *Phys. Rev. Lett.*, 90(1), 2003.

[95] W.-D. Moll and P. Guo. Translocation of nicked but not gapped DNA by the packaging motor of bacteriophage phi29. *J. Mol. Biol.*, 351(1):100–107, 2005.

[96] J. Aymami, M. Coll, G. A. van der Marel, J. H. van Boom, A. H. Wang, and A. Rich. Molecular structure of nicked DNA: a substrate for DNA repair enzymes. *Proc. Natl. Acad. Sci. U. S. A.*, 87(7):2526–2530, 1990.

[97] K. R. Paithankar and K. S. N. Prasad. Precipitation of DNA by polyethylene glycol and ethanol. *Nucl. Acids. Res.*, 19, 1991.

[98] D. C. Schwartz and C. R. Cantor. Separation of yeast chromosome-sized DNAs by pulsed field gradient gel electrophoresis. *Cell*, 37(1):67–75, 1984.

[99] S. Grimes and D. Anderson. The bacteriophage [phi]29 packaging proteins supercoil the dna ends. *J. Mol. Biol.*, 266:901–914, 1997.

[100] C. G. Baumann, S. B. Smith, V. A. Bloomfield, and C. Bustamante. Ionic effects on the elasticity of single DNA molecules. *Proc. Natl. Acad. Sci. U. S. A.*, 94:6185–6190, 1997.

[101] E. Raspaud, M. O. de la Cruz, J. L. Sikorav, and F. Livolant. Precipitation of DNA by polyamines: a polyelectrolyte behavior. *Biophys. J.*, 74(1):381–393, 1998.

[102] H. Wada, Y. Murayama, and M. Sano. Model of elastic responses of single DNA molecules in collapsing transition. *Phys Rev E Stat Nonlin Soft Matter Phys*, 66(6 Pt 1):061912, 2002.

[103] S. B. Smith, L. Finzi, and C. Bustamante. Direct mechanical measurements of the elasticity of single dna molecules by using magnetic beads. *Science*, 258, 1992.

[104] T. Odijk. Stiff chains and filaments under tension. *Macromolecules*, 28:7016–18, 1995.

[105] S. B. Smith, Y. Cui, and C. Bustamante. Overstretching B-DNA: the elastic response of individual double-stranded and single-stranded DNA molecules. *Science*, 271, 1996.

[106] P. Cluzel, A. Lebrun, C. Heller, R. Lavery, J. L. Viovy, D. Chatenay, and F. Caron. DNA: an extensible molecule. *Science*, 271(5250):792–794, 1996.

Summary

This thesis describes experiments that have been performed to study a number of biological processes on a single-molecule level: the translocation of a protein through phospholipid membranes, the unfolding of a protein and the effect of a molecular chaperone on this unfolding, and the packaging of double-stranded DNA by the bacterial virus bacteriophage ϕ29. These experiments have been performed using optical tweezers.

Optical tweezers

Optical tweezers—also called 'optical traps', or 'laser tweezers'—are based on the central observation that a heavily focussed laser beam can be used to stably grab and hold micron-sized particles with a refractive index higher than the surrounding medium, e. g., a polystyrene microsphere in water. If a microsphere slightly moves away from the trap center, e. g., due to thermal—Brownian—motion, the restoring force in the direction of the trap center scales linearly with the distance between the microsphere and the center of the focus. This observation enables the use of optical tweezers as a force probe that can measure forces up to 100 pN with an accuracy of down to less than 0.1 pN. By chemically coupling an optically trapped microsphere to a force-generating biochemical process, the force exerted by this process on the microsphere can be measured by monitoring the position of the microsphere inside the potential well that is formed by the optical tweezers.

Since the first application of optical tweezers in biology—In 1987, Arthur Ashkin and coworkers showed that *E. coli* bacteria can survive and even divide when being trapped by an infra-red laser focus—optical tweezers have been applied to numerous subjects in biology and biophysics. They have been used to study the action of single molecular motors, such as myosin, kinesin and the packaging motor of bacteriophage ϕ29. Also, the elastic and thermodynamic properties of single biopolymers such as polypeptides, nucleic acids and cytoskeletal filaments such as actin and microtubules have been determined using optical tweezers. In all these subjects, interesting behavior is observed in the pN-force range, rendering optical tweezers an ideal experimental tool. Apart from their use in biological subjects, optical tweezers also find their use in experimental soft-matter physics.

In Chapter 1, we described the optical tweezers setup that we built and used for various experiments that are described in the other chapters of this thesis. We have described how we used the setup to measure forces. Furthermore, we described the flow system that we implemented to enable quick and reliable control of the buffer composition during experiments.

Towards optical tweezers measurements on protein translocation

One of the subjects we aimed to study using our optical-tweezers setup was the translocation of proteins through phospholipid membranes by the *E. coli* Sec translocase. In this process, proteins that are destined for the periplasm, for secretion or for integration in a membrane, are targeted to the *E. coli* inner membrane after their synthesis. There, the protein is transported through a pore in a protein complex termed translocase, that mainly consists of the SecYEG heterotrimer. Only proteins having an N-terminal signal sequence are being translocated. The translocation of the protein is driven by ATP hydrolysis by SecYEG-associated ATPase SecA, and by the so-called proton motive force—the proton gradient over the membrane. Due to the dimensions of the pore, the protein must go through in an unfolded state. To prevent a protein from folding or aggregation prior to its translocation, the molecular chaperone SecB binds to the protein after synthesis by the ribosome, thus enhancing the translocation efficiency.

From bulk studies, a large body of experimental data is available for this process. We aimed to perform single-molecule experiments on protein translocation. Using our optical tweezers setup, we aimed to follow a single protein as it is being translocated through the membrane, to address remaining fundamental questions regarding the mechano-chemistry of ATPase SecA and the role of folding dynamics of the translocated protein during its translocation. Furthermore, we hoped to measure step sizes and forces involved in translocation.

For our experimental approach, we modified the canonical bulk translocation activity assay, that uses SecYEG-containing *E. coli* membrane vesicles. As a substrate protein for translocation, we constructed a derivative of model protein proOmpA, carrying eight in-tandem repeats of its periplasmic domain, thus increasing the available measurement time per protein and possibly introducing repetitive features in eventual translocation measurements. We used this protein in a different (bulk) study to show that translocation occurs at a constant rate (in amino acids per second). In our optical-tweezers approach, we aimed to couple the C terminus of this protein to an optically trapped polystyrene microsphere via an 800-nm dsDNA linker and biotin–streptavidin interactions. The SecYEG-containing vesicles were electrostatically bound to another microsphere that was held fixed using a micropipette.

In Chapter 2, we have shown that *E. coli* vesicles can indeed be bound to polystyrene microspheres. Moreover, bulk studies showed that the vesicles still showed translocation activity. Furthermore, we have shown that translocation of a protein can effectively be halted by binding a streptavidin to a biotin on its C terminus. Due to non-specific attachments of both substrate protein and streptavidin tetramers to the membrane surface, the DNA linker could not be specifically coupled to translocase-associated streptavidin tetramers. Future modifications to our optical-tweezers approach, possibly involving a different or modified substrate-protein construct, need to be performed for successful single-molecule experiments.

Unfolding the maltose-binding protein (MBP) with optical tweezers

In Chapter 3, we have described optical tweezers experiments that have been performed on the folding and unfolding of the maltose-binding protein, or MBP. Moreover, we have studied the effect of molecular chaperone SecB on this folding and unfolding behavior.

MBP is a periplasmic protein that is part of the *E. coli* maltodextrin transport system. It has often been used as a model protein in bulk studies to study protein folding and SecB–protein interaction. We have used optical tweezers to unfold single MBP proteins. To do this, we introduced a novel experimental geometry, in which we bound the C terminus of the protein to a micropipette-held microsphere via antibody–epitope interactions. The N terminus was bound to an optically trapped microsphere via a DNA linker and biotin–streptavidin interactions. By moving the micropipette with respect to the optical trap, we could increase the force exerted on the protein termini, leading to the eventual unfolding of the protein. By again lowering the force on the unfolded polypeptide, we could show the subsequent refolding. This could be repeated several times for a single protein. Unfolding occurred at a force of around 25 pN. Before the full unfolding of the protein, often an unfolding intermediate was observed leading to a polypeptide contour length of ~28 nm.

In measurements where we used a protein consisting of four in-tandem repeats of MBP rather than the single-MBP construct, we observed the almost simultaneous unfolding of each of the subunits to the intermediate, prior to the consecutive complete unfolding of the rest of each of the subunits. This complete unfolding occurred at forces similar to that of the single-MBP construct. When again decreasing the force exerted on the protein termini, this protein construct would irreversibly aggregate, rather than refold to its native state.

From previous bulk studies, no unfolding intermediates were known for MBP. Steered molecular dynamics (SMD) simulations showed a likely explanation for the observed intermediate, being a series of surface-exposed C-terminal α-helices that would easily detach from the MBP structure in our simulations.

When a physiological concentration of molecular chaperone SecB was added during a protein unfolding experiment, the unfolding would occur as in the absence of SecB. This confirms previous experimental observations that showed that SecB can only bind to non-native proteins. After the unfolding of a protein, the presence of SecB would completely quench the refolding or—in the case of the 4×MBP construct—aggregation of the protein. Extending the SecB-bound polypeptide resembled that of a polypeptide with no internal secondary or tertiary structure.

Optical tweezers measurements on dsDNA-packaging by bacteriophage ϕ29

Chapter 4 describes various optical tweezers experiments on the packaging of dsDNA by bacteriophage ϕ29. Bacteriophages are viruses that specifically infect bacteria. Bacteria infect their host cell by injecting their genetic material (double- or single-stranded DNA or RNA). The gene expression machinery of the host cell will start producing new viral proteins and eventually also the viral genome is replicated. New viruses can be formed after the packaging of the genetic material in new virus shells, or capsids. For bacteriophage ϕ29, the 6.6 μm-long dsDNA genome is compressed into a cavity of 42 nm in width and 54 nm in length during this process. Large entropic, electrostatic and bending energies must be overcome to package the highly negatively-charged DNA to near-crystalline density. Smith et al. have used optical tweezers to study the packaging of single bacteriophages. They have shown that until ~50% of the bacteriophage genome has been packaged, the packaging rate (in DNA base pairs per second) is constant. The packaging rate then slowly decreases until the full genome has been packaged. It was shown that bacteriophage ϕ29 can package DNA that is 10% longer than its genome.

We have performed experiments aiming to study the effect of polyvalent cations on the packaging rate in this dense regime. Of polyvalent cations such as spermine, it known that they can condense dsDNA into toroidal condensates. Condensation of dsDNA inside the bacteriophage capsid might affect the packaging rate in the dense regime. Furthermore, we have aimed to study the effect of single-stranded breaks, or nicks, in the ϕ29 DNA on the packaging.

For the optical tweezers experiments, we engineered a DNA construct derived from the ϕ29 DNA that was 60% longer and contained a biotin on one end to enable coupling to an optically trapped bead. Because of the length of the DNA construct, and the viral protein gp3 that was bound to its 5′-ends, several non-standard biochemical techniques were explored in this procedure.

In our experiments, we have shown the condensing effect of spermine on a tethered DNA strand. Furthermore, using a short ϕ29 DNA construct, we have shown that neither the presence of a condensing concentration of spermine, nor the presence of nicks in the DNA, significantly affect the packaging rate when less than 50% of the ϕ29 genome has been packaged. Future experiments using the engineered longer ϕ29 DNA construct will have to show that this is also the case when packaging has proceeded to the dense (>50%) regime.

Samenvatting

In dit proefschrift beschrijf ik experimenten die zijn uitgevoerd om een aantal biologische processen te bestuderen op het niveau van afzonderlijke DNA- of eiwitmoleculen. De processen die ik heb bestudeerd zijn: transport van eiwitmoleculen door celmembranen, het ontvouwen van een eiwitmolecuul en het effect van een zgn. 'moleculaire chaperonne' hierop, en tenslotte het importeren van DNA door het bacteriële virus bacteriofaag ϕ29. Alvorens in meer detail in te gaan op elk van deze processen en de resultaten die ik behaald heb, wil ik iets meer vertellen over het apparaat waarmee de experimenten zijn verricht: het optisch pincet.

Het optisch pincet

Een optisch pincet maak je door een zeer intense lichtstraal – typisch een laserstraal – met behulp van een zeer goede lens – een microscoopobjectief – te focusseren tot een focus ter grootte van een duizendste millimeter (een micron). Als je dit in water doet, en het focus richt op daarin ronddrijvende glazen bolletjes ongeveer even groot als het focus, zullen deze bolletjes prompt stoppen met hun beweging, en blijven hangen in het midden van het focus. Bovendien zullen de bolletjes bij het verplaatsen van het focus braaf volgen. Dit klinkt wonderbaarlijk – Hoe kan je met licht dingen verplaatsen? – maar valt enigszins te begrijpen als je een invallende lichtbundel beschouwt als een bombardement van kleine deeltjes. Deze deeltjes – fotonen genaamd – veranderen na contact met het bolletje van richting, enerzijds door weerkaatsing aan het oppervlak, maar vooral doordat de lenswerking van het bolletje doorgaande fotonen van richting doet veranderen. Richtingsverandering van één zo'n foton zal resulteren in een minuscule kracht op het bolletje, zoals een stuiterende tennisbal dat op de aardbol doet. Doordat midden in een sterk gefocusseerde laserstraal zeer veel fotonen van bijna alle kanten komen, zal de netto kracht altijd naar het midden van het focus gericht zijn en zal het bolletje daar blijven hangen als de intensiteit van de laser hoog genoeg is.

Tegenwoordig worden optische pincetten (in het Engels: *optical tweezers*) veelal gebruikt als krachtsensor bij vooral biologische processen. Met behulp van een optisch pincet kunnen krachten worden gemeten ter grootte van een piconewton, dat wil zeggen ongeveer een miljoenste van een tienmiljoenste van de kracht die een kilo suiker uitoefent op je hand. Toevallig zijn dit de krachten die relevant zijn op het niveau kleiner dan dat van een enkele cel. Later noem ik enkele biologische processen die ik heb bestudeerd en waar krachten van enkele of tientallen piconewtons een rol spelen. Als in zo'n biologisch proces bijvoorbeeld een eiwitmolecuul aan zo'n bolletje in een optisch pincet trekt, zal het bolletje enigszins uit het midden van het focus worden getrokken. Tegelijkertijd ondervindt het door het invallende licht nog steeds een kracht gericht naar het midden van het focus, ongeveer gelijk aan de kracht waarmee het door het eiwitmolecuul naar buiten wordt getrokken. Deze kracht blijkt evenredig te zijn aan de afstand tussen het midden van het bolletje en het midden van het focus. Door nu op een of andere manier de afstand tussen bolletje en focus te meten, kan men dus de kracht meten waarmee het eiwitmolecuul aan het bolletje trekt.

Het optisch pincet maakt dus nauwkeurige metingen van krachten en bewegingen van afzonderlijke moleculen mogelijk. Vóor de uitvinding van het optische pincet (en van andere technieken gebruikt in de zgn. enkelmolecuuls biofysica: het magnetische pincet, atomaire krachtmicroscopie [afm] en diverse geavanceerde fluorescentiemicroscopie-technieken) kon alleen het gedrag van zeer vele moleculen tegelijk worden bepaald en het gedrag van afzonderlijke moleculen kon alleen worden bepaald door daarvan een gemiddelde te nemen – iets wat vaak net zo verantwoord is als het gedrag van één persoon herleiden uit het gemiddelde van een maatschappij.

In Hoofdstuk 1 van dit proefschrift beschrijf ik een optisch-pincetopstelling die ik heb gebouwd voor mijn onderzoek en die is gebruikt voor de meeste van de experimenten die in de andere hoofdstukken van dit proefschrift worden beschreven.

Eiwitmoleculen

Voordat ik verder over mijn onderzoek ga vertellen wil ik eerst iets meer vertellen over eiwitmoleculen. De gemiddelde menselijke cel bestaat voor 18% uit eiwitmoleculen en voor de rest uit water (70%) en andersoortige moleculen (o. a. dna, zouten en fosfolipiden, de bouwstenen van celmembranen). Binnen de cel hebben eiwitten talloze functies. Ze geven de cel stevigheid, ze maken het mogelijk dat een cel zich kan delen, ze zorgen voor transport van moleculen binnen de cel, ze beschermen de cel tegen schadelijke bacteriën en virussen, etc. De manier waarop ze opgebouwd zijn is wat ze gemeen hebben. Elk eiwit wordt gevormd door een keten van enkele honderden zogenaamde aminozuren, waarvan er in totaal 20 verschillende zijn. Eiwitten verschillen in de manier waarop deze aminozuren aan elkaar zijn gekoppeld. In een waterige omgeving 'vouwt' zo'n aminozuurketen tot een eiwit, doordat sommige aminozuren elkaar aantrekken, en andere aminozuren worden afgestoten door het omringende water, waardoor ze ergens in het midden van de kluwen zullen terecht komen. Niet elke willekeurig gekoppelde serie van aminozuren kan stabiel vouwen tot een eiwit. Miljoenen jaren evolutie hebben ervoor gezorgd dat veruit de meeste van de in de natuur voorkomende aminozuurketens wel stabiel kunnen vouwen tot een eiwit, dat bovendien ook nog een bepaalde functie (goed) kan verrichten binnen een cel.

Transport van eiwitmoleculen door een celmembraan

Eén van de biologische processen die ik heb bestudeerd (beschreven in Hoofdstuk 2) is het transport van eiwitmoleculen door een celmembraan. Alle cellen in de natuur, van eencellige organismen als de *E. coli* bacterie tot cellen van meercellige organismen als wijzelf, worden omgeven door celmembranen. Bovendien zijn cellen van hogere organismen onderverdeeld in verschillende compartimenten, die elk ook weer zijn omgeven door vergelijkbare membranen. Deze membranen zijn flexibel, maar laten geen spontane verplaatsing van eiwitmoleculen van de ene kant naar de andere kant toe. Indien dit toch nodig is, moet dit gebeuren via speciale poriën in het membraan. Eén zo'n porie wordt gevormd door de zogenaamde Sec translocase. De Sec translocase is een complex van verschillende eiwitmoleculen dat in alle bekende organismen te vinden is. Het is gedurende de evolutie van eencellige tot *Homo sapiens sapiens* in grote lijnen gelijk gebleven.

Wij hebben voor onze experimenten gebruik gemaakt van de Sec translocase van de *E. coli* bacterie, omdat hierover een grote hoeveelheid wetenschappelijke literatuur is geschreven en omdat het om verschillende redenen een relatief eenvoudig systeem is om te bestuderen. In *E. coli* wordt de porie gevormd door een eiwitcomplex genaamd SecYEG. Om geen water en zouten en dergelijke door te kunnen laten is de porie gevormd door dit complex minuscuul klein. Dit heeft als consequentie dat een eiwit er in gevouwen toestand niet meer doorheen kan. Het eiwit moet dus ontvouwen zijn tot een ontvouwen aminozuurketen voor het getransporteerd kan worden – aminozuur voor aminozuur. Om de ontvouwen aminozuurketen door het membraan heen te transporteren, ofwel te transloceren, is energie nodig. Deze energie wordt binnen de cel geleverd door het molecuul ATP, en wordt omgezet in beweging van de aminozuurketen door het zogenaamde motoreiwit SecA.

Zoals gezegd is er in wetenschappelijke literatuur al veel bekend over dit systeem. Al deze kennis is verkregen met behulp van zogenaamde *bulk*-experimenten, waarbij het gedrag van zeer vele translocases tegelijk is bekeken. Enkele essentiële vragen over het precieze mechanisme van het eiwittransport zijn echter alleen te beantwoorden met behulp van experimenten aan afzonderlijke translocases. Om deze vragen te beantwoorden hebben wij geprobeerd zulke metingen te doen met behulp van onze optisch-pincetopstelling. Door tijdens het transport van een aminozuurketen het nog vrije eindje te koppelen aan een met een optisch pincet vastgehouden bolletje, wilden wij het proces volgen in de tijd.

Om deze experimenten mogelijk te maken hebben wij verschillende maatregelen genomen. Om tijdens metingen geen last te hebben van de slapte van het membraan hebben wij het *E. coli* membraan verwerkt tot blaasjes van ongeveer een tiende micron. Deze blaasjes werden aan polystyreen balletjes geplakt van enkele micron groot, die op hun beurt weer op hun plaats werden gehouden door ze vast te zuigen aan een micropipet – een hol buisje met een binnendiameter van ongeveer een micron. In *bulk*-experimenten hebben wij laten zien dat de translocases in de vastgeplakte blaasjes nog steeds actief zijn. Voor de experimenten hebben wij het eiwit proOmpA gebruikt, een standaardeiwit voor eiwittranslocatie-experimenten. Om de duur van een experiment te verlengen hebben wij een deel van de aminozuurketen van dit eiwit enkele malen verdubbeld, zodanig dat de aminozuurketen vijf keer zo lang werd. In *bulk*-experimenten met dit eiwit hebben wij laten zien dat in eiwittranslocatie de translocatiesnelheid in aminozuren per seconde constant is. In onze opzet werd een met een optisch pincet vastgehouden balletje aan het te transloceren eiwitmolecuul vastgeplakt via een DNA-molecuul van ongeveer een micron lang. Door de hierdoor vergrote afstand tussen optisch-pincetballetje en balletje op de micropipet wordt voorkomen dat de laserstraal van het optisch pincet wordt beïnvloed door het balletje op de micropipet. Deze koppeling bleek echter moeilijk te verwezenlijken, enerzijds doordat proOmpA aan het membraan bleef plakken zonder te transloceren, en anderzijds omdat het molecuul dat werd gebruikt om DNA en proOmpA aan elkaar te plakken – streptavidine – ook aan het membraan bleef plakken.

Het ontvouwen van een eiwitmolecuul

Een ander biologisch proces dat wij hebben bestudeerd met behulp van mijn optisch-pincetopstelling is het vouwen en ontvouwen van een eiwit, en het effect van een zogenaamde moleculaire chaperonne hierop. Deze experimenten zijn beschreven in Hoofdstuk 3.

Eerder heb ik beschreven hoe een aminozuurketen kan vouwen tot een functioneel eiwitmolecuul. Hoe dit precies gebeurt is echter allerminst bekend en bovendien voor elk eiwit verschillend. Met behulp van mijn optisch-pincetopstelling hebben we het ontvouwen en vouwen van één afzonderlijk eiwit, het maltosebindende eiwit ofwel MBP, bestudeerd. In gevouwen toestand bevinden beide eindjes van de aminozuurketen zich aan de buitenkant van het eiwit. Door beide eindjes vast te houden met behulp van het optisch pincet en de micropipet kan het eiwit uit elkaar getrokken worden.

Zoals ook al voor andere eiwitten is gezien gebeurt dit ontvouwen pas bij hogere kracht (voor MBP bij 25 piconewton) en het ontvouwen is dan ook volledig. Vóor het volledig ontvouwen van het eiwit zagen wij een soort van tussentoestand, waarbij blijkbaar een deel van de aminozuurketen al werd ontrafeld. Als de kracht op de ontvouwen aminozuurketen weer werd verlaagd, vouwde het weer tot een werkzaam MBP-eiwit binnen tien seconden. Naast MBP hebben wij ook een eiwitconstruct ontvouwen bestaande uit vier afzonderlijke MBP-eiwitten gekoppeld in een kop–staartgeometrie. Deze experimenten lieten dezelfde ontvouwingskracht zien als in het geval van het enkele MBP-eiwit. Verder was het duidelijk te zien dat vóor het volledig ontvouwen van elk van de eiwitten, de vier eiwitten ongeveer tegelijkertijd ontvouwden tot de ontvouwings-tussentoestand die we ook al zagen bij het enkele MBP-eiwit.

Uit eerdere *bulk*-experimenten aan het ontvouwen van MBP waren dergelijke tussentoestanden nog niet bekend. Om deze reden hebben wij computersimulaties verricht aan het ontvouwen van MBP. In dergelijke simulaties – moleculaire dynamicasimulaties – worden atomen gemodelleerd als balletjes en de verschillende krachten tussen atomen als springveren. Om dit soort simulaties realistisch te maken moet de simulatie worden opgedeeld in tijdstapjes van een halve femtoseconde, ofwel een miljoenste van een miljoenste milliseconde. Voor elk tijdstapje moet de positie van tienduizenden atomen berekend worden, waardoor een simulatie – ondanks de rekenkracht van hedendaagse parallelle computers – zeer lang kan duren. Om een simulatie van een eiwit-ontvouwingsexperiment in een werkbare tijd te kunnen voltooien wordt de treksnelheid in de simulatie dan ook flink opgevoerd vergeleken met de treksnelheid in het optisch-pincetexperiment. Dankzij de verrichte computersimulaties hebben wij een verklaring voor de geziene tussentoestand kunnen vinden die perfect overeenkomt met de data uit de experimenten.

Tijdens onze MBP-vouwings- en -ontvouwingsexperimenten hebben wij het moleculaire chaperonne-eiwit SecB toegevoegd. Dit eiwit is nauw betrokken bij eiwittranslocatie door de eerder genoemde Sec translocase. SecB houdt nieuwe, net gesynthetiseerde aminozuurketens in een ontvouwen staat, zodanig dat het door het SecYEG porie-complex getransporteerd kan worden. Het doet dit door zodanig aan de nieuwe aminozuurketen te binden dat aminozuren die in het gevouwen eiwit dicht bij elkaar zitten elkaar niet kunnen vinden. In onze experimenten zagen wij geen effect van SecB vóórdat MBP volledig was ontvouwen. De ontvouwingskracht was gelijk, en ook zagen wij geen verschil in ontvouwings-tussentoestanden. Echter, als we de ontvouwen aminozuurketen weer wat losser lieten, vouwde het onder invloed van SecB niet meer tot een functioneel eiwit, zoals dat in de afwezigheid van SecB wél gebeurde. Deze observaties bevestigen dat SecB geen invloed heeft op reeds gevouwen eiwitten. Verder blijkt dat voor het uitrekken van een SecB-gebonden aminozuurketen – zoals dat tijdens eiwittranslocatie eigenlijk ook gebeurt – aanzienlijk minder kracht benodigd is dan voor het ontvouwen van een functioneel eiwit.

DNA-import door bacteriofaag ϕ29

Als laatste beschrijf ik in Hoofdstuk 4 van dit proefschrift optisch-pincetexperimenten aan DNA-import door het virus bacteriofaag ϕ29. Bacteriofagen zijn virussen die specifiek bacteriën infecteren. Bacteriofagen bestaan voor het grootste deel uit hun genetisch materiaal – DNA of RNA – omgeven door een beschermend hulsje van eiwitten. Ze infecteren een bacterie door hun genetisch materiaal in de gastheercel te injecteren. De bacterie zal nu het DNA of RNA van het virus behandelen als zijn eigen genetisch materiaal en zal de eiwitten die worden beschreven op het DNA of RNA gaan produceren. Uit deze eiwitten worden nu spontaan nieuwe virushulsjes gevormd. Als laatste wordt het virale genetische materiaal vermenigvuldigd, zoals een cel ook met zijn eigen DNA doet als het deelt. Voordat de lege virushulsjes kunnen uitgroeien tot rijpe nieuwe virussen die weer nieuwe gastheercellen kunnen infecteren, moeten ze eerst gevuld worden met hun genetisch materiaal. In het geval van bacteriofaag φ29 wordt in dit proces een DNA-molecuul van 6,6 micron lang in een holte van 42 bij 54 duizendste micron 'gepropt'. Optisch-pincetxperimenten van o. a. Sander Tans hebben laten zien dat hierbij een druk wordt opgebouwd binnen het hulsje van 60 maal de luchtdruk. Voordat het hulsje voor 50% gevuld is met DNA is de importsnelheid constant. Daarna begint de snelheid langzaam af te nemen onder invloed van de opgebouwde druk binnen het hulsje. In totaal past er binnen het hulsje DNA met een lengte van 10% langer dan het normale φ29 DNA.

Wij hebben optisch-pincetexperimenten gedaan om met name het stadium van DNA-import beter te begrijpen als het hulsje voor meer dan 50% vol is. Een van de redenen voor de hoge druk die hier ontstaat is de sterke negatieve elektrische lading van het DNA. Als DNA zo dicht gepakt wordt gaat het zichzelf hierdoor afstoten. Door het toevoegen van een sterk positief elektrisch geladen molecuul – spermine – hoopten wij voor dit effect te compenseren. Van spermine is bekend dat het DNA ringvormig kan doen samenklonteren. Verwacht was dat dit binnen de virushulsjes ook zou gebeuren. Door de dubbele-helixstructuur is DNA een redelijk stijf molecuul, waardoor het moeilijk is het strak op te rollen binnen een klein hulsje. Door een van de twee helices op verschillende plekken door te knippen met behulp van speciale enzymen verwachtten wij dat dit makkelijker zou worden.

Voor onze experimenten hebben wij het φ29-DNA zodanig gewijzigd dat het aanzienlijk (60%) langer werd en dat één van de twee eindjes geschikt werd om er een met een optisch pincet vastgehouden balletje aan te koppelen. Omdat het φ29-DNA te lang was voor sommige standaardtechnieken die daarbij normaal gebruikt worden, en omdat er een eiwitmolecuul aan het φ29-DNA gekoppeld zit, moesten hierbij verschillende nieuwe technieken uitgeprobeerd worden.

Daarna hebben wij met behulp van onze opstelling het samenklonterende effect van spermine getest. Vervolgens hebben wij, met behulp van een DNA-construct dat niet lang genoeg is om het hulsje voor meer dan 60% te vullen, het effect van spermine en knipjes in een van de twee DNA-helices op de DNA-importsnelheid gemeten. Hier was geen effect van te zien. Latere experimenten met behulp van het verlengde DNA-construct moeten laten zien of er een effect is als het hulsje voor meer dan 60% vol is.

Curriculum Vitae

Ruud van Leeuwen was born in Gouda, The Netherlands on December 9th, 1976. From 1989 to 1995 he attended 'Voorbereidend Wetenschappelijk Onderwijs' (VWO) at the St.-Antoniuscollege in Gouda. Next, he started his studies in Applied Physics at Delft University of Technology. During his studies, he worked as a Summer Research Assistant at the NATO Undersea Research Center (NURC) in La Spezia, Italy, doing research on a benchmark method for simulation models of undersea sound propagation. His undergraduate research was done in the Laboratory of Acoustic Imaging and Sound control under supervision of Dr G. Blacquière and Dr C. P. A. Wapenaar. In his Master's thesis, entitled *Imaging of acoustic data acquired on a circular array using wave field extrapolation*, he describes a new method of imaging tissue using ultrasound and a circular array of sound transducers. After graduating in 2001, he started his PhD research in the Biophysics group of Dr Sander J. Tans at the FOM Institute for Atomic and Molecular Physics (AMOLF) in Amsterdam. The results of this research are described in this thesis.

List of publications

D. Tomkiewicz, N. Nouwen, R. van Leeuwen, S. Tans, and A. J. M. Driessen. SecA supports a constant rate of preprotein translocation. *J. Biol. Chem.*, 281(23):15709–15713, 2006.

R. van Leeuwen, M. Tyreman, P. Bechtluft, H. Tepper, D. Rozeveld, D. Tomkiewicz, N. Nouwen, A. J. M. Driessen, and S. Tans. Single-molecule observation of molecular chaperone action. *In preparation*, 2006